# Mechatronics Optimization Development for Wind Tunnel Tests

Master's thesis in Mechatronics Engineering applied to Aerodynamics

Pierfrancesco Oselin

DEPARTMENT OF MECHANICS AND MARITIME SCIENCES

CHALMERS UNIVERSITY OF TECHNOLOGY
Gothenburg, Sweden 2023
www.chalmers.se

Master's thesis 2023

# Mechatronics Optimization and Development for wind tunnel tests

Pierfrancesco Oselin

Department of Mechanics and Maritime Sciences
*Division of Vehicle Engineering and Autonomous Systems*
Chalmers University of Technology
Gothenburg, Sweden 2023

Mechatronics Optimization and Development for wind tunnel tests
Pierfrancesco Oselin

Supervisor: Guglielmo Minelli, Volvo Cars
Examiner: Simone Sebben, Department

Master's Thesis 2023
Department of Mechanics and Maritime Sciences
Division of Vehicle Engineering and Autonomous Systems
Chalmers University of Technology
SE-412 96 Gothenburg
Telephone +46 31 772 1000

Cover: Rear diffusers optimized for different side wind conditions, mounted on the Volvo EX90

Typeset in LaTeX
Printed by Chalmers Reproservice
Gothenburg, Sweden 2023

Mechatronics Optimization and Development for wind tunnel tests
Pierfrancesco Oselin
Department of Mechanics and Maritime Sciences
Division of Vehicle Engineering and Autonomous Systems
Chalmers University of Technology

# Abstract

In the realm of the automotive industry, the development of vehicles entails the fulfillment of numerous requirements such as appealing design, comfort, safety, and efficiency. Notably, in recent years, the significance of efficiency has grown due to mounting environmental concerns regarding internal combustion engine (ICE) vehicles and limitations on the range of battery electric vehicles (BEVs).

Of the various engineering aspects, aerodynamics assumes a pivotal role in determining the performance of cars, exerting a substantial influence on vehicle efficiency. To investigate and enhance aerodynamics, automotive companies adopt a combined approach involving both digital and real-world testing. The former is accomplished through the utilization of Computed Fluid Dynamic (CFD) analyses, while the latter entails wind tunnel testing of clay car models.

This thesis covers the current approach to the study of aerodynamics, focusing on the issues that characterize the existing workflow, including downtime and inaccuracies. In response to these challenges, a novel workflow founded on automated mechatronics optimization is introduced and a prototype is tested, thereby showcasing a fresh and more efficient modality of working with clay car models within wind tunnel facilities.

The proposed workflow aims to enhance the aerodynamic optimization of vehicles by implementing a scalable, plug-and-play system that expedites the process and yields advanced, efficient designs. This endeavor has brought to remarkable results, such as the development of an innovative diffuser configuration that enhances efficiency during side-wind conditions, as well as a 73.4% reduction in time within the current wind tunnel workflow through the application of automated mechatronics.

Keywords: BEV, mechatronics, optimization, wind tunnel tests, clay car.

# Acknowledgements

Lorem ipsum dolor sit amet, consectetur adipisicing elit, sed do eiusmod tempor incididunt ut labore et dolore magna aliqua. Ut enim ad minim veniam, quis nostrud exercitation ullamco laboris nisi ut aliquip ex ea commodo consequat. Duis aute irure dolor in reprehenderit in voluptate velit esse cillum dolore eu fugiat nulla pariatur. Excepteur sint occaecat cupidatat non proident, sunt in culpa qui officia deserunt mollit anim id est laborum.

PIERFRANCESCO OSELIN, Gothenburg, June 2023

# List of Acronyms

Below is the list of acronyms that have been used throughout this thesis listed in alphabetical order:

| | |
|---|---|
| AC | Alternate Current |
| ADAS | Advanced Driver Assistance System |
| BEV | Battery Electric Vehicle |
| CFD | Computed Fluid Dynamic |
| CPS | Cyber-Physical System |
| DC | Direct Current |
| DNN | Deep Neural Network |
| GUI | Graphical User Interface |
| ICE | Internal Combustion Engine |
| IP | Internet Protocol |
| LIMO | Loop-In-the-Model Optimization |
| MQTT | Message Queuing Telemetry Transport |
| PLC | Programmable Logic Controller |
| QoS | Quality of Service |
| TCP | Transmission Control Protocol |

# Contents

# List of Figures

# List of Tables

# 1

# Introduction

The automotive industry faces numerous challenges when it comes to the development and production of cars. From the initial digital concept to the tangible realization of a vehicle, car manufacturers are tasked with finding the optimal balance between various requirements while always striving for exceptional performance and efficiency.

Among these requirements, it is possible to find factors such as appealing design, comfort, driving experience, safety, and reliability. However, in recent years, a new imperative has emerged – the need for efficiency, driven by the growing awareness of global warming and the rising costs of traditional fuel sources.

As customers expectation demands vehicles that cover more kilometers while minimizing fuel consumption, automotive manufacturers must incorporate efficiency considerations into their research and development phases. The focus on efficiency is not only driven by economic factors but also by the pressing need to reduce emissions and pollution associated with the transportation sector. Furthermore, the advent of battery electric vehicles (BEVs) has introduced a paradigm shift, distinguishing them from traditional internal combustion engine (ICE) vehicles that rely on fuel combustion for propulsion.

Aerodynamics plays a critical role in making modern cars meet the efficiency requirements. By comprehensively understanding the principles and effects of aerodynamics, vehicles can be designed with enhanced fuel efficiency, reduced emissions, and aligned with global environmental goals.

Moreover, by examining the contrast between BEVs and ICE vehicles, we can identify how aerodynamic considerations play a crucial role in the development of both vehicle types.

Modern car manufacturing companies currently cover the aerodynamic study in a hybrid manner: after few iteration in the styling of a vehicle, aerodynamics engineers test the model and its efficiency in a digital environment to simulate its performances and estimate how promising a new car concept could be. This virtual study, defined by the use of Computed Fluid Dynamics (CFD) allows to investigate interesting factors and phenomena, but trade-off in accuracy must be assumed.

Because of that, an additional set of physical tests is required in these companies. Pre-production clay car model of the selected concept are tested in wind tunnel facilities to more accurately determine the aerodynamic characteristics of this car.

Nevertheless, this second approach comes with downsides: a less flexible setup in terms of model changes and configurations, as well as extended downtime during wind tunnel studies. These directly influence the research and development (R&D) costs and the time needed to develop a new vehicle version, eventually reflecting on the final customer.

In this thesis, a new automated workflow for studying the aerodynamics of a vehicle is introduced, with the aim to drastically reduce downtime in wind tunnels.

In this work, a prototype that demonstrates a new way of working with clay cars is tested. This paves the way to a new, more efficient and advanced investigation for an improved and better integrated aerodynamics design.

## 1.1 The importance of aerodynamics

As briefly mentioned before, customers focus has been slowly moving, in the recent years, to a new awareness of vehicle consumption and impact on the environment. With classical ICE vehicles, consumption translates into fuel consumption and efficiency, namely the maximization of kilometers that can be covered per unit of fuel. This kind of efficiency is often measured in kilometers per liter ($km/l$). Additionally, customers have also begun to take into account the emissions of $CO_2$ and other harmful pollutants, often quantified as grams emitted per kilometer ($g/km$).

In response to the growing environmental concerns, the automotive industry has undergone a significant transformation, focusing on the study, development, and sale of battery electric vehicles (BEVs). Given that this technology is still in its developmental stages and energy storage remains a prominent challenge, car manufacturers have intensified their efforts to enhance vehicle aerodynamics. The objective is to minimize energy consumption and maximize the driving range of BEVs through the implementation of streamlined designs.

Consequently, aerodynamics has assumed a pivotal role in the contemporary research and development (R&D) process, as it exerts a profound influence on various performance aspects, including vehicle range, speed, and energy consumption. To facilitate a better comprehension of this concept, a brief explanation of vehicle dynamics is covered in the following section.

### 1.1.1 Vehicle dynamics

Performances related to a road vehicles refer to the capability of accelerating, breaking and dealing with grades during a straight-line motion.

The main external forces acting a two-axle vehicle, considered as a unique rigid body, are shown in Figure 1.1.

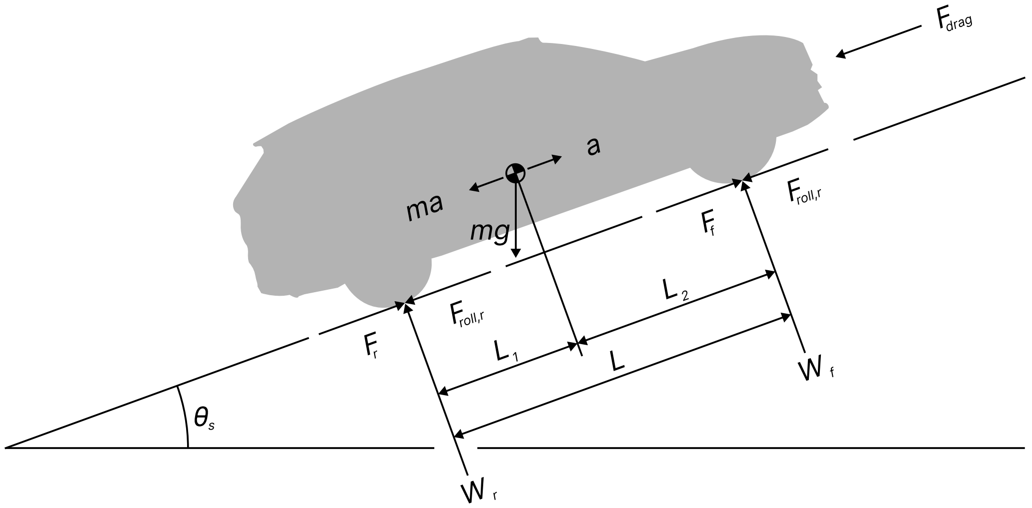

**Figure 1.1:** Forces acting on a two-axle vehicle, according to [1].

$F_r$ and $F_f$ correspond to the tractive forces [1] that allow the actual motion. These forces originate from the rotational motion of the wheels, driven by the engine. For a rear-wheel-drive vehicle, $F_f = 0$, whereas for a front-wheel vehicle, $F_r = 0$.
$F_g$ represents the grade resistance experienced by a vehicle when it is in motion on an inclined surface. This force is inherently dependent on the sine of the angle of inclination, being defined $F_g = m\,g\,\sin\theta_s$.
$F_{roll,r}$ and $F_{roll,f}$ correspond to the rolling resistances, caused by the surfaces of contact between the ground and the tyres.
The force denoted as $F_{drag}$ represents the aerodynamic drag force resulting from the movement of the vehicle within the surrounding airflow. This force is directly proportional to the square of the velocity. Its magnitude is significantly influenced by the design of the vehicle, specifically dependent on the exposed surfaces and the aerodynamic flow separation occurring at the rear section of the car.
Finally, although not explicitly reported in the diagram, it should be noted the presence of two significant forces: lift force ($F_{lift}$) and downforce ($F_{down}$). These forces arise due to the vehicle's horizontal movement, where it assumes a role similar to that of an airfoil within the airflow. It is important to highlight that while the disparity between these latest two forces does not directly affect the vehicle's efficiency, it greatly influences its stability, particularly when operating at high speeds.
Considering the longitudinal axis in Figure 1.1, it is possible to design the equation of motion, here reported in Equation 1.1

$$m\,\ddot{x} = F_{t,r} + F_{f,f} - F_{roll,r} - F_{roll,f} - F_{drag} + F_g \tag{1.1}$$

By introducing the concept of inertial force $F_i = m\,\ddot{x}$ and by summing all the rolling resistance contributions in one term $F_{roll}$, the equation above can be rewritten as

$$F_t = F_{roll} + F_{drag} + F_g + F_i \tag{1.2}$$

with $F_t$ total tractive effort.

From Equation 1.2, however, it is not immediate to understand the correlation between traction force and efficiency. By recalling the definition of energy

$$E = \int F(t)\, v(t) \delta t \tag{1.3}$$

is is possible to estimate what is the total energy required to a vehicle for guaranteeing a specific motion. Naturally, the less energy is used for assessing the exact same movement, the more efficient. For this reason, Equation 1.3 can be interpreted as energy consumption from a vehicle perspective

$$E_{consump} = \int F_{tot}\, v_{vehicle}\, \delta t$$

The definition of energy, written is such manner, is simple to decode. $v_{vehicle}$ is a function of time and, unless ADAS or fully-autonomous driving are implemented, it entirely depends on the driver and cannot be optimized. By assuming this statement, it is immediate that energy consumption minimization comes only with the minimization of $F_{tot}$, and thus its factors.

As mentioned before, $F_i$ depends on the vehicle inertia and, unless a car manufacturer company starts making lighter-weight vehicles, it is hard to reduce its contribution. $F_g$, instead, depends on the plane inclination and its contribution depends on the surrounding topography and environment. It is of course a parameter that cannot be controlled and additionally, for pure horizontal motions, its magnitude goes to zero.

The only remaining factors that might be reduced for achieving efficiency are the rolling resistance $F_{roll}$ and the drag force $F_{drag}$. In the automotive industry, they are indeed the most studied agents and dedicated departments focus on minimizing them.

The definition of rolling resistance is reported in Equation 1.4

$$F_{roll} = -f_R\, m\, g \tag{1.4}$$

with $g$ gravitational acceleration, $m$ vehicle mass and $f_R$ rolling coefficient. In particular, the latter may change with the steering, as it is a function of slip angle and lateral adherence coefficients and, based on experimental data, it was demonstrated to change with the vehicle longitudinal velocity. In [1], an empirical formula was proposed to define the rolling coefficient, based on radial-ply passenger car tires data, reported here as Equation 1.5.

$$f_R = 0.0136 + 0.40 \times 10^{-7}\, V^2 \tag{1.5}$$

with $V$ vehicle speed, in $km/h$.

Since it depends of the tire inflating pressure and the type of ground surface, to reduce it, a tire optimization should be conducted, but this is not the focus of this thesis. Additionally, the rolling resistance does mainly affect the vehicle dynamics at low speed, while at high velocities the aerodynamic drag becomes the main resistance force, as illustrated in Figure 1.2.

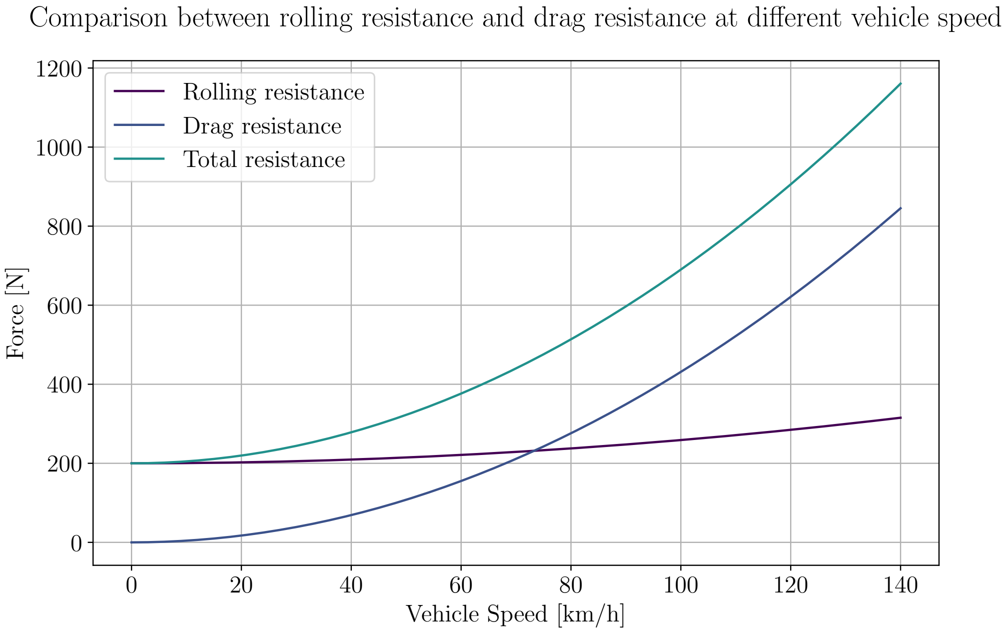

**Figure 1.2:** Rolling resistance and aerodynamic drag of a representative SUV. Rolling resistance coefficient from Equation 1.1 in [1]. Weight of the vehicle chosen to match Figure 2.5 in [2]. The area and drag for the SUV were calculated using the mean area and drag coefficient of the vehicles presented in [3] and [4]. SUV mean $C_D = 0.358$, mean $A = 2.626\,m^2$.

On the other hand, the definition of aerodynamic drag is reported in Equation 1.6

$$F_{drag} = \frac{1}{2}\,\rho\,C_D\,A\,v^2 \tag{1.6}$$

with $\rho$ representing the density of the fluid the car is located in, $C_D$ its drag coefficient, $A$ the cross sectional area and $v$ the relative speed of the vehicle to the fluid.
Particularly, $C_D$ is a dimensionless quantity used to represent the overall resistance of an object. It summarizes the contribution of skin friction and form drag. The former is mainly related to the viscosity of the fluid and represents the friction of fluid particles on the surface of the considered body, whilst the latter is related to the shape of the body interacting with the flow and it is mainly determined by the wake separation of the flow.
Since the second one plays a major role in cars and clay bodies, the only factor that aerodynamic engineers can tune is the shape of the vehicle, to eventually reduce the overall $C_D$ and thus increase efficiency.
The work in [7] supports what just stated, reporting that the aerodynamic drag accounts for more than a quarter of the tractions energy required, based on the World Light Vehicle Test (WLTP) test cycle.
Aerodynamics, however, does not only affect efficiency and stability, but a set of different system parameter as well. As an example, a good aerodynamic study covers the cooling for battery, transmissions and brakes, the exterior durability and contamination in terms of visibility and splashes behaviour.

It is then fundamental to deeply understand and study the aerodynamics of a vehicle, to increase the quality of the product and to raise its technical specifications. In such manner, automotive companies car release more competitive products and widen their customer segment, as well as increasing their trust.
As briefly introduced at the beginning of the chapter, car manufacturers nowadays study the aerodynamics of new vehicles via a 2-step approach.
Initially, the design department proposes a digital twin of what could be a good version of the car under development. The defined CAD model is then tested and analyzed via CFD, to better understand what is its aerodynamics and come up with aero solutions. A sequence of redesign iterations occurs, according to the feedback that aerodynamic engineers provide to designers and new versions of the model are tested as a result.
Once a stable design version is reached, a full-scale clay car model is built and tested in the wind tunnel facility, to collect more accurate data about drag and lift coefficients, as well as other crucial parameters.
A clay car model, shown in Figure 1.3, is a full-or-scaled copy of a vehicle whose aim is to allow realistic aerodynamic tests without building a complete vehicle. Starting from a foam core, layers of clay are applied sequentially, to provide a surface that can be easily carved but able to maintain the given design. Initially done by hand, nowadays clay car carving is applied by multi-axis milling machines. After an initial roughing phase, during which most of the material is removed, a sequence of increasing precision machining follows. Additionally, clay car models include metallic and plastic components, such as steering mechanism, hoods, side mirrors, as well as a fully-functional suspension systems, to better mimic the real vehicle properties.
The clay car testing represents an important step in the workflow since it allows to test different scenarios, namely different wind speed and yaw angle combinations, in a short period of time.
Finally, the tests provide additional feedback allowing to continue the iteration process. Figure 1.4 provides a visual illustration of what has just been explained.

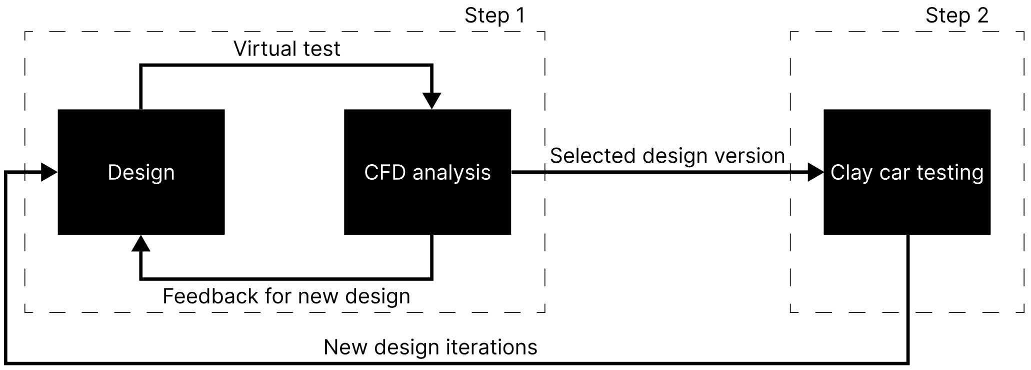

**Figure 1.4:** Design workflow to develop the most aerodynamically efficient vehicle.

Nevertheless, some downsides affect it directly, impacting on the research and development costs.
First of all, CFD and clay car analyses are not perfect methods and present some

**Figure 1.3:** Example of clay car model. In the picture a Volvo XC40 is shown, located in the Volvo Cars wind tunnel facility.

constraints. The joint usage of the methods might lead to a series of trial-and-error tests whose outcomes do not bring any insightful information nor improvement in the vehicle aerodynamic performances.

Moreover, the system as structured is highly complex and fast decisions cannot be undertaken. From the first digital version to the first wind tunnel test, several months could pass, slowing down the improvement rate and developing time.

The need of a faster and better workflow then arises, to more effectively develop new vehicles and reduce costs. In the following sections, a better explanation of the downsides associated to CFD analysis and clay car testing are discussed, to make the reader aware of why a new development workflow is needed.

### 1.1.2 Advantages and disadvantages of computational fluid dynamics

CFD is a computational technique used to analyze and solve fluid flow problems, enabling engineers to study and visualize complex phenomena and wake behaviours. CFD exploits numerical analysis to solve the equations that govern the dynamics of the fluid, such as the conservation of mass, conservation of linear momentum and conservation of energy that describe the motion of the fluid over time.

Discretization methods then play a crucial role in CFD, allowing the continuous governing equations of fluid dynamics to be approximated and numerically solved in a finite time.

Even though it is a powerful tool that allows a strong and effective analysis, it presents some downsides that limit its application in the automotive industry. To test one scenario, meaning a unique combination of wind speed and yaw angle, from 10 to 30 hours of cluster-computation are needed, slowing down the overall analysis and investigation. Consequently, to store all the information coming from few test analyses, an important memory allocation size, in the order of terabytes, is needed. Moreover, to solve the complete dynamic in finite times, CFD tools rely on physics and numerical approximations that allow to get a more or less accurate idea of the interaction of the vehicle with the flow field. However, these approximations do not allow companies to issue official certifications of their vehicles, and even internal benchmark are considered approximated compared to a real test. Furthermore, as stated in [8], CFD is mainly used for estimating the aerodynamic performance of a specific configuration and does not guarantee the identification of optimal designs. For these reasons, additional studies and tests in the wind tunnel are necessary, to provide true results by directly measuring forces on a full-or-scaled vehicle model.

### 1.1.3 Advantages and disadvantages of clay car testing

As just introduced, clay car tests in the wind tunnel become necessary to provide true, reliable results when high accuracy must be achieved. Additionally, a strong advantage in exploiting these tests is that different configuration of the vehicle can be tested in few hours, overcoming the bottleneck caused by the long computation times of the CFD analysis.

One notable benefit of utilizing wind tunnel experiments resides in the precision with which the wheel-induced flow contributions can be assessed. As evidenced in the literature, CFD analyses prevent a comprehensive investigation of these effects, relying on the utilization of simplifications and approximations that compromise the accuracy of findings.

Wind tunnel studies, as tools for testing the aerodynamics of a vehicle, are very accurate, even though open road conditions cannot be studied. As Figure 1.4 showed, they are exploited along with CFD analysis to come up with performing designs that minimize aerodynamic drag and enhance vehicle efficiency.

Downsides start rising when modifications on the vehicle designs must be introduced and then tested, as there is no automatic way for achieving this task. Consequently, aerodynamic engineers have to physically enter the facility to manually change the clay car shape, interrupting the workflow and increasing downtime, thus costs. A better discussion of those is provided in Section 1.2.

## 1.2 Current workflow in the wind tunnel

By referring again to Figure 1.4, it is possible to observe that the wind tunnel is involved only in the second stage of the workflow. Specifically, it is used once an already good and efficient design is achieved and wind tunnel data is requested. The design is thus tested along with slightly different versions of it, such as the ones characterized by different diffuser angles, wheel deflector shapes and sizes, or the presence of additional spoilers.

The continuous testing and verification of somewhat modified configurations is used for fine tuning the correct, but approximated outcome that the CFD analysis produced. In particular, this iteration process cannot be assessed via digital analysis [8] since improvements in drag coefficient or lift forces might be suppressed by numerical approximation of the software. It comes then necessary to manually test out the small but significant improvements introduced by design upgrades.

Even though wind tunnel tests can successfully satisfy this need by providing real and accurate results, the physical process comes with downsides.

It has been told in the previous sections that wind tunnel tests allow to try several vehicle configurations in a limited amount of time, definitely smaller than the one taken by the CFD analysis. Nevertheless, short amount of time does not imply efficiency. Aerodynamics engineers have to manually apply modifications and adjustments to the clay car model: to assess that, the fan that generates the wind must be started and stopped as in a swinging process. Additionally, extra waiting time for reaching the wind nominal speed is needed as well. Figure 1.5 visually illustrates what has just been explained.

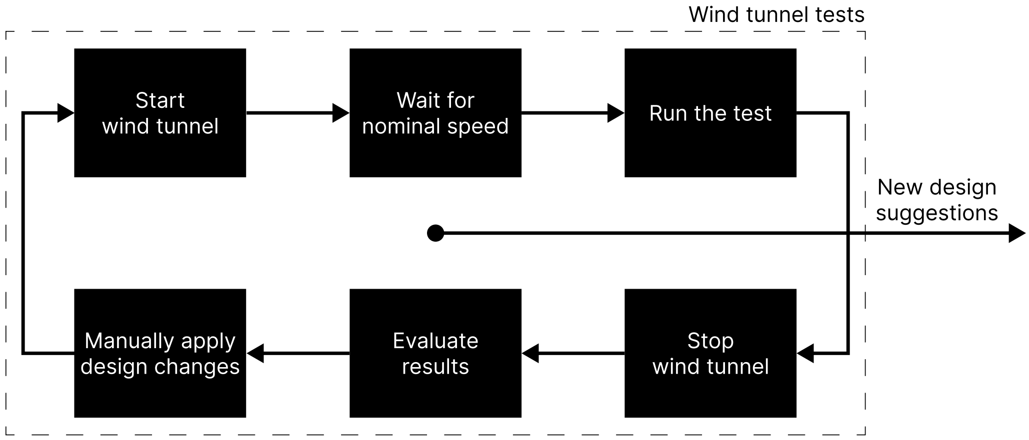

**Figure 1.5:** Current workflow for wind tunnel tests. Inefficiency and downtime characterize the system.

While dealing with complex systems such as wind tunnel facilities, efficiency matters. Downtime, namely a period of time during which no value is created for the company, represents only a cost for the industries and the missing value does not justify the energy consumption and the employed staff. A detailed discussion of that can be found in Section 3.3.

Moreover, the continuous testing of new car configurations represents the so called trial and error approach. Once data is started to be collected, engineers try to modify the vehicle design according to their previous experience, seeking more optimal configurations. Nevertheless, a car design is different from others and the introduction of components such as deflectors, diffuser or spoilers, might result beneficial for some models and generate the opposite behaviour in others. This workflow, then, leads to additional inefficiencies as it is based on attempts that might turn worthless for some cases.

The last critical point in the existing aerodynamic study is due to the precision in applying the new changes during the wind tunnel tests. Since the adjustments are manually performed, poor accuracy is introduced in the workflow. Human errors, as well as low sensitivity in the design variations might lead to inconclusive results that would have actually been interesting to investigate. It is then obvious the strong need of improving the aerodynamic optimization workflow to faster release better products on the market.

The idea of introducing an advanced design optimization based on aerodynamic performances comes from the papers [5] and [8], in which the authors tried to aerodynamically optimize the shape of buildings via cyber-physical systems (CPS). In the specific case, real scaled models of buildings were jointly used with servo-motors to adaptly change edges and create efficient designs. Because the model is undergoing physical change as it approaches the optimal solution, this approach is given the name *loop-in-the-model optimization* (LIMO) [5]. The strength of this innovative method lies in the ability by CPSs to link the real world with the cyber world, leveraging the capabilities of computers to monitor and control physical attributes. Additionally, LIMO approaches guarantee high flexibility, since they can be built around any optimization algorithm, by replacing the evaluation of a numerical model with physical testing.

For simplicity, the loop-in-the-model optimization will be referred in this work as *mechatronics optimization*. An illustration of how it works is reported in Figure 1.6.

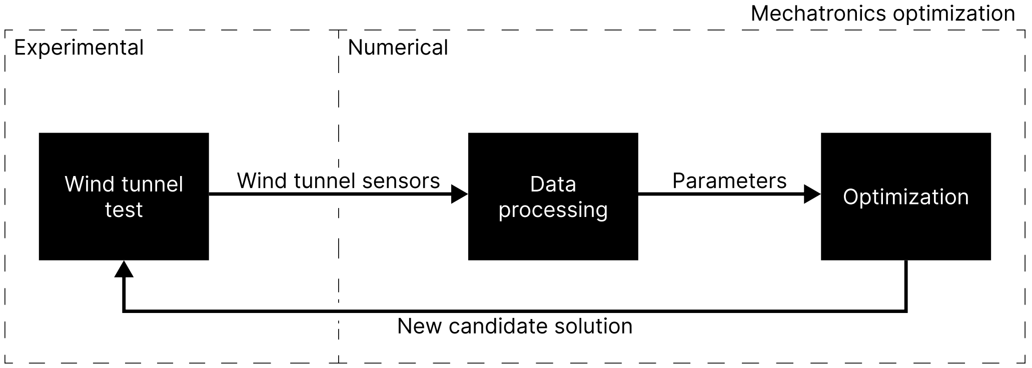

**Figure 1.6:** Diagram of CPS framework for optimal vehicle design under wind loading. Inspired by the one reported in [5], re-adapted for the specific case.

## 1.3 Mechatronics automation and optimization

A similar implementation of what just discussed was realized by Urquhart in [9]. In the paper, the author optimized the angles of small trailing edge flaps on a base cavity of a full-scale sports utility vehicle placed in a wind tunnel. The work led to high performance results but it was focused more on the optimization of the vehicle design.

This thesis differentiates from [9] by implementing a smooth and seamless workflow that optimizes car designs by automating wind tunnel tests and introducing advanced clay car models. The focus, then, does not only cover the design or the optimization part, but aims to create a new way to interact with the wind tunnel

facility and realize a so-called efficient plug-and-play system to reduce downtime.
The schematic of the new workflow proposed in this thesis is shown in Figure 1.7, in which the Mechatronics optimization box summarizes the CPS framework illustrated in Figure 1.6. As it possible to observe, the new proposed procedure is simpler than the one reported in Figure 1.5 and, as mentioned in Section 1.2, completely automated.
In section 1.4 the system design requirements for the mechatronic system are introduce while the illustration of the implementation will be covered in Chapter 2.

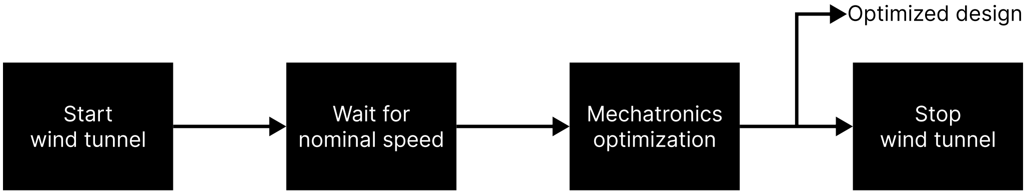

**Figure 1.7:** New proposed workflow for wind tunnel tests. The mechatronics optimization box represents the LIMO of Figure 1.6.

## 1.4 Thesis objectives

After the introduced knowledge about how a vehicle is developed from an aerodynamic perspective, it is clear the need of developing a new, automated workflow that relies on optimization algorithms to detect potential efficient and innovative designs.
This research, however, is not only carried out for improving the literature and better understand the strong impact that optimized configurations might have in terms of range and energy consumption. The additional goal is to provide a new, flexible way for Volvo Cars Corporation, the sponsor of this project, to interact with its wind tunnel facility and fasten the aerodynamic study of its incoming vehicles to eventually realize better products.
To assess this standard, in agreement with the company, some system design requirements have been chosen, to create a seamless workflow that could interact with the already existing technology, as well as be ready for supporting more complex mechatronics-actuated vehicles.

- The system must be scalable, it must support from 1 to N moving components (parameters)
- The system must be plug-and-play, it must be easy to use even for non-technical experts. Nothing is hardcoded and system values can be updated over time
- Introduction of active communication with the wind tunnel facility. Not only data must be read, but information such as yaw angles or wind speed can be commanded for future cross-yaw or varying-wind speed optimizations
- The system must be easily upgraded, with the chance of adding new optimization algorithms even written in different coding languages
- The system must be highly tunable, allowing the declaration of sampling budgets, specific ranges and dimensions of the search space to investigate

- The system must support mono- or multi-objective optimization

## 1.5 Outline

The first part of this thesis, already covered, illustrates the reasons why aerodynamic optimization is such important while developing a vehicle and what are the limitations of the current workflow.
Further, the methodology chapter explains the test facility, the test rig and the mechatronic solutions introduced for respecting the system design criteria.
After that, a detailed illustration of the gathered data and the successful results obtained follows, paving the way for advanced aerodynamic studies in the future.
Finally, some concluding remarks and possible future work is presented.

# 2

# Methodology

The successful implementation of mechatronics solutions requires the development of a seamless system that facilitates an uninterrupted flow of data between the agents involved. Accomplishing this task poses significant challenges.

To address this issue, it is necessary to first gain a deep understanding of how to construct such a system and to identify the key agents involved in data transmission and processing. Once this is achieved, the next step is to construct a test rig and implement the optimization software. This chapter aims to explore the methods and processes used to a seamless mechatronics system that steered and defined by a continuous flow of data.

## 2.1 System architecture

Volvo Cars currently studies the aerodynamics of early prototypes and clay car models as described in Chapter 1, with all the pros and cons already discussed. After carefully analyzing the existing workflow, and considering all the requirements introduced with the system design, three agents have been identified as the major players in the construction of a more advanced mechatronics system.

1. the wind tunnel system
2. the clay car test rig
3. the optimization software

To achieve the desired goal, the wind tunnel and the test rig must interact and exchange data with the optimization software. Since the type of data that are sent and received by these two agents is different, there is no need for them to have a direct communication. Thus, the software, running on a dedicated machine called here *optimization computer*, will act as a server, namely receiving evaluated data points and forwarding new sets of parameter variables. By facing the problem in this way, the system can be schematized as reported in Figure 2.1.

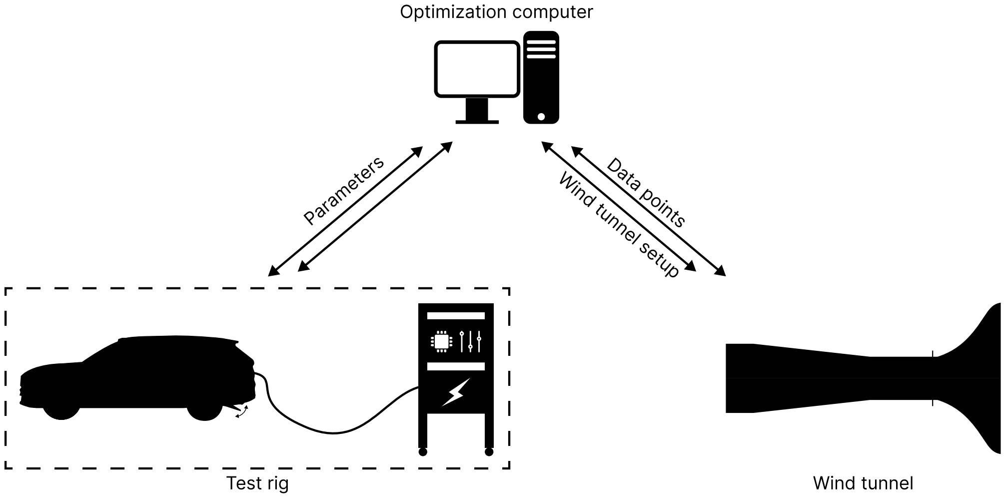

**Figure 2.1:** System architecture and data flow for the mechatronics implementation.

To build an effective system, it is crucial to overcome a significant challenge: establishing seamless communication between its various components. Once the system's structure has been understood, the focus shifts to addressing the complexities of data transmission and processing. Specifically, to enable a smooth and continuous data flow, the following issues must be optimized:

1. Communication with the test rig and the motors
2. Communication with the wind tunnel and its software
3. Realization of a software that can both handle the communications and the optimization

Each point will be broken down and analyzed in the following sections.

### 2.1.1 Test rig communication

In this first mechatronics prototype, the motors that govern the flaps are driven by microcontrollers, namely low-power computers on single integrated circuit. Due to this, a lightweight and reliable communication protocol must be adopted for high performances. Moreover, due to the potential intense data traffic and the length of cables, the network on which the system relies could be unstable or affected by high latency. For all these reasons, among the several alternatives, the MQTT protocol was adopted, as it supports all the requirements for supporting this scenario.

According to its definition, Message Queuing Telemetry Transport (MQTT) is a lightweight messaging protocol designed for devices with limited computing capabilities and for low-bandwidth, high-latency, or unreliable networks.

The MQTT protocol follows a publish-subscribe messaging model, where a client publishes a message to a broker with a specific topic, to which other clients subscribe for receiving the message. A broker, on the other hand, is a small computer that acts as a server or gateway. It is responsible for collecting messages from all the publishers and forwarding them to the right subscribers.

Additionally, the protocol supports three levels of Quality of Service (QoS), which provide different guarantees of message delivery. The QoS introduces an even higher flexibility, as high-priority messages can be temporary stored on memory while handshake procedures are adopted to verify the actual message delivery.
In this particular case, the microcontrollers and the optimization software act both as MQTT publishers and MQTT subscribers to correctly exchange data and achieve the desired motion. An additional low-power computer is needed to play the role of the broker. By creating such a system, the test rig is one step closer to the required plug-and-play behavior, as it becomes fully functional without leaning on external devices for handling the message forwarding. To use that, indeed, it is only necessary to join the local network via Ethernet connection and publish the right commands on the correct MQTT topics. An example of this setup can be found in Figure 2.2 while a better explanation of the test rig can be found in Section 2.2.

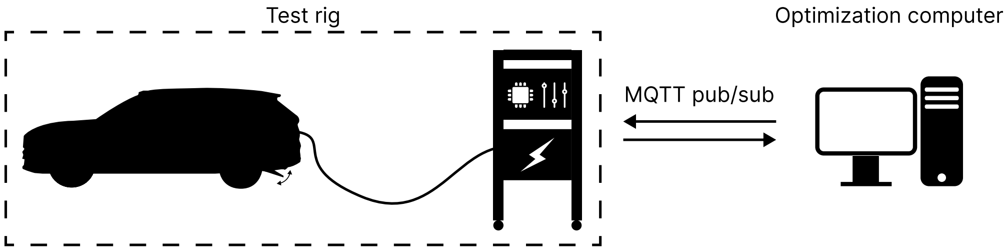

**Figure 2.2:** System architecture and data flow for the mechatronics implementation.

### 2.1.2 Communication with the wind tunnel

Establishing a proper communication with the wind tunnel is one of the major challenges faced during the implementation of this project. In the past, other researchers and engineers at Volvo Cars used to read information from the tunnel in heuristic ways. One example is the work by Urquhart [9], where analog voltage signals from the wind tunnel balance were used to get data points.
Even though this approach resulted to be effective, uncertainty and errors were introduced, as a cascade of signal conversions and manipulations were performed. Moreover, voltage signals had to be scaled in order to create a correlation between their magnitudes and the measured $C_D$ values.
Additionally, with that approach time-averaged values of $C_D$, $C_{LR}$, $C_{LF}$, offered by the wind tunnel software could not be retrieved, as digitally computed and not physically available.
Due to the need of finding better solutions to interact with the existing system, alternative approaches were considered. After few months of discussions and tests, an optimal and reliable answer was found in the Modbus-TCP/IP protocol.
Modbus is a simple and widely used industrial communication protocol that is used to send data between industrial devices. When TCP/IP protocol is used as transport layer instead of a standard serial communication, the protocol is referred to as Modbus-TCP/IP. Its advantage is to allow devices to connect over Ethernet, making it easier to communicate over longer distances.

In more detail, the communication and exchange of information occur only via Transmission Control Protocol (TCP), as it can handle and prevent possible data loss. Recalling its theory, the protocol is connection oriented, meaning that a connection must be established before sending actual data. In this method, one device listens to connection requests (passive open) from other devices. The former are known as server whilst the latter as clients.

Acknowledged that, existing constraints in the wind tunnel software made it behave only as TCP client, therefore the optimization computer, unconstrained and more flexible, had to assume the role of TCP server.

Data request and interpretation is instead delegated to the Modbus protocol. Almost in an opposite way, this standard works with the master-slave approach: a good explanation of how it works is provided by Schneider Electric [10] and here summarized

- Only 1 master is connected to the network at a time.
- Only the master can initiate communication and send requests to the slaves.
- The master can address each slave individually using its specific address or all slaves simultaneously using address 0.
- The slaves can only send replies to the master.
- The slaves cannot initiate communication, either to the master or to other slaves.

The wind tunnel software already exploits a Modbus-TCP/IP communication to gather information from different devices, such as pressure and humidity sensors. Due to their slave nature, the main software plays the role of the master, querying requests to update data only if needed. Nevertheless, since only one master can run at a time on a specific network, to run the mechatronics, and at the same time being able to interact with the sensors, the optimization computer needs to behave as a slave. This new system and its setup is well summarized in Figure 2.3.

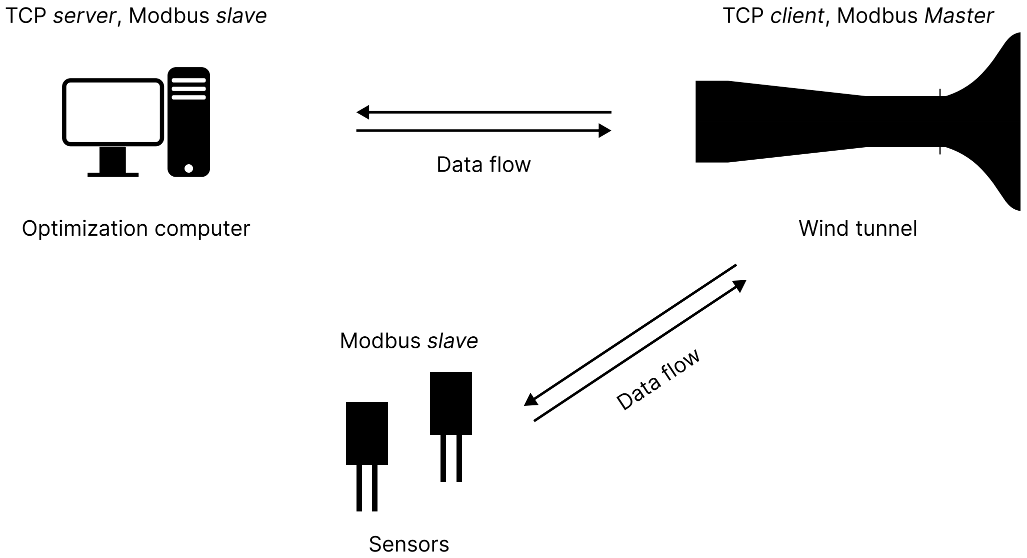

**Figure 2.3:** System architecture and data flow for the mechatronics implementation.

A clever solution would hence be to make the new computer act as a PLC device on the network, to mimic the other sensors behavior and work along with them. To successfully achieve this, a portion of the optimization machine memory must be dedicated to Modbus registers.

Modbus registers allow data to flow continuously upon master requests. They can be divided in four categories, listed in Table 2.1.

| Data Type | Access Mode | Size | Address Range |
|---|---|---|---|
| Coil | Read-write | 1 bit | 00001 – 09999 |
| Discrete input | Read-only | 1 bit | 10001 – 19999 |
| Input register | Read-only | 16 bits | 30001 – 39999 |
| Holding register | Read-write | 16 bits | 40001 – 49999 |

**Table 2.1:** Modbus register types, including memory allocation and possible ranges.

Even though each register type has its own purpose, it is frequent to find all I/O mapped to holding registers only. To ease the workflow, this implementation allocates all the data to holding registries as well.

## 2.2 Test rig

A early prototype of the test rig was already developed by Koncept Center, the Volvo Cars department responsible for creating, among the rest, mechatronics proofs of concepts. This version consisted of two wide flaps mounted on a bench, to demonstrate the system capabilities and the range of motion that could be achieved.

After this stage, the prototype has been disassembled to build the final version, structured as following

- Flaps and motors mounted on a clay car
- Power box
- Control box
- Connection cables

The name of these components suggests their role in the rig system: the power box is responsible for providing power to the entire rig, the control box for handling the signals, the flap motors for assessing the physical motion and the connection cables for allowing data to flow through the system. A representation of the whole setup can be seen in Figure 2.4. Each of these parts will be better discussed in dedicated sections.

To make the system more flexible and portable, the control and power boxes were mounted on a standing rack 1.5 meters high. The rig has been created with the idea to have a flexible and modular system. Therefore a plug-and-play system is an excellent solution that allows future development, modularity and flexibility. Having this in mind, a complete setup is sketched in Figure 2.5. To use the system, then, it is sufficient to plug in one cable to the clay car and another one in the optimization computer. The setup, eventually, will look similar to the one represented in Figure 2.5.

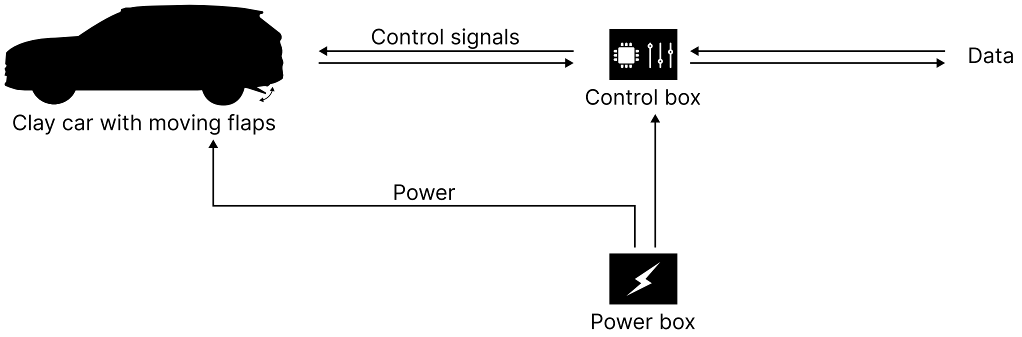

**Figure 2.4:** Schematic representation of the components in the test rig.

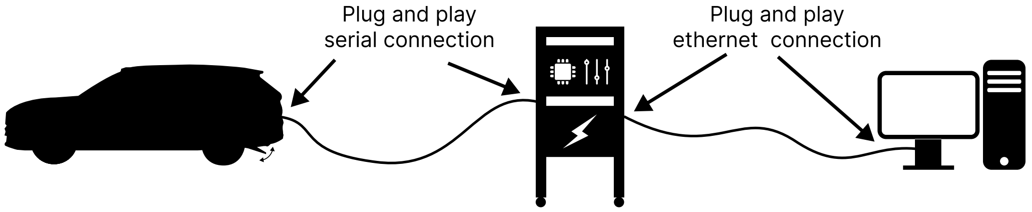

**Figure 2.5:** Plug and play test rig and agents involved.

### 2.2.1 Control box

The control box, as the name suggests, is responsible for controlling the motors mounted on the clay car and handle feedback signals. It essentially includes all the electronics that manage the test rig.

With the current design, a control box contains the following components

- Raspberry Pi
- Fuse box
- Network switch
- 4 motor controllers
- 4 microcontrollers

Each element plays a fundamental role to make the system work.

The *Raspberry Pi* runs Linux and behaves as a server. Accordingly to MQTT terminology it plays the role of the broker, being responsible to forward the MQTT messages to the subscribed devices. Without it, no communication could be handled.

The *fuse box* is a set of fuses that prevents any possible shortage of the system.

The *network switch* allows the communication among the broker, the microcontrollers and the optimization software via Ethernet communication. In this implementation it is of type unmanaged, meaning that it is not responsible for assigning IP addresses to the connected devices. Therefore, it is important to correctly set the right addresses, hard-coding the value of the microcontrollers. Moreover, it is fundamental to be sure that all the devices share the same subnet mask.

In the control box, 4 different microcontrollers can be found. As briefly mentioned in the previous section, a microcontroller is responsible for moving one flap , meaning that this box implementation can support up to 4 different spoilers. In this case, ESP32-POE-ISO by Olimex were used even though less powerful chips could have

been exploited. These controllers, in particular, have enough I/O ports to correctly drive two identical motors. Consequently, wide and heavy flaps can be governed as well by using two synchronized actuators.
Claiming that the microcontrollers drive the motors is a generalization. In reality, motor signals and power are provided by the *motor controllers*. As a result, for each microcontroller a motor controller is coupled. Its output, in terms of voltage signals, will follow the microcontroller one, adding enough power to allow the motion.
The schematic representing the connections among the aforementioned components is reported in Figure 2.6.

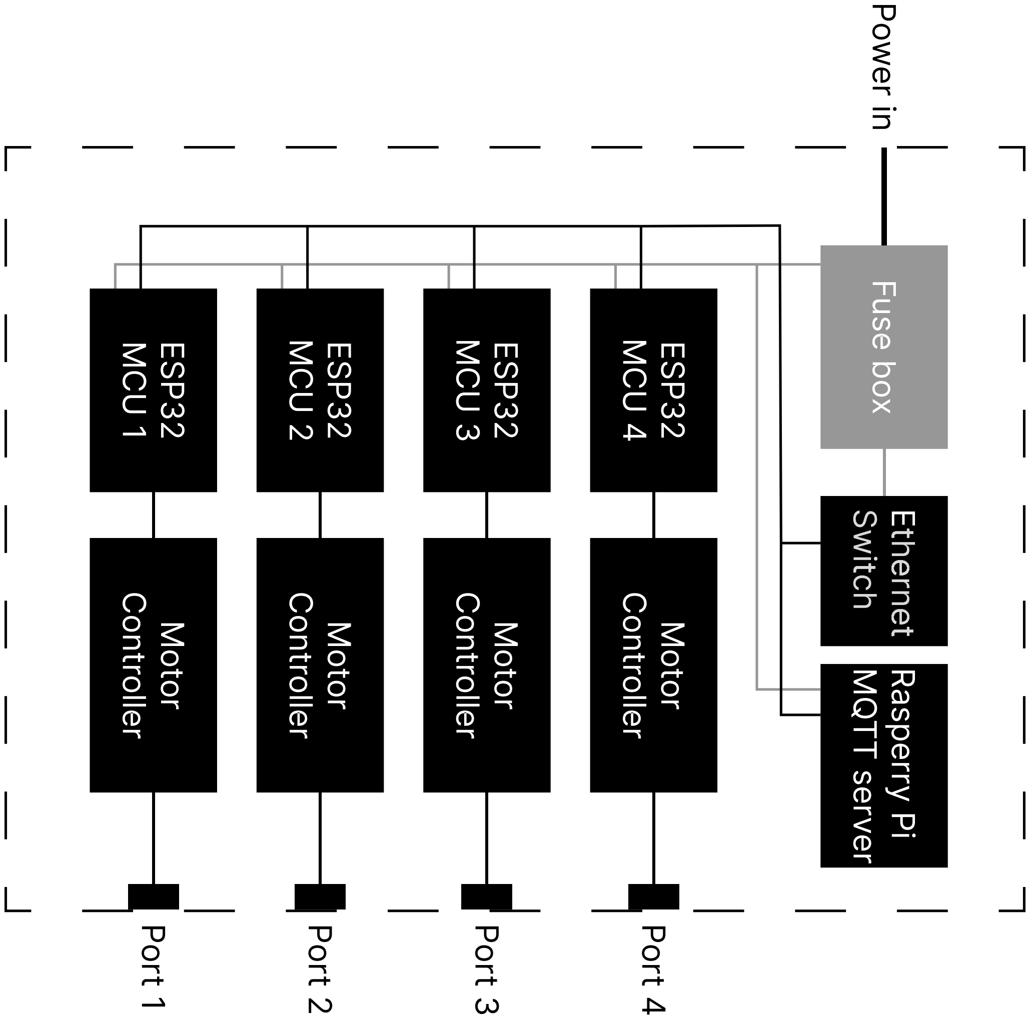

**Figure 2.6:** Control box schematic and its components.

To implement the so-desired scalability, namely the possibility to increase the number of controlled components with limited effort, the control boxes were designed accordingly. Multiple identical copies can, potentially, work along, allowing the correct management of $4N$ wings.
However, according to the MQTT rules, only one broker is necessary to receive, forward and broadcast the signals onto the network. For this reason, only one box will contain the Linux server.

### 2.2.2 Power box

The power box is responsible for powering up the test rig and making all the electronics run. Since the control box runs with two different voltage circuits, different converters can be found inside it.

In particular, the control box requires a 5V circuit for the microcontrollers, the Raspberry Pi and the network switch, and a 24V circuit to power the motor controllers and therefore the motors. Because of that, two different types of power converters can be found in the box.

The power box therefore presents multiple high-voltage converters to support the system scalability. With this design one power box can provide power up to 3 different control boxes. The limited amount of supported devices is due to space constraints for the internal components and the maximum nominal power that it can provide, set to $1200\,W$. If more than 3 control boxes were used, an additional power box is needed, following the 3-to-1 ratio.

The components inside the box are

- Earth fault protection
- AC/DC converter for low-voltage circuit
- AC/DC converter for high-voltage circuit (control box 1)
- AC/DC converter for high-voltage circuit (control box 2)
- AC/DC converter for high-voltage circuit (control box 3)

The *earth fault protection* is intended to protect equipment when an insulation fault occurs, for instance a direct contact between a life conductor and earth. In such a situation, great fault currents will flow back to the transformer through its neutral point when connected to earth.

The *AC/DC converter for low-voltage circuit* converts the standard 230V of the power grid to 5V, being able to provide the needed volts to run the microcontroller, the network switch and the Raspberry Pi.

The *AC/DC converter for high-voltage circuit* converts the standard 230V of the power grid to 24V, in order to correctly run the motors and their controllers.

In Figure 2.7 the power box schematic is reported.

Eventually, the complete schematic of the test rig is reported as Appendix 2 at the end of the document.

### 2.2.3 Flaps and motors

Briefly introduced in the sections before, the test rig includes 4 individual and identical flaps, mounted in the rear part of the car. Each flap is controlled by a motor, which movement is driven by the control box. On top of each motor rod, a 3D-printed plastic cap is mounted while a switch button is attached on top of each stator. In this way, with the rod approaching its end stop, the switch is triggered via physical contact with the cap and a stop signal is sent to the respective microcontroller. By doing so, failures or physical damages to the system are prevented and safer tests can be run, even in case values out of the allowed range of motion are sent.

The motors used for the mechatronic prototype are DINGS' MOTION 14N2215AA4250SMSN, chosen for their reliability and precision. Since they are stepmotors, no particular controllers are needed to drive them, thus avoiding the

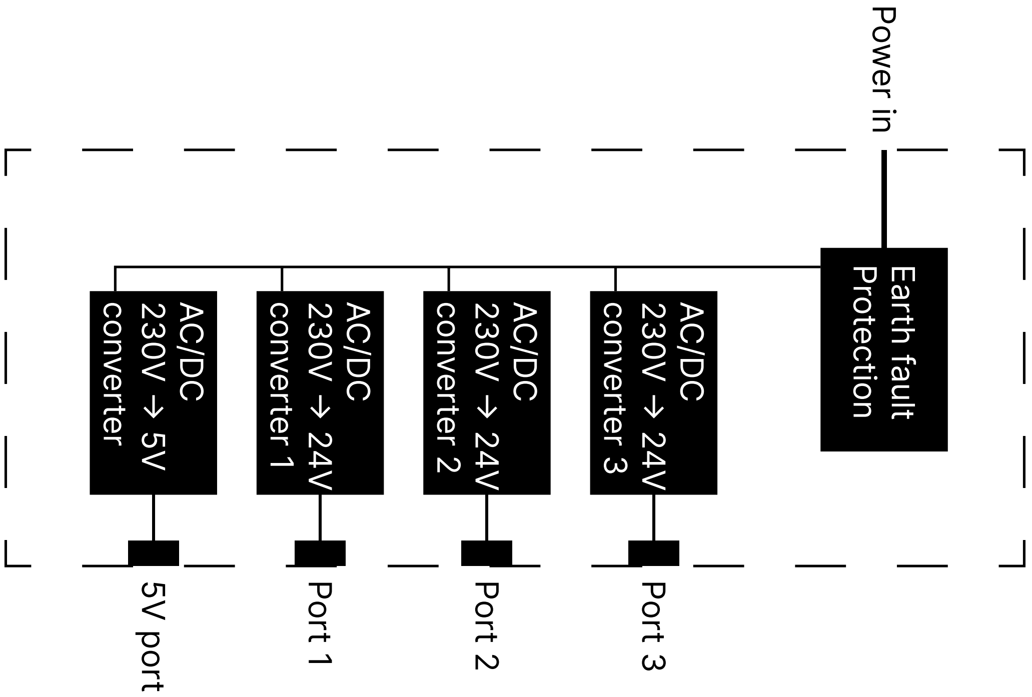

**Figure 2.7:** Power box schematic and its components.

implementation of PID or alternatives to make them reach the desired positions. Table 2.2 reports a more accurate description of the motor specifications, according to the manufacturer website.

| **Category** | **Code** | **Meaning** |
|---|---|---|
| Motors Size | 14 | 35mm |
| Linear Actuator Type | N | Non-Captive Linear Actuator |
| Step angle | 2 | 2 Phase with 1.8° |
| Motor length/Stack | 2 | Double Stack |
| Rated current/Phase | 15 | 15A |
| Lead Screw Code | AA | Code AA |
| Number of Lead Wires | 4 | 4 Flying Leads |
| Lead Screw Length / Stroke | 250 | 250mm |
| Lead Screw Surface Treatment | S | Standard [No Teflon Coating] |
| End Machining | M | Metric |
| Nut Style | S | Standard Flange Nut [External Linear Actuator] |
| Encoder Option | N | None |
| Customer Sequence Number | - | - |

**Table 2.2:** Motor specifications according to the manufacturer manual, reported on its website

The switch buttons are attached on the motors via metallic mountain brackets. They are handmade and irregularities can be found. In particular, one of those showed strong differences from the others, reducing the actual flap range of motion by 2 degrees.

To solve this issue and guarantee the same performances for each flap, the motors range of motion was limited via software, from $-10°$ to $+13°$. Additionally, due to the trigonometric calculations to convert the rod rotations to flap degrees, a sensitivity of 0.5° was achieved. This directly leads each flap to assume 46 possible configurations.

Figure 2.8 shows the CAD model of the flaps and their mounting brackets to be easily installed on the clay car vehicle.

**Figure 2.8:** CAD model of the flaps and mounting brackets used in this project.

## 2.3 Test object

The test object is a full-scale clay car model of the new Volvo EX90 SUV electric vehicle, with the test rig mounted in the rear section of the car. The flaps, thus, play the role of a small rear diffuser with variable shape.

The clay car model respects the new design guidelines dictated by Volvo, which include a small bump in the front part of the roof. This extra space is used in the latest models for allocating a LiDAR sensor to achieve Advanced Driver Assistance Systems (ADAS) capabilities.

The cooling inlets at the front part of the vehicle are closed. Since the final goal of this project is to demonstrate the capabilities that the mechatronics implementation could provide, the analysis is focused on the changes in values (deltas) rather than the actual magnitude.

For the tests, two different configurations were tested to verify the reliability of the mechatronics solution, as well as to add variety to the test object. The considered configurations are reported in Table 2.3.

| | **Configuration 1** | **Configuration 2** |
|---|---|---|
| Car | Volvo EX90 | Volvo EX90 |
| Tires | Scorpion Verde 275/40 R21 | Scorpion Verde 275/40 R21 |
| Rims | 21" Volvo Inscription | 21" Volvo Inscription |
| Front inlets | Closed | Closed |
| Roof kick | No | Rear |
| Rim coves | No | Flatter Cover 20" |

**Table 2.3:** Motor specifications according to the manufacturer manual, reported on its website

In Figure 2.9 and Figure 2.10 it is possible to observe the modification applied to the vehicle to switch from Configuration 1 to Configuration 2, as reported in Table 2.3.

**(a)** 21" Volvo Inscription rims **(b)** 20" wheel cover

**Figure 2.9:** Different wheel configurations.

**Figure 2.10:** Roof kick added for the second clay car configuration

Eventually the majority of the tests have been run using the second car configuration, as the more insightful information is the achieved deltas rather than the comparison between different car models.

## 2.4 Test facility

The wind tunnel experiments were conducted at the Volvo Cars Aerodynamic Wind Tunnel (PVT), which has the capacity to reach speeds of up to 250 km/h. For this particular research, tests were carried out at a speed of 140 km/h, resulting in a Reynolds number of $Re_{\sqrt{A}} = 4.2 \cdot 10^6$ based on the square root of the frontal area of the vehicle $A$ as characteristic length in the definition. The tunnel is a closed return type with slotted walls, featuring a test section of 27 $m^2$, resulting in a blockage ratio of around 10% for a full-scale model.

The ground simulation features a five-belt moving ground system mounted with distributed suction and scoop boundary layer control. Each belt has tangential blowers behind it that increase the appearance of the belts' length. To enable the model to yaw, the vehicle is mounted on a turntable.

In the study that is being given, only negative yaw angles are used according to the SAE standard J1594 [11], which means that when viewing the vehicle from the rear, the wind moves from left to right. Four struts, which fixate the vehicle's position and height, are used to attach the vehicle to a six-component balance.

In order to account for blockage effects, the forces and moments are non-dimensionalized to coefficients.

Figure 2.11 illustrates the wind tunnel facility and where the car is mounted during the tests.

**Figure 2.11:** Clay car mounted on the wind tunnel balance.

The wind tunnel instrumentation allows to achieve a sensitivity of 0.0005 for the drag and lift normalized coefficients, a sensitivity of 0.01 $km/h$ for the wind speed and 0.01° for the yaw value.

## 2.5 Optimization software

The optimization software represents the core of the mechatronics project, as it has to handle the communication with both the wind tunnel system and the test rig. The channels and protocols that are used to exchange data among these are explained in Sections 2.1.1 and 2.1.2. In addition to this, several criteria have been taken into account to design and realize the final product. Some of those are here reported.

- The software must run on Windows, both 32-bit and 64-bit versions
- The software must only work offline, for security reasons
- The software must be scalable
- The software must be plug-and-play
- The software must be easy to use. GUI is preferred
- The software must be safe, no risky or dangerous actions can be done
- The software must be easy to upgrade, even for non-experts.

To respect all the constraints and create a flexible and reliable product, the optimization software was developed in C# .NET Framework using Microsoft Visual Studio. This guaranteed the possibility to create a friendly user interface as well as to exploit all the computational power needed for the processes.

To realize a *scalable system*, every 2 seconds the software looks for microcontrollers connected to the network. In this way, flaps can be added or removed smoothly and effortlessly. Once a new device is detected, respective information are queried. Nothing is harcoded, meaning that the software can support from 1 to N different flaps by default. The only and known bottleneck in the system might be the MQTT broker, run on a Raspberry Pi in this implementation. With the increasing number of connected flaps in the system, data flow could be too high to be handled by such tiny computer and more powerful devices should be used.

To respect the *plug-and-play* requirement, the software tries to connect to both the wind tunnel system and the test rig every time it detects a disconnection. This leads the user to only connect the optimization computer to the other devices via Ethernet cables in order to make it work.

The optimization software was also designed to be *easy to upgrade and to use.* One of its major feature is the possibility to run optimization algorithms written in any programming language, such as C++, Python or Julia. Consequently, engineers can write their own code in the language they feel more comfortable with. The algorithms are loaded at runtime, avoiding to hardcode them in the main software.

### 2.5.1 Multidimensional control

Both monodimensional and multidimensional controls can be achieved via software by grouping the desired flaps together (from 1D to ($N$-1)D), or leaving them move individually ($N$D). In such a manner, further analysis can be conducted and symmetric constraints can be introduced to fasten the design exploration.

### 2.5.2 Optimization algorithms

As introduced before, each flaps was limited to a 23° range of motion, going from $-10°$ to $+13°$. The sign convention is reported in Figure 2.12.

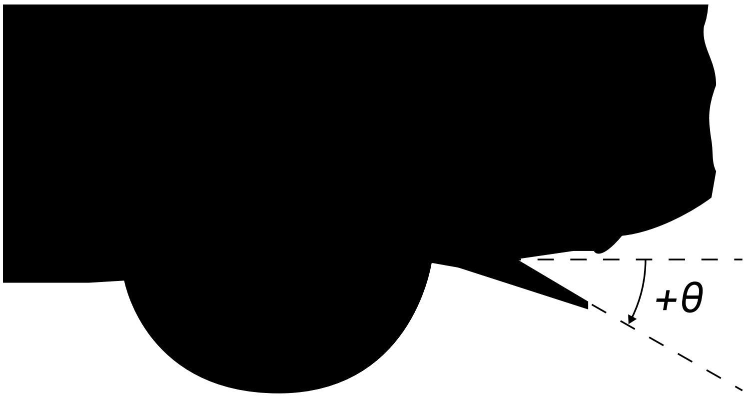

**Figure 2.12:** Side view of the flaps mounted on the clay car, showing the sign convention for the flap angles. The horizontal axis is parallel to the ground.

Since the test rig , as implemented in the software, is characterized by a sensitivity of 0.5°, each surface can assume 46 different configurations, leading to $46^4 \simeq 4.48 \cdot 10^6$ different combinations. Considering the motion time, the stabilization time and the averaging time, the system takes up to $110\,s$ to test a single configuration. It is of course unfeasible to try every combination, indeed the operation would take $4.9 \cdot 10^8\,s$, or 15.5 years of uninterrupted tests. Economic and time constraints force to find a smarter solution to solve the problem.

An effective answer consists in the introduction of optimization algorithms, which consider the clay car and the test rig as a black-box-function. The function domain becomes the flaps configuration space and the codomain the wind tunnel values, such as drag force coefficient $C_D$, front lift force coefficient $C_{LF}$ or rear lift force coefficient $C_{LR}$.

Other alternatives including deep neural network (DNN) implementations or the introduction of optimal controllers were discarded. The former, indeed, are too dependent from the car geometry, meaning that if a deep neural network such as a multilayer perceptron (MLP) is trained on a car model, it will not suit other designs due to the differences in the geometry. This might not provide the correct configuration that minimizes the targeted value, e.g. the drag coefficient.

Moreover DNN methods require large data, namely they need vast datasets to properly train the model. Sampling and gathering data from the wind tunnel is an expensive procedure that must be reduced as much as possible. The optimal configuration should then be found with the minimum collection of data points, in the minimum amount of time. Training a neural network is not compliant with these constraints.

Introducing advanced methods from the control theory such as *LQ control* implies

solving extremely complex non-linear systems that can be hardly modeled. This might increase the computational times, creating a new bottleneck in the mechatronics system that prevents the possibility to find any optimal configuration. For this reason, this approach has also been discarded.
Once understood that the optimization algorithms are the best approach to face the problem, several options from the literature have been considered. In particular, the ones taken into account and implemented via software are listed in Table 2.4.

| **Algorithm** | **Family** |
|---|---|
| Bayesian Optimization | Sequential Model-Based Optimization (SMBO) |
| Broyden–Fletcher–Goldfarb–Shanno (BFGS) | Numerical optimization |
| Latin Hypercube Sampling | Statistics |
| Nelder Mead | Numerical optimization |
| Particle Swarm Optimization | Evolutionary algorithm |
| Response Surface Modeling | Statistics |
| Sobol Sampling | Statistics |
| Surrogate model | Model-based Optimization |

**Table 2.4:** List of considered algorithms and their class description

The algorithms were intentionally chosen from different background in order to understand which suits the optimal car configuration problem the best. As it will be shown in Chapter 3, some algorithms performed better than others due to the nature of the challenge.
In addition to this, statistical sampling methods such as Latin Hypercube Sampling and Sobol Sampling were considered for two purposes. The first one is to select points from the search space in order to uniformly cover it and test configurations. In several applications, indeed, quasi-random methods perform better than optimization-oriented ones. The second one is used to initialize other algorithms in alternative ways compared to the classical Gaussian distribution. A deeper discussion of this can be found in Section 3.1.5.
Eventually, a simple *sweep* approach is also considered to make the test rig behave as a standard rear diffuser, tackling the problem as monodimensional. The sweep consists in a progressive motion from the minimum to the maximum value of the allowed input space. This approach not only brings a 1-D analysis but also economic advantages as better explained in Section 3.3.
A final note regards the surrogate model optimization algorithm just introduced. It was taken from [12] and it will be defined in this work as Urquhart Surrogate model, from the principal author of the paper.

## 2.6 Wind tunnel tests

Tests were performed for about 78 hours. The first 12 hours were used to test the communication with the wind tunnel and the test rig, while the remaining hours for

gathering data.
Different algorithms were tested at different yaw values. For the latter, 0°, $-5°$ and $-10°$ were considered. The wind speed was instead kept constant at $140\,km/h$. For denoting the positive sign of rotation the SAE J1594 [11] was used.
Different averaging times for computing the wind tunnel values were also considered: initially a $20\,s$ average was exploited, switching to a $60\,s$ for other tests, as better explained in Section 3.1.3.
The complete list of the tests done for this project can be found as Appendix 1 in the dedicated section.

## 2.7 Car efficiency and drag coefficient

The theoretical formulation and meaning of drag coefficient $C_D$ has been already introduced in Chapter 1. Through this value, it is possible to estimate the drag forces acting on a car due to longitudinal speed. Even though more complex dynamics occur, such as the contribution of side wind, the coefficient remains a good indicator of a vehicle aerodynamic efficiency.
Nevertheless, a more sophisticated relation between efficiency and drag coefficient must be considered, to better understand what possible $\Delta C_D$ values might lead to in terms of energy consumption and range.
Covering the true effect that small changes in $C_D$ values lead to vehicle efficiency is a complex study that requires a dedicated investigation, not included in the objective of this work. Nevertheless, a less precise but still reliable reasoning can be done in order to have a general idea of possible advantages the car could benefit.
Therefore, the following discussion will be called *rule of thumbs* as it provides a rough but correct idea of the relation between efficiency and drag.

### 2.7.1 The rule of thumb

As already introduced in Section 1.1, the drag force (from Equation 1.6) can be expressed as following

$$F_{drag} = \frac{1}{2}\,\rho\,C_D\,A\,v^2$$

with $\rho$ fluid (air) density, $A$ vehicle frontal area and $v$ vehicle longitudinal velocity. In order to overcome this force during the vehicle motion $\Delta s$, a precise amount of energy is required, equal to

$$E = F_{drag}\,\Delta s \tag{2.1}$$

with $E$ expressed in Joule $J$ and $\Delta s$ in $m$. Vehicle parameters, however, are usually expressed differently: distances are measured in $km$ and energy in $Wh$. Particularly, $Wh$ is the standardized way to express the amount of energy stored in BEVs. It is possible then to use those unit measures by introducing a conversion coefficient $\gamma$, namely

$$E = \gamma\,F_{drag}\,\Delta s \tag{2.2}$$

with velocity in $F_{drag}$ expressed in $km/h$. By isolating $F_{drag}$ in Equation 2.2, it is possible to obtain

$$\gamma F_{drag} = \frac{E}{\Delta s} = \left[\frac{Wh}{km}\right] \tag{2.3}$$

Looking at the unit measure obtained, $Wh/km$ can be seen as the energy consumption per kilometer of the vehicle. In other words, it represents the vehicle's efficiency, since its minimization results to be beneficial for the system.
From Equation 2.3 is it possible to observe that by multiplying $F_{drag}$ by the conversion factor $\gamma$, it is easy to switch from a force to energy consumption representation, so that

$$e_{loss} = \gamma F_{drag} = \frac{1}{2}\,\gamma\,\rho\,C_D\,A\,v^2 \tag{2.4}$$

Equation 2.4 represents the energy consumption per kilometer of a vehicle to overcome the aerodynamic drag.
According to the WLTP legislation [13] and [14], the density for dry air is $\rho = 1.189\,kg/m^3$ while the conversion coefficient is $\gamma = 0.0214$. These values leads Equation 2.4 to the case-specific version

$$e_{loss} = \gamma F_{drag} = 0.01274\,C_D\,A\,v^2 \tag{2.5}$$

WLTP legislation provides standard test cycles, called WLTP cycles, used for certification and official car range estimations in European Union. During the test, the speed is made varying over time, scoring an average velocity of $v = 82\,km/h$.
Equation 2.5, for such velocity, becomes

$$e_{loss} \simeq 86\,C_D\,A \tag{2.6}$$

while, if high speed value such as $v = 120\,km/h$ is considered, it becomes

$$e_{loss} \simeq 183\,C_D\,A \tag{2.7}$$

Additionally, WLTP legislation provides information about the claimed and actual energy losses, called vehicle consumption. This value, expressed in $Wh/km$ for electric vehicles, is the result of a complex interaction among weather conditions, vehicle dynamics, driving mode, environment and secondary systems such as infotainment or ADAS.
Nevertheless, for this work the vehicle consumption can be generalized to be due to only vehicle resistance. By recalling the mathematical manipulation obtained in Equation 2.3

$$e_{loss,\,tot} = \gamma F_{res}$$

A further simplification can be done. The total vehicle resistance $F_{res}$, indeed, can be safely broken down in two main factors: rolling resistance $F_{roll}$ and air drag resistance $F_{drag}$

$$F_{res} = F_{roll} + F_{drag} \tag{2.8}$$

leading to the simplified definition of energy losses

$$e_{loss,\,tot} = \gamma F_{res} = \gamma\left(F_{roll} + F_{drag}\right)$$

The WLTP official ratings for the Volvo EX90 are reported in Table 2.5, according to data reported in [6].

| | | | |
|---|---|---|---|
| Range | 585 km | CO2 Emissions | 0 g/km |
| Rated Consumption | 209 Wh/h | Rated Fuel Equivalent | 2.3 l/100km |
| Vehicle Consumption | 183 Wh/km | Vehicle Fuel Equivalent | 2.1 l/100km |

**Table 2.5:** WLTP ratings reported in [6]. Rated = official figures as published by manufacturer. Rated consumption and fuel equivalency figures include charging losses. Vehicle = calculated battery energy consumption used by the vehicle for propulsion and on-board systems.

Even if Volvo Cars claimed both rated consumption and rated fuel equivalent values, it is better to consider the values obtained during the WLTP test.
Since the mechatronics project does not involve rolling resistance optimization, it is possible to break down the total vehicle consumption in a constant factor, $F_{roll}$, and a optimizable contribution, $F_{drag}$.
In order to evaluate the reduction in energy consumption $\Delta e_{loss,\,tot}$ after a possible optimization, the following reasoning can be done

$$\begin{aligned}\Delta e_{loss,\,tot} &= e_{loss,\,tot,\,new} - e_{loss,\,tot,\,old}\\ &= \gamma\left(F_{roll,\,new} + F_{drag,\,new}\right) - \gamma\left(F_{roll,\,old} + F_{drag,\,old}\right)\end{aligned}$$

Due to the constant nature of $F_{roll}$ in this project, $\Delta e_{loss,\,tot}$ becomes

$$\Delta e_{loss,\,tot} = \gamma\left(F_{drag,\,new} - F_{drag,\,old}\right) \tag{2.9}$$

and by recalling the definition of $F_{drag}$, Equation 2.9 turns into

$$\Delta e_{loss,\,tot} = \frac{1}{2}\gamma\,\rho\,\Delta C_D\,A\,v^2 \tag{2.10}$$

assuming the front area $A$ and the vehicle speed $v$ constant.
Equation 2.10 allows to estimate the potential reduction in energy consumption via minimization of the drag force. For this specific case, recalling Equation 2.6, Equation 2.10 turns into the actual rule of thumb

$$\Delta e_{loss,\,tot} = 86\,\Delta C_D\,A\,v^2 \tag{2.11}$$

In [6] the usable battery capacity $C_{battery}$ is also reported, smaller in magnitude than the nominal one claimed by the company. In particular, a 107 $kWh$ battery capacity was rated. This value allows to convert energy consumption in car range

$$Range = \frac{C_{battery}}{e_{loss,\,tot}} = \frac{107\cdot 10^3}{e_{loss,\,tot}}$$

By considering the non-optimized vehicle consumption, a total range of about 585 $km$ can be achieved. If the energy losses can be even more minimized via the mechatronics approach, higher values could be obtained.
In Chapter 3 considerations about possible efficiency and range improvements will be covered.

# 3

# Results

In this chapter, all data resulting from this work are gathered and analyzed. The main objective is to quantify the benefit of an automated mechatronic solution when incorporated into traditional wind tunnel tests. Results are compared in terms of costs savings and performances.

This chapter is divided into two main sections. First, a validation study is conducted. Optimization algorithms, averaging time and minimum number of samples are discussed. Next, the core of the work is presented, and the advantages that an automated mechatronic system can bring to traditional wind tunnel experiments is discussed in details.

## 3.1 Validation

As just mentioned, here below a series of choices that have been made during the realization and the startup of this project are presented.

### 3.1.1 Benchmark functions

One of the first analysis to be conducted has been the benchmarking and ranking of the developed optimization algorithms. This was done due to the need of maximizing the quality of the obtainable results from the test days, by using the most effective strategies and techniques.

Few benchmark functions, reported in Table 3.1, were introduced. The targeted algorithms were evaluated on those, by assessing different behavioural tests. In particular, only 2D functions were considered, to be able to visualize them and easily judge the quality of the results.

| **Function** | **Definition** |
|---|---|
| Stybliski-Tang 2D | $\frac{1}{2}\sum_{i=1}^{2}\left(x_i^4 - 16x_i^2 + 5x_i\right)$ |
| Rastrigin 2D | $20 + \sum_{i=1}^{2}\left[x_i^2 - 10\cos(2\pi\, x_i)\right]$ |
| Rosenbrock 2D | $100\left(x_2 - x_1^2\right)^2 + (x_1 - 1)^2$ |
| Beale 2D | $(1.5 - x_1 + x_1\, x_2)^2 + \left(2.25 - x_1 + x1\, x_2^2\right)^2$<br>$+ \left(2.625 - x_1 + x_1\, x_2^3\right)^2$ |
| Sphere 2D | $\sum_{i=1}^{2} x_i^2$ |
| Perm d, $\beta$ 2D | $\sum_{i=1}^{2}\left(\sum_{j=1}^{2}\left(j^i + \beta\right)\left(\left(\frac{x_j}{j}\right)^i - 1\right)\right)^2$ |
| Goldstein-Price 2D | $\left[1 + (x_1 + x_2 + 1)^2 \times\right.$<br>$\left.\left(19 - 14x_1 + 3x_1^2 - 14x_2 + 6x_1x_2 + 3x_2^2\right)\right] \times$<br>$\left[30 + (2x_1 - 3x_2)^2 \times\right.$<br>$\left.\left(18 - 32x_1 + 12x_1^2 + 48x_2 - 36x_1x_2 + 27x_2^2\right)\right]$ |
| Ackley 2D | $-\,a\,\exp\left(-b\sqrt{\frac{1}{2}\sum_{i=1}^{2} x_i^2}\right) - \exp\left(\frac{1}{2}\sum_{i=1}^{2}\cos(c\, x_i)\right)$<br>$+\,a + \exp(1)$ |
| Bohachevsky 2D | $x_1^2 + 2x_2^2 - 0.3\cos(3\pi x_1) - 0.4\cos(4\pi x_2) + 0.7$ |

**Table 3.1:** Benchmark function names and their mathematical definition.

Each benchmark function has its own magnitude. In order to facilitate the comparison, as well as lead the analysis on more case-oriented scenarios, a scaling has been applied, narrowing the interval to $f(X) \in [0.20; 0.35]$. Reducing the output to this narrow span allows to get values closer to real car drag coefficients. Specifically, a linear scaling has been applied, according to Equation 3.1.

$$F_{scaled}(x) = \frac{F_{max} - F_{min}}{f_{max} - f_{min}} \left(f(x) - f_{min}\right) + F_{min} \tag{3.1}$$

where $F_{min} = 0.20$ is the new desired minimum and $F_{max} = 0.35$ is the new desired maximum. Instead, $f_{min}$ and $f_{max}$ are the original minimum and maximum of the functions.

The search space and the respective scaled output space of the functions are shown in Figure 3.1.

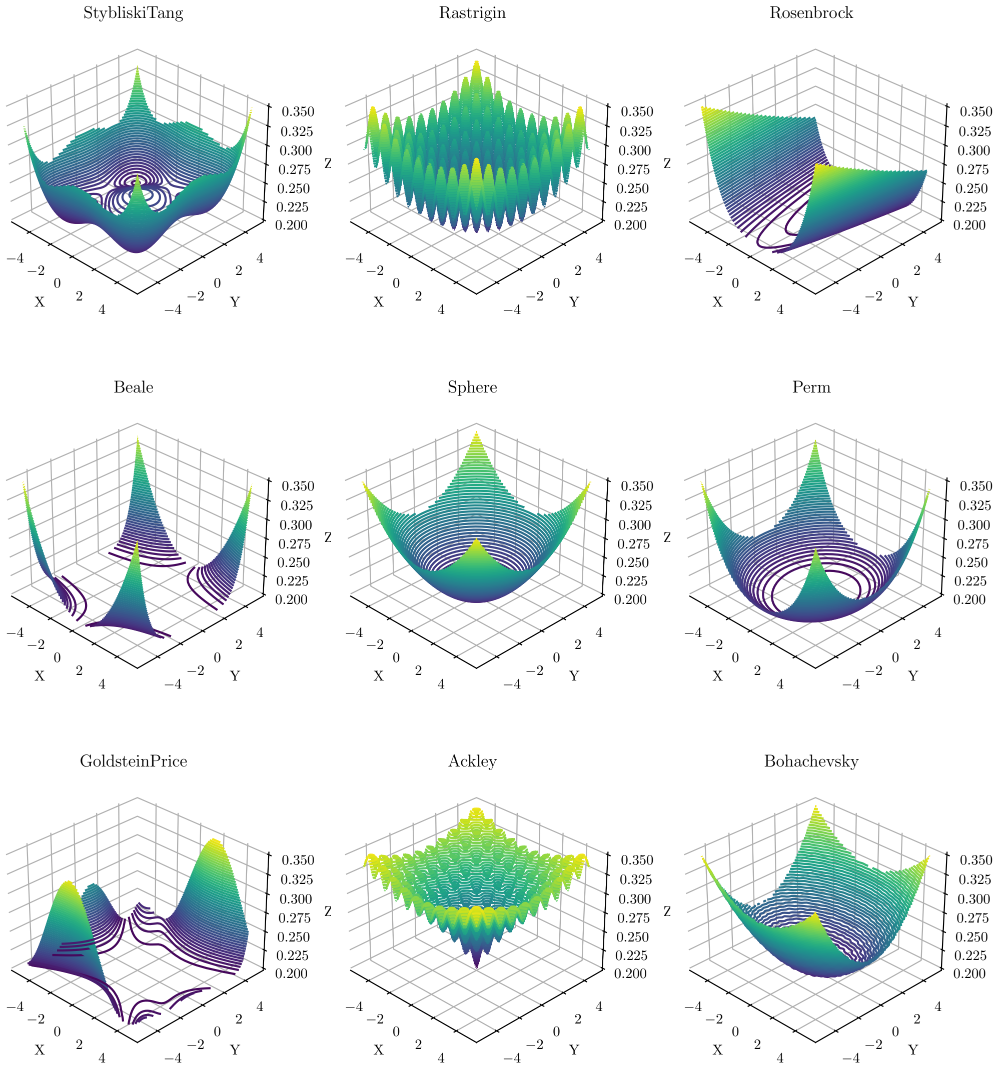

**Figure 3.1:** 3D visualization of the considered benchmark functions. Search space is represented by the $xy$-plane, while the output space is displayed on the $z$-axis.

Another interesting visualization of the benchmark functions is the one proposed

in Figure 3.2, in which the distribution of local maxima and minima can be read more easily. In the following sections, all the introduced benchmark functions will be considered to evaluate the algorithms performances, even though more attention will be given to Sphere, Perm, and Bohachevsky functions.
The particular focus on these three specific functions is due to their convex characteristic: it is assumed, in this pilot project, that the problem associated to clay car aerodynamic optimization via mechatronic diffuser is convex, or at least that it does not exhibit plenty of local minima, as for example the Ackley function.

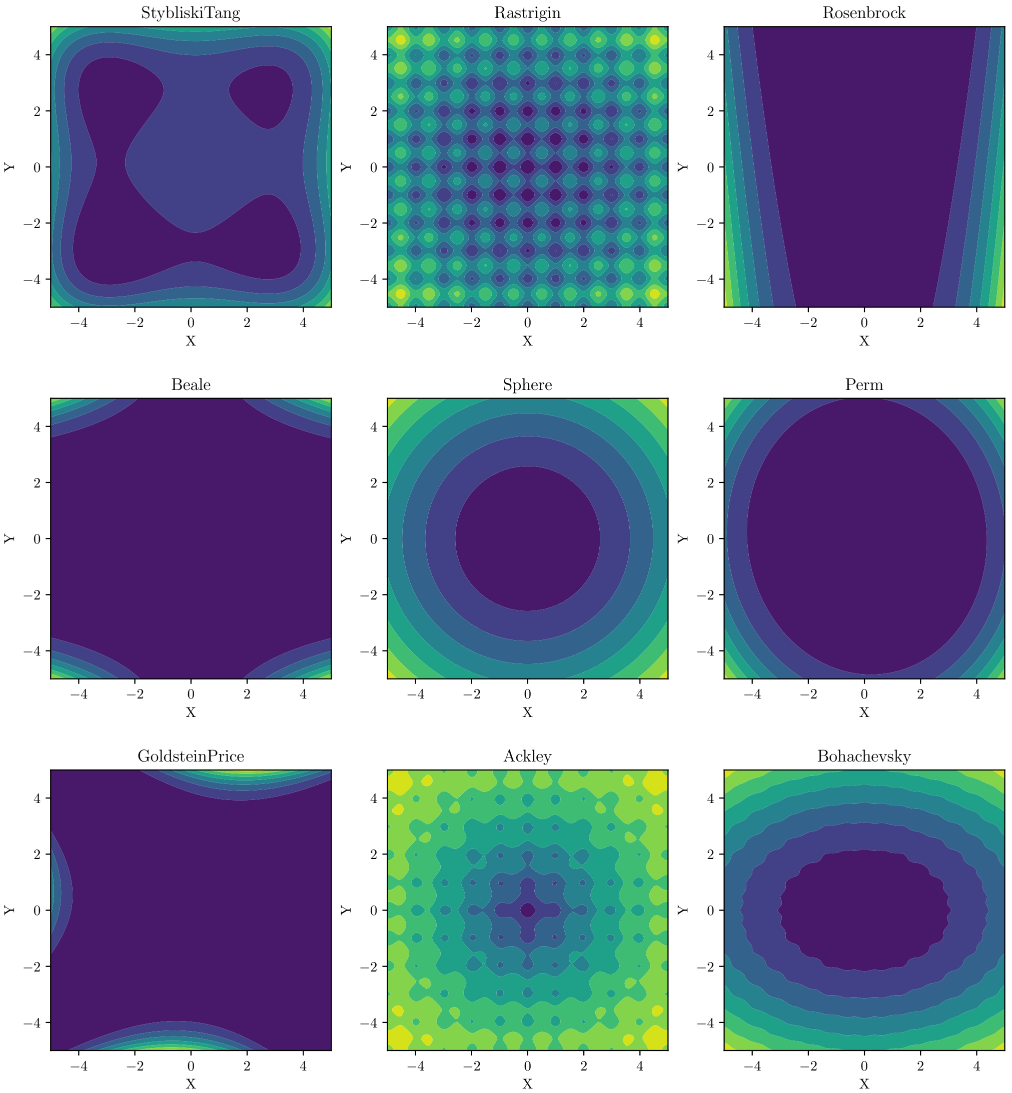

**Figure 3.2:** 2D visualization of the considered benchmark functions. The function has been color-mapped accordingly to the function values.

Additionally, it is believed that the black box function coming from the clay car model has a gradient significantly different from zero, leading to true and effective optimization possibilities. Functions such as Goldstein-Price or Beale, characterized by strong flat regions, do not show this behavior, thus less importance will be given to the performances coming from them.

### 3.1.2 Optimizer comparison

To understand which algorithms perform better than others, the optimizers have been tested on the benchmark functions to get insights on their performances. Specifically, the optimization algorithms were provided with a sampling budget of maximum 100 values. This number was chosen arbitrarily but with the condition to be high enough to make the algorithms work. In reality, a lower budged is considered, due to the expensiveness of interacting with the wind tunnel, in terms of costs and time. A more detailed discussion of this can be found in section 3.1.4.
Additionally, the algorithms have been run 250 times on each benchmark function, in order to estimate their average behaviour (mean) and confidence (standard deviation). This is due to the fact that some optimization processes are not systematically but stochastically initialized, as illustrated in Section 3.1.5.

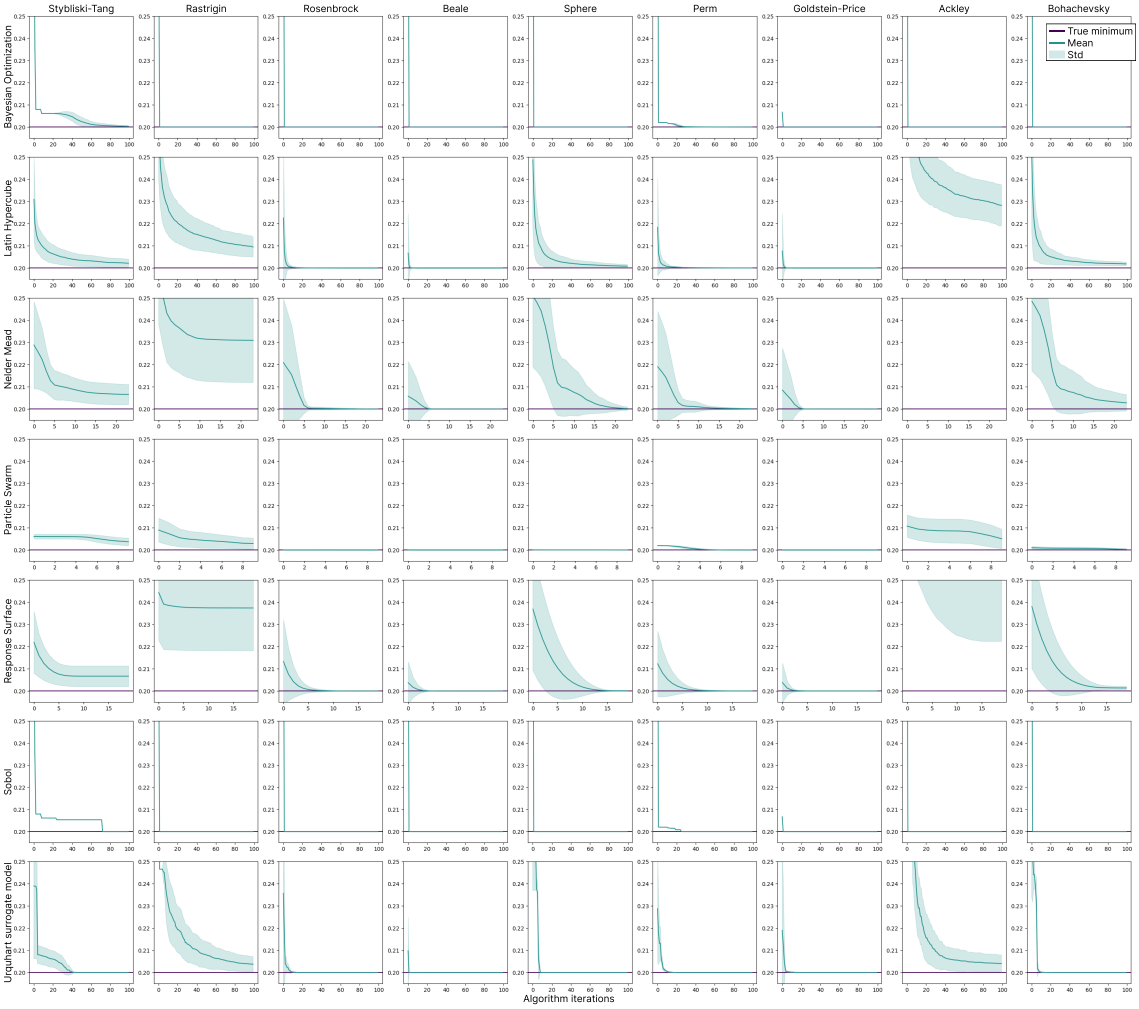

**Figure 3.3:** Evaluation of the optimization algorithms performances: 250 tests have been run over the benchmark functions, in order to compute relevant statistics. On the x-axis, the algorithm iterations are reported while on the y-axis the emulated $C_D$ value.

In Figure 3.3 the performances over the algorithm iterations are displayed. Here, the y-axis represents the optimization cost.

As it is possible to see, the algorithms provide high performances over specific benchmark tests, while performing worse on others.
Some functions, due to their initialization, spotted the true optimum, or very close to it, during their first iterations. This is the reason why some curves are completely flat, overlapping the true known minimum. Moreover, the graph scale has been set the same in all plots, in order to ease the comparison for the reader. Small improvements are thus difficult to appreciate. Figure 3.4 displays a more focused representation of the Latin Hypercube test, to demonstrate the existence of small steps impossible to see from the previous picture. From this figure it is possible to observe its evolution over time, improving with the algorithm iterations, that is not constant but stochastic. Indeed, it it were deterministic, no standard deviation, thus the green area, would be observed.

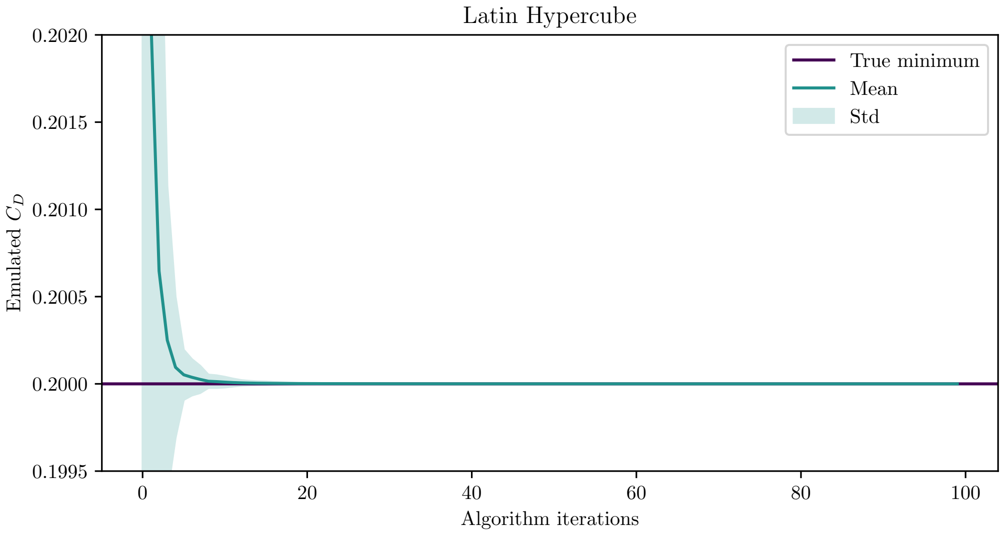

**Figure 3.4:** Evaluation of the Latin Hypercube performances over 250 tests. The test is the same as Figure 3.3, but a narrower output space is displayed to better appreciate small improvements.

Another insightful information is the standard deviation obtained from the tests and highlighted with light blue shadow in Figure 3.3 and 3.5. This allows to expresses the algorithms uncertainty over time. A small standard deviation is a indication for reliability, meaning that even though the processes are initialized with different points, the outcome is robust and repeatable. Algorithms that presented high standard deviations during the benchmark tests will be discarded, as not reliable enough for collecting high quality data for the mechatronics demonstration.
As mention in Section 3.1.1, more attention is payed on the results obtained from the tests over Sphere, Perm, and Bohachevsky benchmark functions, as they present a convex property, more similar to current optimization problems.
A comparison example is reported in Figure 3.5, in which Nelder Mead, Response Surface and Urquhart surrogate model are shown. Nelder Mead and Response Surface algorithms present higher standard deviation over time with respect to the Urquhart surrogate model. Even though they might still perform sufficiently good

during wind tunnel tests, the choice of not using them has been made. This guarantees that reliable data will be gathered.

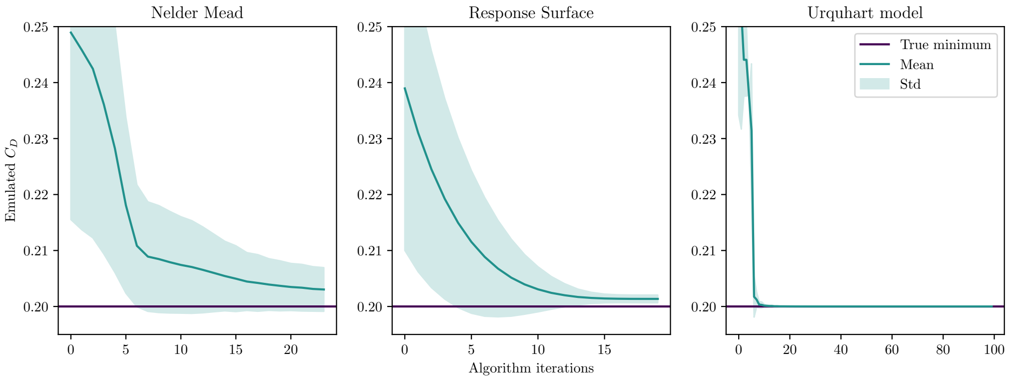

**Figure 3.5:** Focus on the standard deviations obtained during the tests on the Bohachevsky function reported in Figure 3.3. The first two graphs present higher standard deviation, while the Urquhart surrogate model results to be more reliable.

It is also important to underline that the Latin Hypercube Sampling and the Sobol Sampling, as pure optimization algorithms, shown in Figure 3.3, just consist in selecting almost-random points. Since they are structured as such, and no advanced logic nor development is included in these approaches, the optima that can be found only depend on stochasticity. This led to interpret the two methods as trial and error approaches, the exact same way the aerodynamics department is nowadays using to find the best configurations. The two methods have thus been discarded as pure way to investigate the optimum.

After all these consideration, only the Bayesian Optimization, Particle Swarm and Urquhart surrogate model remain to be exploited. Looking at the performances displayed in Figure 3.3, the algorithms are completely equivalent. Even though they have been initially tested in the wind tunnel, the majority of the results is created using the surrogate model, as considered to be more reliable and stable since already tested by Urquhart et al. in PVT [9]. In this way, the certainty of obtaining good results was guaranteed.

### 3.1.3 Averaging time in wind tunnel

Previous works run at PVT showed to have obtained a confidence interval of 0.0008 for $C_D$ value for a confidence of 95% with a 20 $s$ averaging [9].

The facility and the instruments used in this work are the same used in the mentioned paper, while the clay car model differs.

, it is appropriate to assume that the tests for this project will be affected by the same standard deviation. Since two different averaging can be used, 20 $s$ and 60 $s$ respectively, it is fundamental to understand which is the one that best suits the problem.

The definition of confidence interval $C_I$ is reported in Equation 3.2.

$$C_I = \bar{x} \pm z^* \frac{\sigma}{\sqrt{n}} \tag{3.2}$$

with $\bar{x}$ representing the sample mean value, $z^*$ the level of confidence, also known as *z-score*, $\sigma$ the sample standard deviation and $n$ the size of the considered number of samples. From statistics, it is known that a confidence level of 95% is associated to $z^* = 1.96$

$$C_I = \bar{x} \pm 1.96 \frac{\sigma}{\sqrt{n}}$$

To compute the averaged values, the wind tunnel systems updates data at a frequency of $1\,Hz$, meaning that for a $20\,s$ averaging the population size becomes $n = 20$. Assuming that the sampled data will be affected by the same standard deviation, a $60s$ averaging will lead to a confidence level with a population size three times bigger. In [9] the confidence interval was formulated as

$$C_{I_{20}} = \bar{x} \pm 1.96 \frac{\sigma}{\sqrt{20}} = \bar{x} \pm 0.0008$$

Nevertheless, it is safer to round up the value to $C_{I_{20}} = 0.001$ to slightly extend the confidence interval and work with a more relaxed assumption.

$$C_{I_{20}} = \bar{x} \pm 1.96 \frac{\sigma}{\sqrt{20}} = \bar{x} \pm 0.0008 \simeq \bar{x} \pm 0.001$$

Therefore, for a $60\,s$ averaging

$$C_{I_{60}} = \bar{x} \pm 1.96 \frac{\sigma}{\sqrt{60}} = \bar{x} \pm \frac{0.001}{\sqrt{3}} = \bar{x} \pm 0.00058 \simeq \bar{x} \pm 0.0006$$

since the wind tunnel system has a sensitivity of $C_D = 0.0001$. Table 3.2 summarizes what has been said so far.

| **Averaging time** | $20\,s$ | $60\,s$ |
|---|---|---|
| **Confidence interval** | $\bar{x} \pm 0.001$ | $\bar{x} \pm 0.0006$ |

**Table 3.2:** Estimated confidence interval coming from different averaging times.

As it is possible to see, higher averaging times lead to better results since the confidence interval is narrower. This turns into more accurate wind tunnel data and an increased stability of the optimization algorithms. However, introducing an average time of $60\,s$ leads to an 80% increase of the overall waiting time and the benefits coming from higher data quality might not be worth it. It is then fundamental to understand how uncertainty might affect the general behavior of the algorithms.

To test it out, the uncertainty due to the confidence interval was simulated. Gaussian distributed noise with zero mean and $\sigma = C_I$ was added to the output of the benchmark functions during the optimization runs. A similar behaviour was observed in all the optimization algorithms. Figure 3.6 shows only the Nelder Mead case since easier to observe and understand.

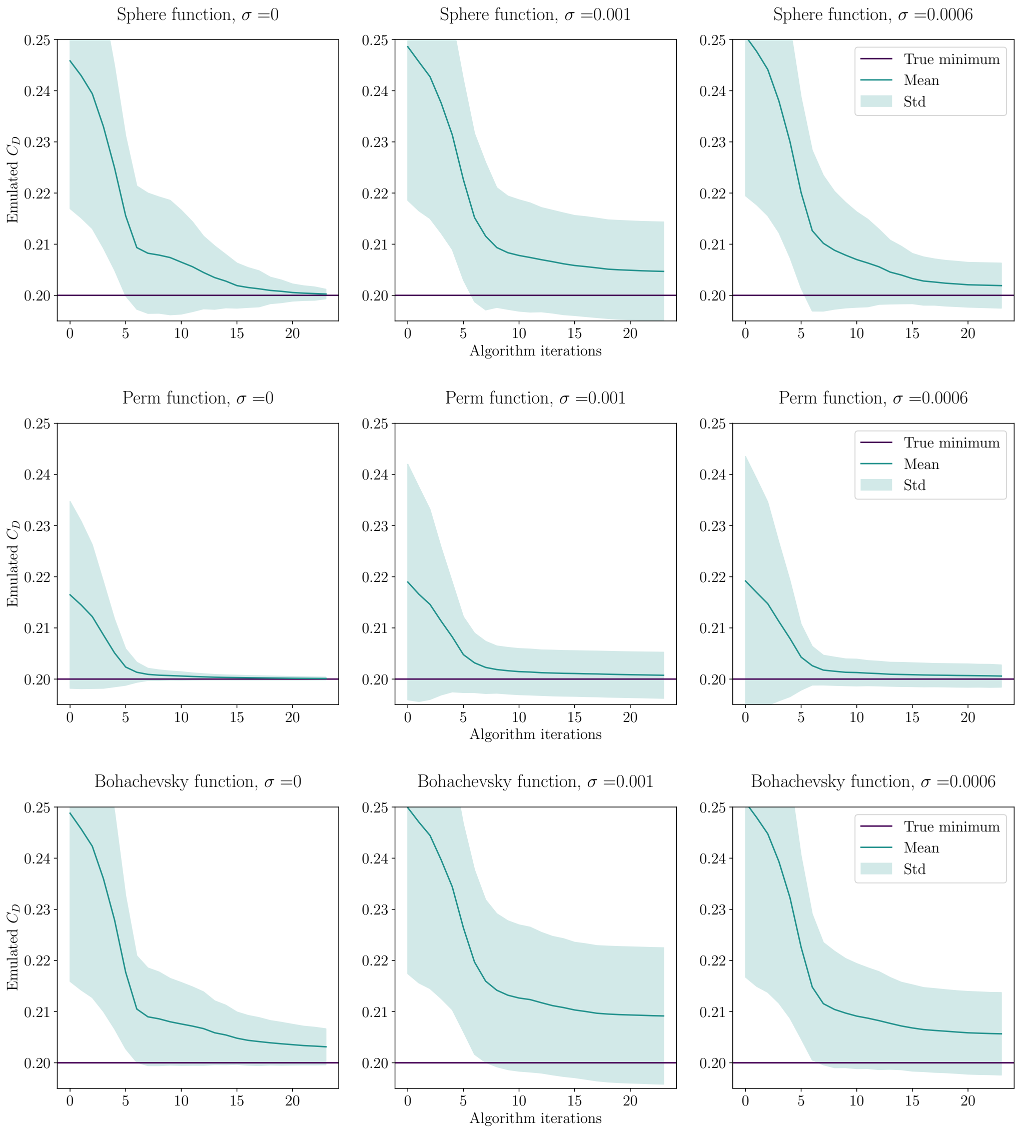

**Figure 3.6:** Effect of different confidence interval on optimization algorithms. The Nelder Mead case is illustrated, as easier to observe the true impact the uncertainty induces.

Figure 3.6 shows the impact of uncertainty due to variable confidence intervals summarized in Table 3.2. Sphere, Perm and Bohachevsky functions were taken into account, as they better represent the clay car optimization quest as stated in Section 3.1.1.
Table 3.3 reports the averaged error over 250 tests from the true minimum for each of the considered benchmark functions. As it is possible to see, the artificial noise introduced to simulate the variability of data substantially affects the performances. Specifically, the errors increase about one order in the Sphere and Perm test, and almost two orders of magnitude in the Bohachevsky one.
Nevertheless, even though uncertainty heavily affects the optimization results, the difference between the tests conducted with $\sigma = 0.001$ and $\sigma = 0.0006$ is very small. Considering the longer times needed to obtain confidence interval, a $60\,s$ average

does not add particular improvements in terms of better trade-off between time and quality.

| **Function** | $\sigma$ | **Error** |
|---|---|---|
| Sphere | 0 | 0.0003 |
| Sphere | 0.001 | 0.004 |
| Sphere | 0.0006 | 0.001 |
| Perm | 0 | 0.00009 |
| Perm | 0.001 | 0.0009 |
| Perm | 0.0006 | 0.0006 |
| Bohachevsky | 0 | 0.0003 |
| Bohachevsky | 0.001 | 0.008 |
| Bohachevsky | 0.0006 | 0.006 |

**Table 3.3:** Errors in the minimization processes due to Gaussian distributed noise with zero mean and variable standard deviation values. The scores points out how different confidence intervals affect the quality of the optimization processes.

Initial tests in the wind tunnel were conducted by using a $20\,s$ moving average to fasten the optimization process. Although data was acquired at high pace, instability in $C_D$, $C_{LR}$ and $C_{LF}$ values were encountered. This was most probably due to the test rig built: since the flaps are relatively small and they do not cover the entire car floor, high variability affected the coefficient values due to a fluctuating wake.
Consequently, all the tests were retaken with the longer $60\,s$ averaging time, leading to better and more stable results. In the following sections, only performances obtained from these last tests will be illustrated, as more precise and accurate. Nevertheless, in the Appendix a list of all the tests done in the wind tunnel can be found.

### 3.1.4 Number of samples

When dealing with computational expensive functions and their optimization, it is important to find a good trade off between the improvement in the result and the time spent for seeking it. Indeed, it is well known from the literature that most of optimization algorithms will find the true global optimum for a running time that approaches infinite. Nevertheless, hours of computation might not be worth for improvements in the order of $10^{-9}$, especially if the final outcome has to be brought in real world scenarios, where high sensitivities cannot be achieved.
In the mechatronics context, the expensiveness of optimizing the unknown function associated to the clay car model does not rely on computational times but on the costs for using the wind tunnel, in terms of power usage, booked shifts and required staff.
The more the wind tunnel is used, the more power it will require. PVT presents a turbine that consumes $5\,MW$ if run at its maximum speed, generating wind at 250 $km/h$. For tests at $140\,km/h$, the fan requires only $0.9\,MW$ but additional agents, namely a $3\,MW$ cooling system and a $1.8\,MW$ scoop fan, will still be involved. With the current price of electricity, it is easy to estimate the cost for using the

wind tunnel system and as a consequence, the more it is used the more money will be needed.

Additionally, if PVT is used for assessing the aerodynamics optimization of a clay car model, other investigations such as final tests or certification procedures for other vehicles cannot be run, creating a bottleneck in the company workflow and delaying a series of scheduled tests that might be fundamental for other departments.

Therefore, it is important to understand whether the considered optimization algorithms provide good results and at what point the increased number of samples do not add significant value to the minimization quest. Figure 3.7 shows the analysis done to assess the best trade-off between the number of considered samples and the achieved optimal configurations.

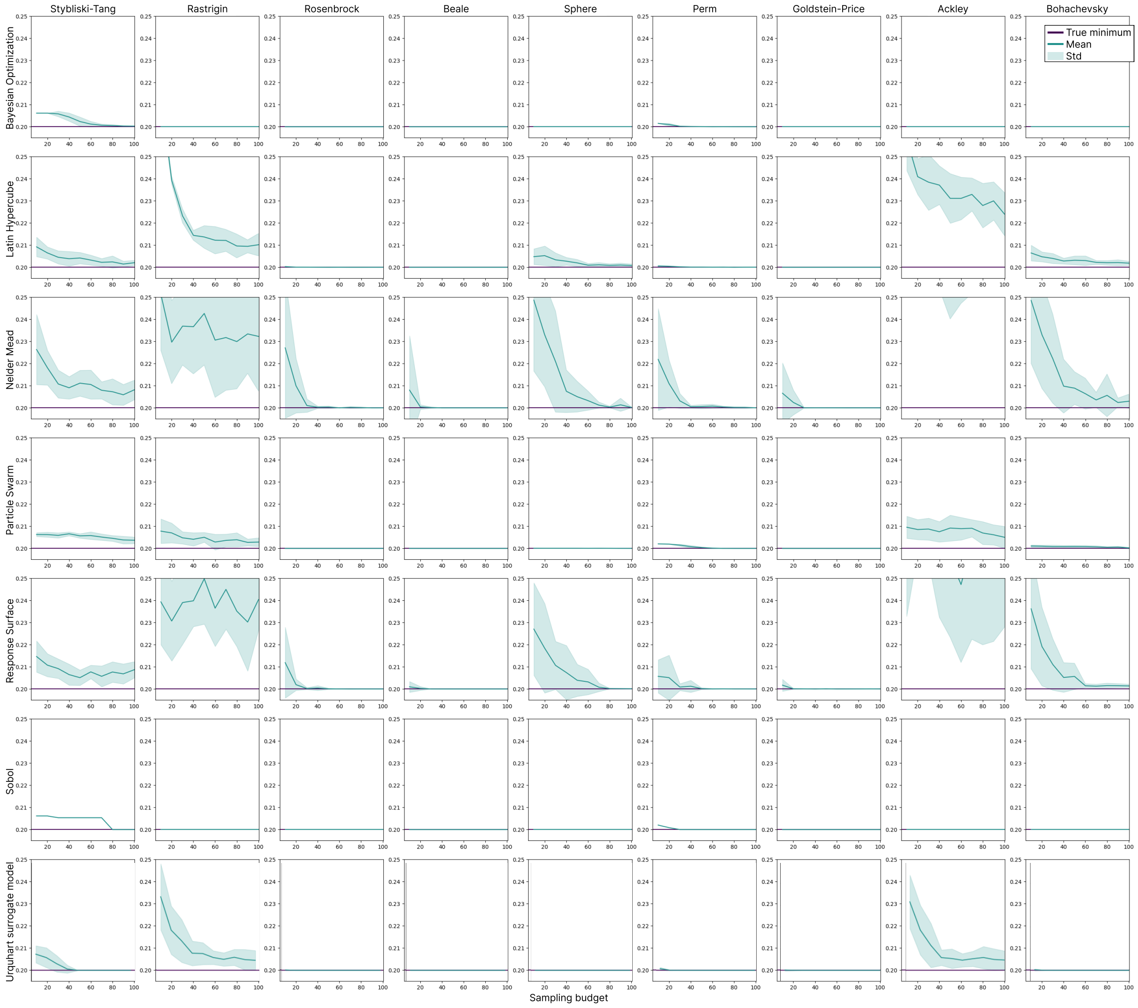

**Figure 3.7:** Maximum allowed sampling budgets versus optimization algorithms performances. The algorithms were tested 20 times for each budget, leading to the computation of mean and standard deviation.

Each optimization algorithm was tested on all the benchmark functions with a variable sampling budget. In particular, the algorithms were provided with an increasing budget in the range $[10, 100]$.

For every sample set, 20 different tests were run to be able to estimate the mean behaviour and the associated standard deviation. Only the best outcome from the algorithms were taken into account instead of the evolution over time of the best found value.
From Figure 3.7 it is possible to observe that most of the plots are flat. This is due to the detected minimum: a flat curve means that the algorithms were consistent and able to find the same value even with a small sampling budget.
Nevertheless, from the graphs that change over time, it is possible to see that improvement is connected to the increasing number of samples provided. Specifically, several algorithms over the benchmark functions started to present a really good performance while approaching a budget of 60 samples. After that, improvements still occurred but the improvement rate dramatically lowered, settling to constant for most of the tests.
For these reasons, a total budget of 60 samples has been adopted for the wind tunnel tests, as believed to provide the best trade-off between iterations and performance quality.

### 3.1.5 The initialization effect

Diving into the algorithms details, one fundamental aspect that strongly affects their behaviour is the way they are initialized. Generally speaking, most of the optimization approaches start with a randomized sample or set of samples, in order to increase sparsity and avoid getting stuck in local minima.
However, there exists different methods to better initialize an optimization algorithm. In some cases, for example, it is aimed to cover as much search space as possible, trying to avoid clusters of points. Other initializations others try to sample from probability distributions. For this project, three different initialization approaches have been considered: *Uniform sampling* (Gaussian distributed), *Latin Hypercube Sampling* and *Sobol sampling.* The difference among them can be observed in Figure 3.8, where a 2-dimensional example is shown. Specifically, $X_1$ and $X_2$ are the two dimensions in which the methods sampled the points. By displaying each dimension on an axis, it is possible to see how the sampling points are located in space.

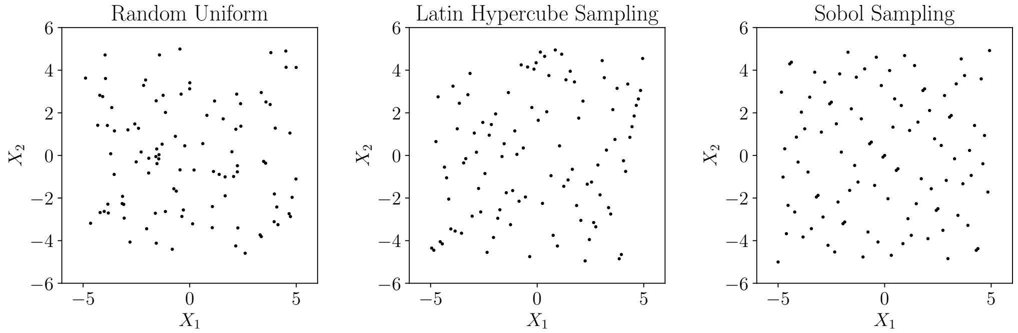

**Figure 3.8:** Different sampling methods considered for the mechatronics implementation. 100 points have been sampled from a 2-dimensional space. Each dimension is bounded in the range $x_i \in [-5, +5]$.

Sobol and Latin Hypercube sampling divide the space in sub-regions from which only one value is sampled. However, in Latin Hypercube method no constraints about minimum relative distances are introduced, leading to possible data clustering.
A more remarkable behavior of this effect can be observed in the random uniform sampling. Since the method does not divide the input space in sub-regions, bigger clusters of data can occur.
On the other hand, Sobol sampling tries to maximize the relative distances among the points in order to cover as much space as possible, leading to a more well-distributed selection.
An even more strong visualization of this effect can be observed by highlighting the points neighbourhoods and their superimposition, as shown in Figure 3.9.

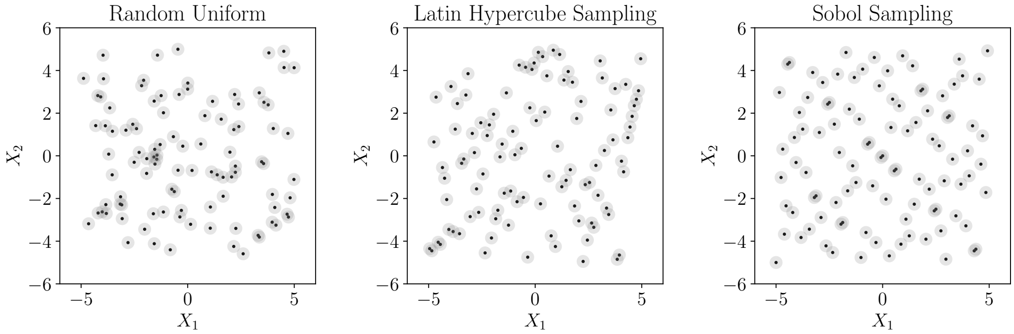

**Figure 3.9:** Different sampling methods considered for the mechatronics implementation. The points have been sampled from a 2-dimensional space. Neighbourhood was also reported to better visualize possible superimposition.

However, in the examples shown in Figure 3.9 an infinite sensitivity was considered. As mentioned in Section 2.2, the test rig presents a sensitivity of 0.5°, strongly different from the one considered for the sampling test. Consequently, it is important to highlight the behaviour of the sampling methods when dealing with a discrete space. Figure 3.10 shows that.

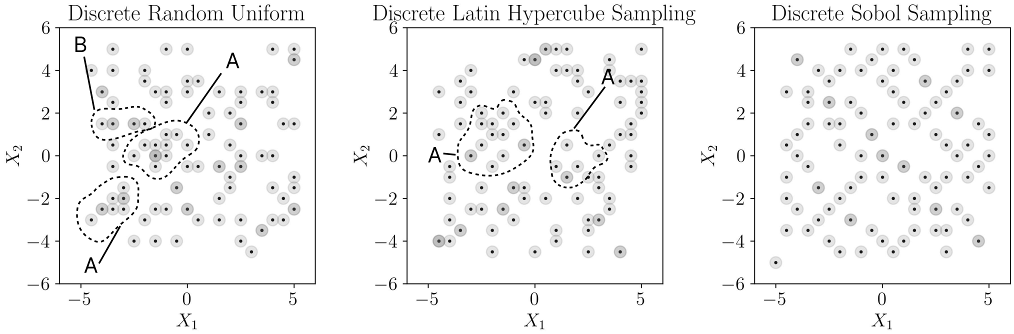

**Figure 3.10:** Different sampling methods considered for the mechatronics implementation. The points have been sampled from a 2-dimensional space and the neighbourhood was highlighted to better identify the superimposition. A) strong superimposition effect and B) strong clustering effect.

As it is possible to observe, uniform sampling is characterized by a strong clustering effect. Several points are superimposed or very close to each other, leading to several strong vacancies of unexplored search space. Latin Hypercube Sampling, on the other hand, is affected by a smaller number of overlays, but the clustering effect can still be observed. Indeed, in Figure 3.10 the Discrete Latin Hypercube Sampling shows several darker points, symptom of superimposition. This issue cannot be neglected, as points within the gaps might be fundamental for leading the optimization algorithm to the right search direction. Indeed, when dealing with expensive functions, either computationally or economically, it is important not to waste initialization samples on already considered points, in order to maximize the algorithm capabilities. In solutions that exploit surrogate models, sampling the same point multiple times means limiting the abstraction capability of the model to approximate the unknown function. This can lead to dramatically lower performances, as features such as convexity could be missed.

Sobol sampling, instead, performs better than the others since it is able to almost cover the entire input space with a low overlapping effect. This immediately leads to a more complete initialization of the optimization algorithms, allowing higher performances during the tests.

The true impact the sampling methods have on the optimization methods can be observed in Figure 3.11. For the test, the Particle Swarm Optimization algorithm was taken into account.

At first glance, it is observed that Sobol sampling leads the optimization algorithm to better performances, as it allows a more even and higher coverage of the search space. Indeed, by considering a broader search space, particles are generally more spread, leading to a better initialization (e.g. the Bohachevsky test) and a faster convergence (e.g. Rastrigin test). Moreover, from the considered graph, the standard deviation that affects the average performance is reduced. This directly leads to a more reliable, higher repeatable optimization procedure.

Regarding the surrogate model developed by Urquhart et al. in [12], the authors relied on the Latin Hypercube sampling method to initialize the algorithm. Nevertheless, they also noticed how the clustering problem affects the model performances. Consequently, they developed an optimize version, called in the paper *Optimized Latin Hypercube* sampling, which exploits the Audze-Eglais objective function to evenly spread the sampling points in the input space. The difference between a standard (random) Latin Hypercube sampling and its optimized version can be observed in Figure 3.12, directly taken from the original paper [12].

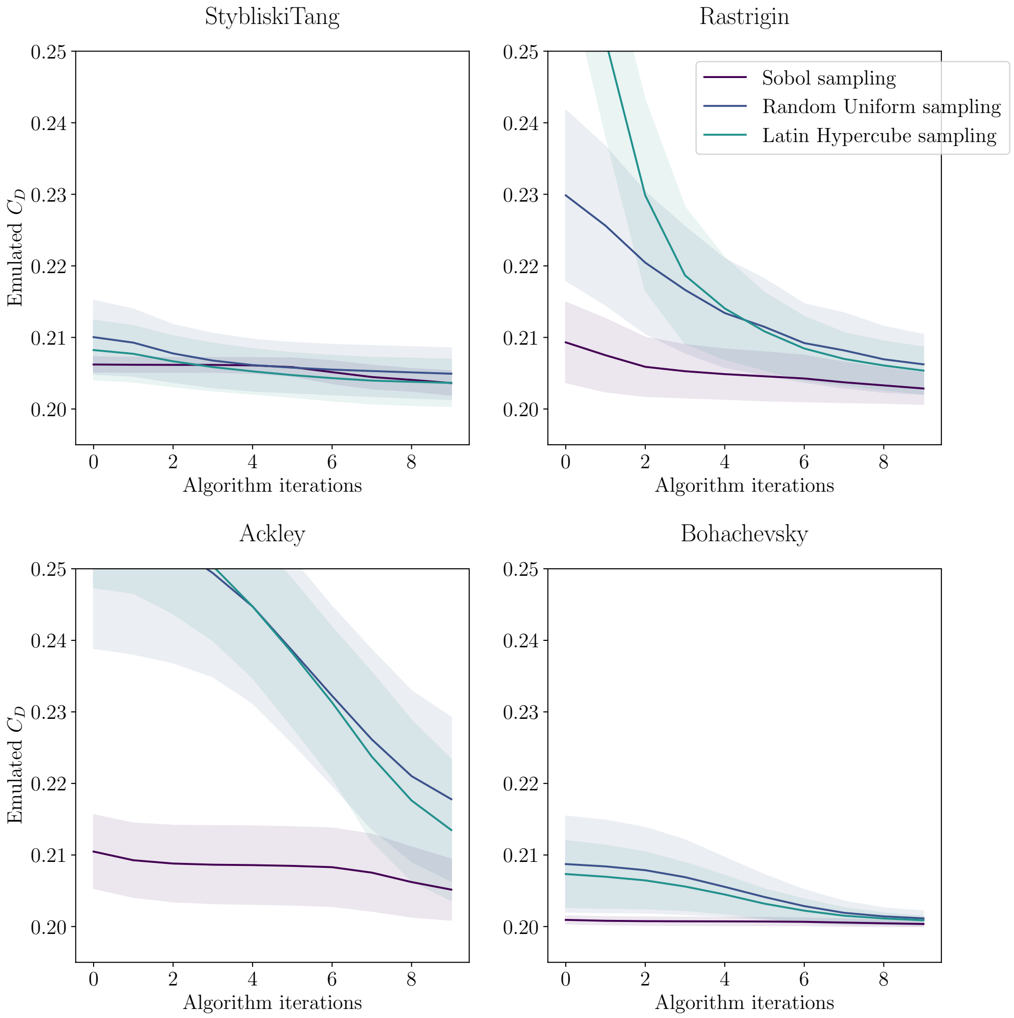

**Figure 3.11:** Impact of the initialization effect on the Particle Swarm Optimization algorithm, tested 250 times. Mean and standard deviation are displayed for each method.

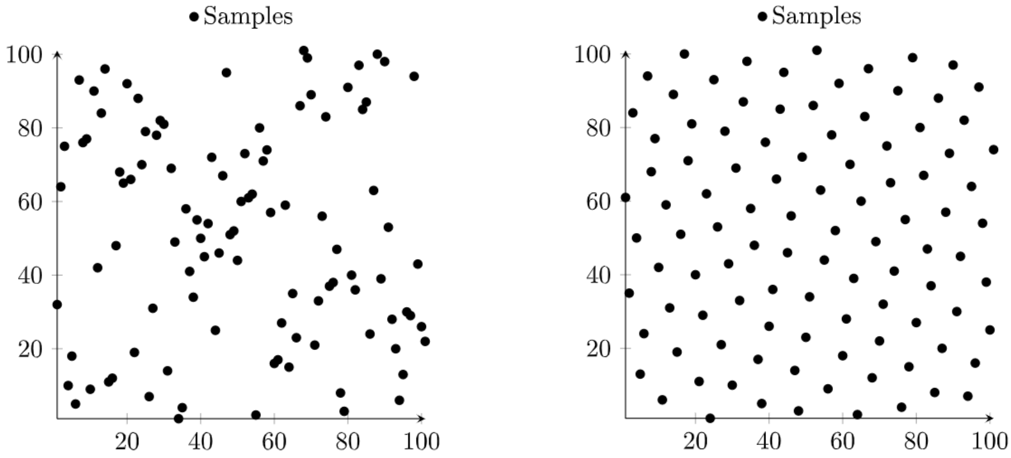

**Figure 3.12:** Standard (random) Latin Hypercube sampling (left) with respect to Optimized Latin Hypercube sampling (right). The clustering problem is solved in the optimized version.

It is possible to see from the picture that the Optimized Latin Hypercube sampling behaves in a similar manner to Sobol sampling. Hence, for the optimization quest, the Urquhart surrogate model is assumed to be correctly initialized.

### 3.1.6 Repeatability

A fundamental feature that describes the quality of the mechatronic system and its implementation is the so called repeatability. Repeatability (or test–retest reliability) describes the variation in successive measurements of the same variable taken under the same conditions (e.g., same observer, location, instrument, and procedure) in a short period of time.

A high-repeatability system leads to high performances and reliability, meaning that identical inputs lead to almost the same output. The system is therefore affected by low uncertainty, it is trustable and robust.

In this case, the repeatability test consisted in sampling $C_D$ values several times from the wind tunnel, for different flap configurations. The configurations were tested in different orders during the tests, to provide higher data reliability. Data has been collected at 0°-yaw and with a wind speed of $140\,km/h$, considering an averaging time of $60\,s$, as the one used for the optimization processes. The obtained values are reported in Table 3.4.

| | **Config. 1** | **Config. 2** | **Config. 3** | **Config. 4** |
|---|---|---|---|---|
| Test 1 | 0.3316 | 0.3238 | 0.3286 | 0.3272 |
| Test 2 | 0.3320 | 0.3236 | 0.3282 | 0.3273 |
| Test 3 | 0.3318 | 0.3233 | 0.3284 | 0.3271 |
| Test 4 | 0.3314 | 0.3234 | 0.3281 | 0.3275 |
| Test 5 | 0.3314 | 0.3240 | 0.3279 | 0.3273 |
| Test 6 | 0.3312 | 0.3233 | 0.3286 | 0.3273 |
| Test 7 | 0.3316 | 0.3239 | 0.3282 | 0.3273 |
| Test 8 | 0.3318 | 0.3234 | 0.3281 | 0.3272 |
| Test 9 | 0.3315 | 0.3236 | 0.3284 | 0.3269 |
| Test 10 | 0.3318 | 0.3240 | 0.3285 | 0.3272 |
| Mean | 0.3316 | 0.3236 | 0.3283 | 0.3272 |
| Std | 0.0002 | 0.0003 | 0.0002 | 0.0001 |

**Table 3.4:** Repeatability tests and the obtained $C_D$ values. Data has been collected at 0°-yaw with a wind speed of $140\,km/h$, considering an averaging time of $60\,s$. Mean value and standard deviation for each test are listed.

For each point, 10 samples have been collected, leading to a total of 40 tests. Along with the obtained $C_D$ values, means and standard deviations are also reported. The most insightful information from the table is on the standard deviation, which points out the level of uncertainty associated to the tests. The smaller the standard deviation, the more precise and reliable the system is. In this case, all the tested points led to consistent results, characterized by a low uncertainty.

A visualization of the standard deviation that affects each configuration can be found in Figure 3.13. A maximum value of $C_D = 0.0003$ was observed. Since it is well below the uncertainty of the balance ($C_D = 0.001$), the tests must be considered successful, as no higher precision could be added to the system.

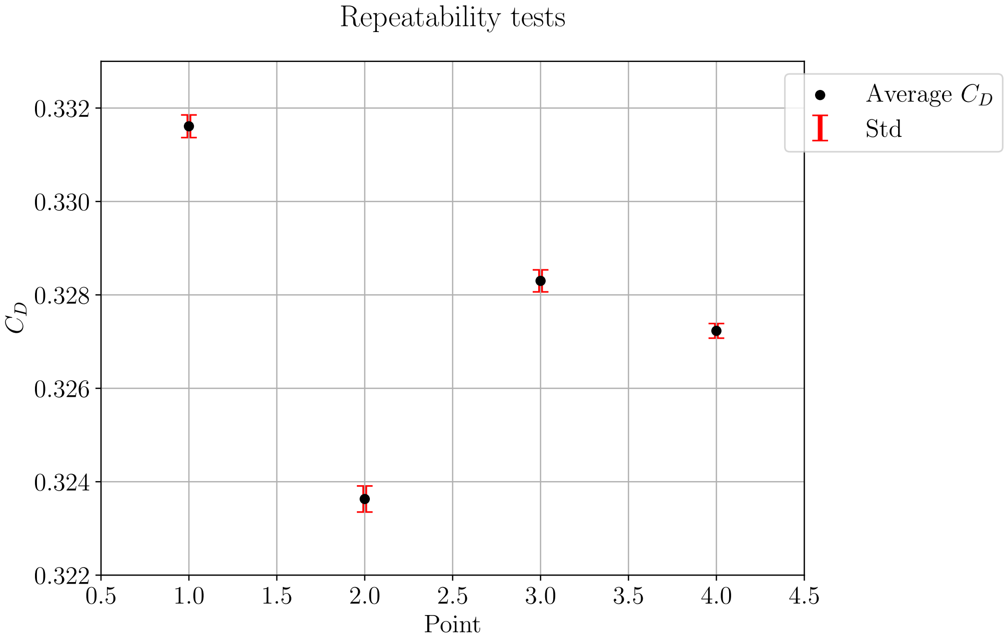

**Figure 3.13:** Visualization of the $C_D$ values obtained during the repeatability test, conducted at $140\,km/h$ and by using a $60\,s$ averaging time. The error bars, colored in red in the graph, show the standard deviation associated to the tested point.

$C_D$ provides a very insightful information about a car and its efficiency. However, a vehicle must be studied in terms of stability as well. Stability is directly connected to lift forces that act on the model, especially when the car is moving at high speed, e.g. $140\,km/h$. Therefore, it is also important to check the reliability of lift coefficients values $C_{LR}$ and $C_{LF}$.

Since the test rig is mounted on the rear part of the vehicle, no significant deltas have been observed regarding $C_{LF}$. On the other hand, $C_{LR}$ is heavily influenced by the diffuser configuration and thus eligible for a repeatability analysis. In particular, the data shown in Table 3.5 have been acquired during the same repeatability tests and Figure 3.14 shows its graphical illustration.

Considering the definition of confidence interval introduced with Equation 3.2 in Section 3.1.3, the value associated to a 95% confidence level can be computed for the repeatability tests.

$$C_{I_{test}} = \bar{x} \pm 1.96 \frac{\sigma}{\sqrt{10}}$$

In this case, the population number becomes $n = 10$ since points were sampled 10 different times. The formula such computed leads to the results reported in Table 3.6.

| | **Config. 1** | **Config. 2** | **Config. 3** | **Config. 4** |
|---|---|---|---|---|
| Test 1 | 0.0065 | 0.0221 | 0.0083 | 0.0424 |
| Test 2 | 0.0063 | 0.0225 | 0.0087 | 0.0422 |
| Test 3 | 0.0062 | 0.0228 | 0.0095 | 0.0415 |
| Test 4 | 0.0068 | 0.0228 | 0.0091 | 0.0414 |
| Test 5 | 0.0058 | 0.0221 | 0.0094 | 0.0409 |
| Test 6 | 0.0062 | 0.0228 | 0.0080 | 0.0413 |
| Test 7 | 0.0057 | 0.0218 | 0.0083 | 0.0416 |
| Test 8 | 0.0061 | 0.0228 | 0.0088 | 0.0419 |
| Test 9 | 0.0062 | 0.0222 | 0.0091 | 0.0421 |
| Test 10 | 0.0066 | 0.0229 | 0.0092 | 0.0420 |
| Mean | 0.0062 | 0.0225 | 0.0088 | 0.0417 |
| Std | 0.0003 | 0.0004 | 0.0005 | 0.0004 |

**Table 3.5:** Repeatability tests and the obtained $C_{LR}$ values. Data has been collected at 0°-yaw with a wind speed of $140\,km/h$, considering an averaging time of $60\,s$. Mean value and standard deviation for each test are listed.

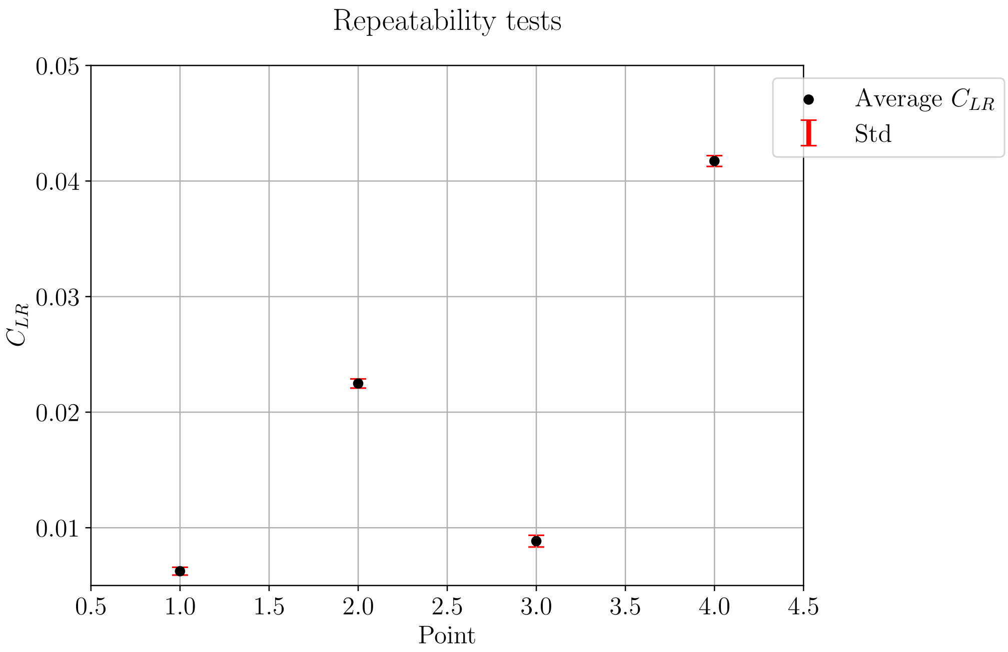

**Figure 3.14:** Visualization of the $C_{LR}$ values obtained during the repeatability test.

| Confidence Interval | **Point 1** | **Point 2** | **Point 3** | **Point 4** |
|---|---|---|---|---|
| $C_{I_{C_D}}$ | 0.0001 | 0.0002 | 0.0001 | 0.0001 |
| $C_{I_{C_{LR}}}$ value | 0.0002 | 0.0002 | 0.0003 | 0.0003 |

**Table 3.6:** Confidence intervals associated to the repeatability tests

Considering $C_{I_{C_D}}$, it is interesting to point out that the assumption introduced in

Section 3.1.3, namely to have the same standard deviation encountered in [9], is confirmed. Moreover, since a wider moving average was taken into account, the confidence interval is even smaller, directly leading to better performances of the optimization and a higher reliability of the data.

## 3.2 Data discussion

After carefully setting up the system and once identified the best optimization algorithms to rely on during the tests, data has been acquired for two different car configurations at different yaw values. In the following sections the test results will be presented, illustrating the potential of the mechatronic system as a new method to study and improve the aerodynamics of clay car models.

As mentioned in Sections 3.1.3 and 3.1.6, a $20\,s$ moving average was initially considered. The first tests were conducted along with the repeatability evaluations, which outcomes were analyzed only during the post-processing phase. Once discovered the unreliability of the results, all the tests had to be redone, in order to provide higher quality analyses. Therefore, in the following sections all the inaccurate values are not reported, except for Section 3.2.1 in which a further analysis about reliability and performances is discussed.

### 3.2.1 Validation of the averaging time assumption

As already mentioned in different sections, averaging times heavily affects the quality of the results. Through benchmark and repeatability tests, it has been demonstrated that measurements might lead to different outcomes due to non-stable wakes and flow unsteadiness.

The data unsteadiness directly affects the optimization algorithm performances, as inaccurate values of $C_D$ or $C_{LR}$ might be bounded to the wrong flaps configurations. In this way, the algorithms will avoid to further investigate certain areas of the search space, misleading the operator.

An example of this is shown in Figure 3.15, in which a $C_D$ optimization has been conducted at 0° yaw with wind speed of $140\,km/h$. In particular, a 4-dimensional optimization has been performed, exploiting the Urquhart surrogate model.

Looking at the picture, it is clear that an higher averaging time leads to better performances. It is more correct to start comparing the two results from the $20^{th}$ point, as the first steps might be different due to an unlucky initialization of the algorithm. Not only the $60\,s$ moving average scored a better optimization, but while approaching the final steps a further improvement has been done. Eventually, a configuration with $\Delta C_D = 0.0021$ lower was found. The value has to be considered quite remarkable, as for the aerodynamics optimization of passenger cars improvements above $C_D = 0.001$ matter.

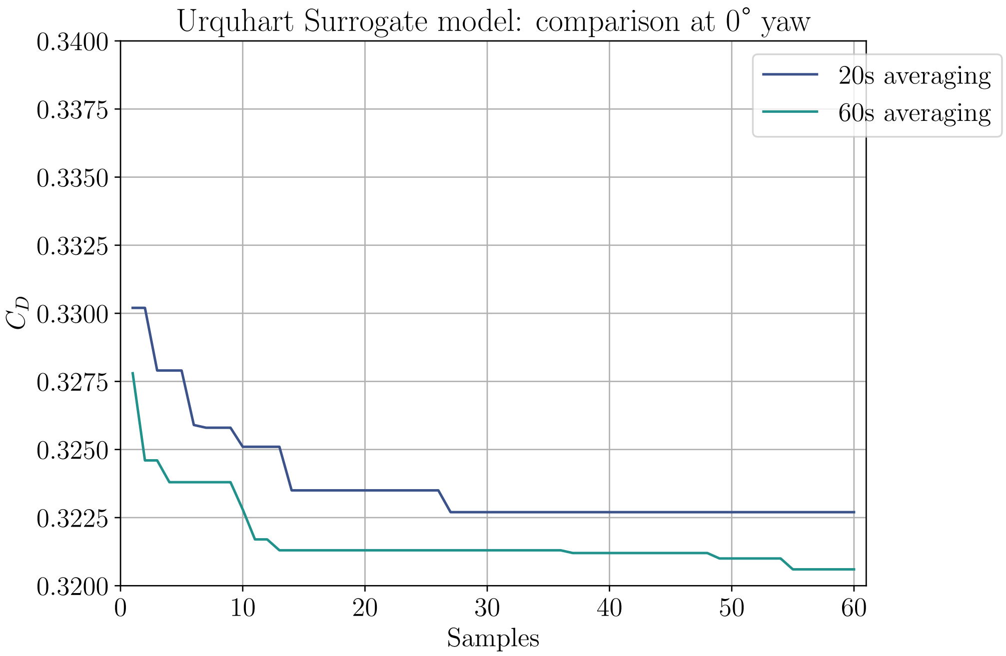

**Figure 3.15:** Performance comparison between the 20 $s$ and the 60 $s$ averaging during a 4-dimensional optimization at 0° yaw. The clay car $C_D$ value is displayed.

A more remarkable difference that can be obtained by using a 60 $s$ average can be seen in Figure 3.16 and Figure 3.17, in which a final difference of $C_D = 0.0037$ and $C_D = 0.0025$, respectively, is observed.

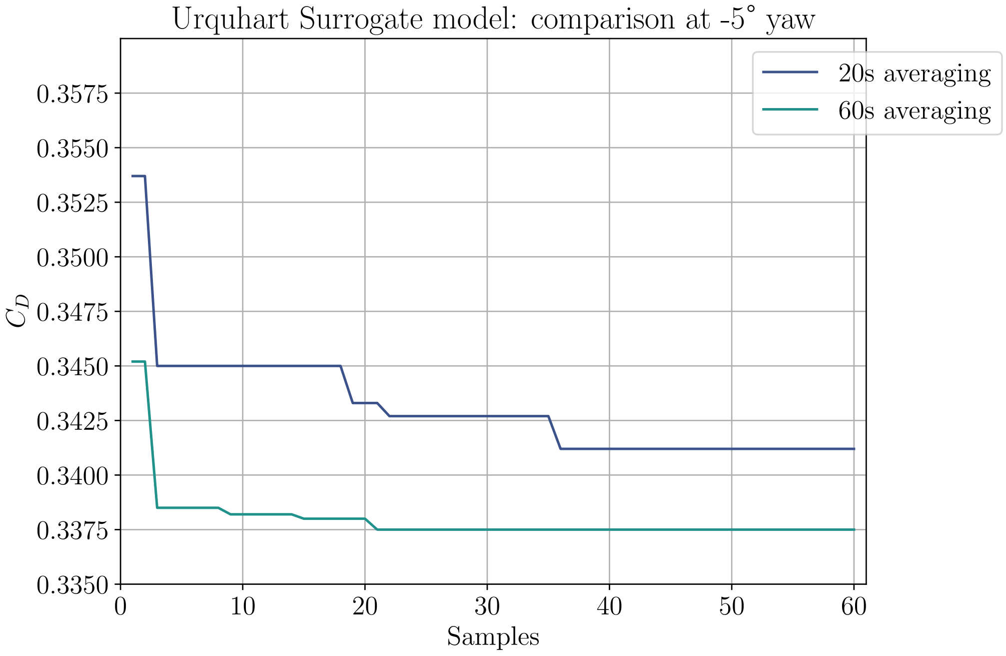

**Figure 3.16:** Performance comparison between the 20 $s$ and the 60 $s$ averaging during a 4-dimensional optimization at $-5°$ yaw. The clay car $C_D$ value is displayed.

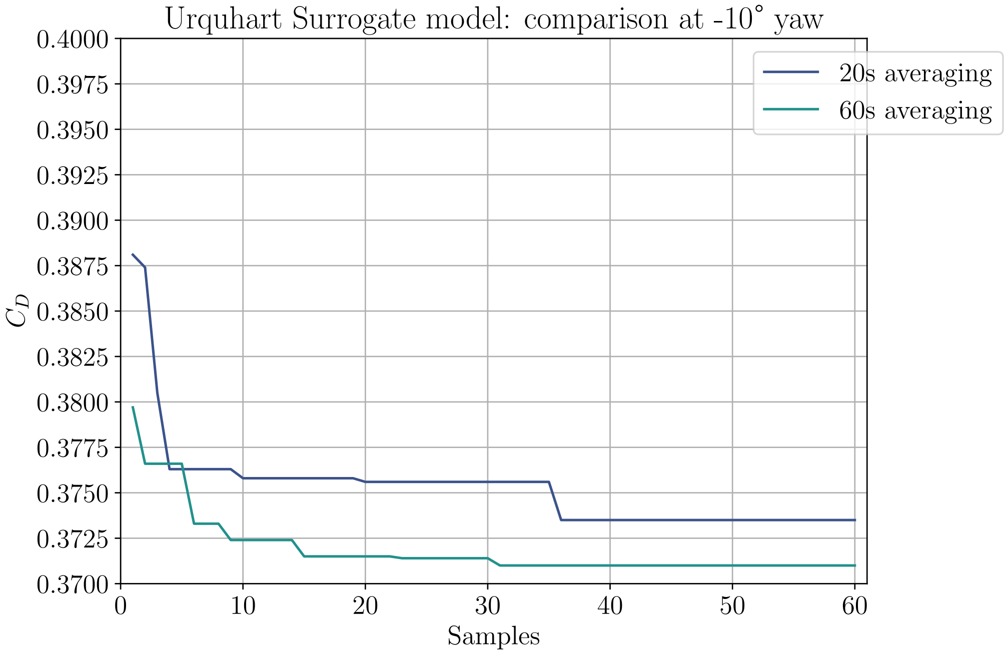

**Figure 3.17:** Performance comparison between the 20 $s$ and the 60 $s$ averaging during a 4-dimensional optimization at $-10°$ yaw. The clay car $C_D$ value is displayed.

It is clear then that an higher averaging time, as supposed, make the optimization algorithms more stiff and solid in their optimization processes. Noticeable differences can be observed by implementing one moving average or another, leading to better or worse results. This confirms the assumption that 60 $s$ averaging time guarantees high quality data, and that waiting more for computing the aerodynamics values brings optimality.

### 3.2.2 Optimization at 0° yaw

A detailed explanation of the workflow that aerodynamics engineers at Volvo Cars currently follow is reported in Section 1.2 and 3.3. Regarding the diffuser optimization, the latest test routine consist in starting from an already known good position, discovered via CFD analysis, and performing a sweep of at least three new configurations, verifying the neighbourhood diffuser angles.

The process, as already discussed, can be roughly seen as a 1-dimensional minimization attempt via a trial and error approach. This because engineers just sample the local area around the known point with a 1D moving diffuser, hoping to find better configurations. Even if effective, the trial and error approach is not efficient and improved configurations are not guaranteed.

In order to demonstrate that the mechatronic project can perform better than this method, a 1-dimensional analysis has been conducted. Particularly, a sweep movement covering all the search space has been run, considering a step of $\Delta\theta = 1°$. The test results are shown in Figure 3.18. From the picture it is clearly visible that a unique minimum can be identified during the diffuser motion, scoring a $C_{D_{min}} = 0.321$. Specifically, the best configuration corresponds to $\theta = 5°$ according to the convention introduced in Section 2.5.2.

Additionally, the trend shown in Figure 3.18 confirms the assumption of the problem associated to the diffuser optimization to be convex. Indeed, only one minimum can be spotted, while its neighbourhood grows rapidly.

Just with this simple test, it is possible to find an initial optimum by covering almost the entire search space in a finite amount of time. With the settings adopted for the system, namely 60 $s$ of averaging time, 30 $s$ for the wake stabilization and 5 $s$ for moving from one diffuser position to another, the whole investigation and therefore the minimum can be found in roughly 35 minutes.

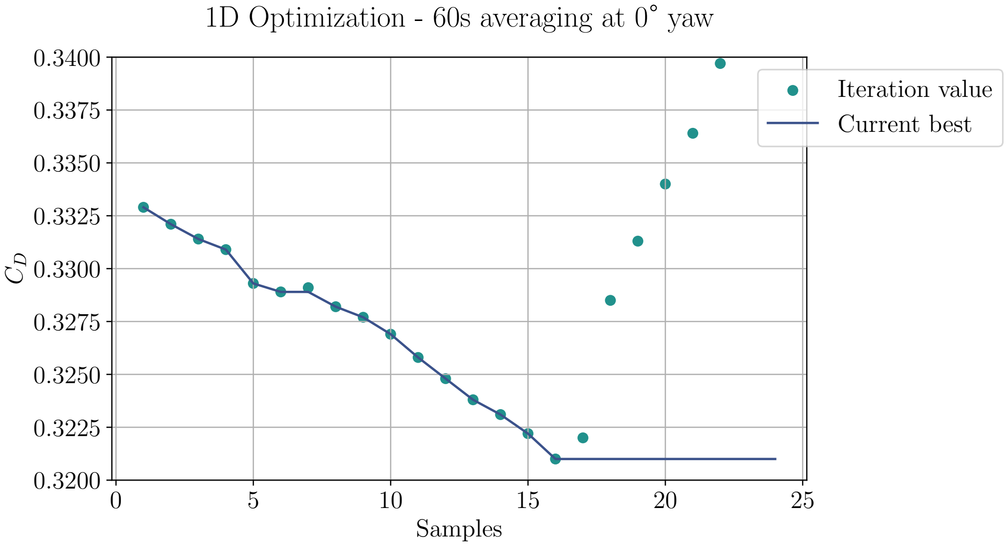

**Figure 3.18:** 1-dimensional mechatronics test to optimize the clay car drag coefficient $C_D$ at 0° yaw and wind speed of 140 $km/h$.

The goal of the mechatronic project is to find even better solution than the standard ones. By relying on optimization algorithms and working in higher dimensional search spaces, more performing results can be found. This might lead to non-trivial configurations that optimize possible asymmetries or unknown dynamics of the vehicle, not taken into account until now.

In this case, a 4-dimensional optimization has been run, during which each flap was individually controlled and treated as one variable of the input space. The obtained $C_D$ values and the optimized result are represented in Figure 3.19

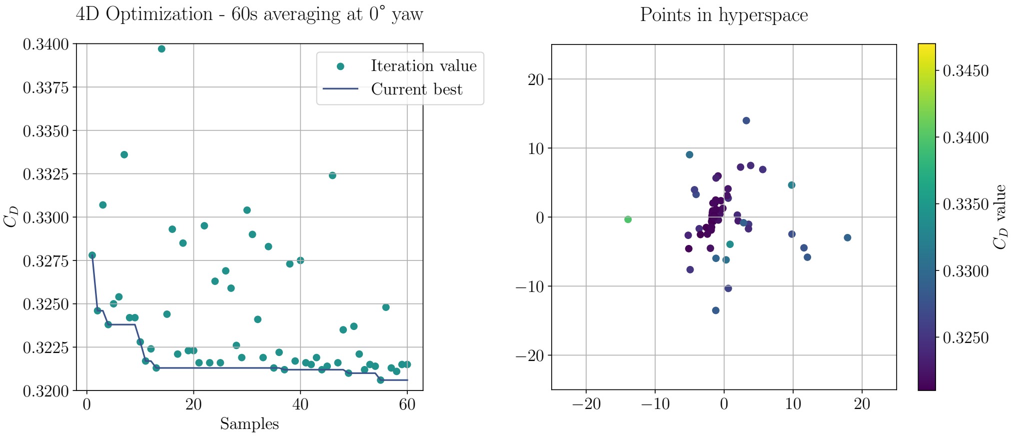

**Figure 3.19:** 4-dimensional mechatronics test to optimize the clay car drag coefficient $C_D$ at 0° yaw and wind speed of 140 $km/h$, by using the Urquhart surrogate model. On the left side, $C_D$ values obtained from the sampling process are shown along with the evolution of the best value found over time. On the right side, a 2-dimensional hyperspace is shown, to better represent the disposition of the points and their relative distance.

In particular, the Urquhart surrogate model was used for assessing the investigation and a minimum of $C_{D_{min}} = 0.3206$ was found. As expected, the algorithm tried to sample more points in the neighbourhood of what it considered the true minimum, leading to a precise and clustered sampling. In Figure 3.19 two graphs can be observed. In the one on the left side, the scattered $C_D$ values obtained in the optimization process are reported, as well as the evolution over time of the best configuration found. On the right side, a representation of the search space and the sampled points is illustrated. Specifically, since the considered input space is 4 dimensional, it is impossible to provide a visual representation of it as it is. A dimensional reduction has thus been applied via *Principal Component Analysis* (PCA), requiring a 2-dimensional output space. In this way, an interpretable visualization has been achieved, while preserving a consistent relationship between the data points.

Low-dimensional data, represented as points in the scatter plot, are colored according to their $C_D$ value. This allows to understand and highlight patterns. Indeed, in this case it is possible to see how clustered data shows similar low $C_D$ values, illustrating the correct evaluation of the clay car black box function by the optimization algorithm.

To better understand the potential of a multi-dimensional optimization, Figure 3.20 comes to help. In the picture, a direct comparison between $C_D$ values obtained during the 1-dimensional and 4-dimensional optimization is shown, as well as the evolution over time of the best result.

To correctly evaluate the information in the graph, only the final values should be considered. Indeed, the 1-dimensional analysis is not governed by any optimization algorithm but just by a simple sweep movement. The core of the comparison then becomes the difference in magnitude $\Delta C_D$ between the scored drag coefficients rather than the efficiency in the improvement.

As it is possible to see from Figure 3.20, at the end of the 4-dimensional optimization a better solution has been found, leading to an improvement of $\Delta C_D = -0.0004$. Even though it is a small delta, the value is higher than the uncertainty coming from the repeatability tests, leading to the reliability of the result.

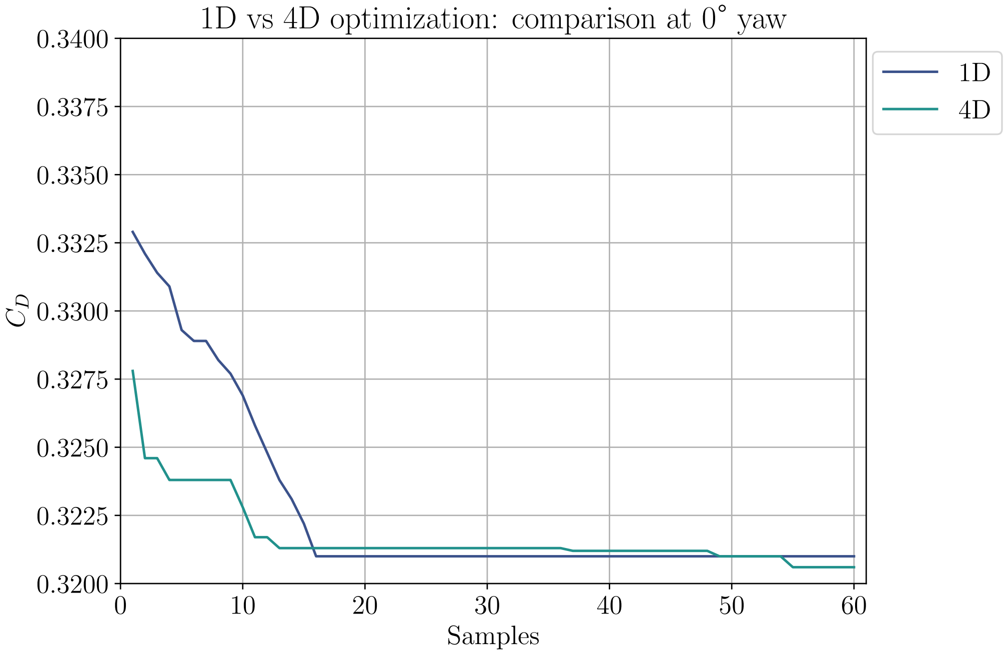

**Figure 3.20:** Performance comparison between the 1-dimensional and the 4-dimensional optimization. Achieved $C_D$ values are compared

Connecting the changes in the $C_D$ coefficient to the gained or lost car range is a difficult process, since the vehicle dynamics is extremely complex. However, the rule of thumbs introduced in Section 2.7.1 allows to roughly estimate what savings and improvements might be obtained via these new diffuser configurations.
Specifically, it was described that the energy losses can be broken down in two parts: a constant rolling resistance $F_{roll}$ and an optimizable air drag resistance $F_{drag}$. Since $F_{roll}$ was not studied and the real $F_{drag}$ of the car, without the mechatronic system, is unknown due to modifications such as the covered inlets and the wheel covers, it is impossible to estimate the individual contributions of the two factors.
Nevertheless, the variation in the total energy losses can be roughly estimated by considering the $\Delta C_D$ obtained in the 1D-4D optimization comparison. Recalling Equation 2.11, according to WLTP regulations and considering an average speed of $v = 82\,km/h$ and a front area $A = 2.87\,m^2$, the improvements in $C_D$ leads to

$$\Delta e_{loss,\,tot} = 86\,\Delta C_D\,A = 0.1\,\frac{Wh}{km}$$

Assuming that the vehicle consumption reported in Table 2.5 corresponds to the 1-dimensional optimized diffuser, the energy improvements coming from the 4-dimentional optimization are

$$\Delta e_{\%} = 1 - \frac{e_{loss,\,tot} - \Delta e_{loss,\,tot}}{e_{loss,\,tot}} = 0.05\%$$

Taking into account the actual range of the vehicle reported in [6], the car autonomy can be extended for

$$\Delta s = 585 \cdot \frac{0.05}{100} = 0.3\,km$$

In addition to that, it is also interesting to observe an asymmetry in the best configuration found. Indeed, since PVT presents a symmetric test section and the mounting points on the balance allow the clay car model to be placed in the exact center of the test section, there is no apparent reason that justifies the outcome. Consequently, the real cause must be related to the car. As previously discussed in Section 2.3, the clay model presents a more or less symmetric body and shape, while the chassis and floor are characterized by asymmetric elements. This possibly led the optimization algorithm to investigate non-symmetric solutions in order to counterbalance the asymmetry caused by the car floor.
Figure 3.21 provides the graphical representation of the different diffuser configurations obtained after the 1-dimensional and 4-dimensional optimizations.

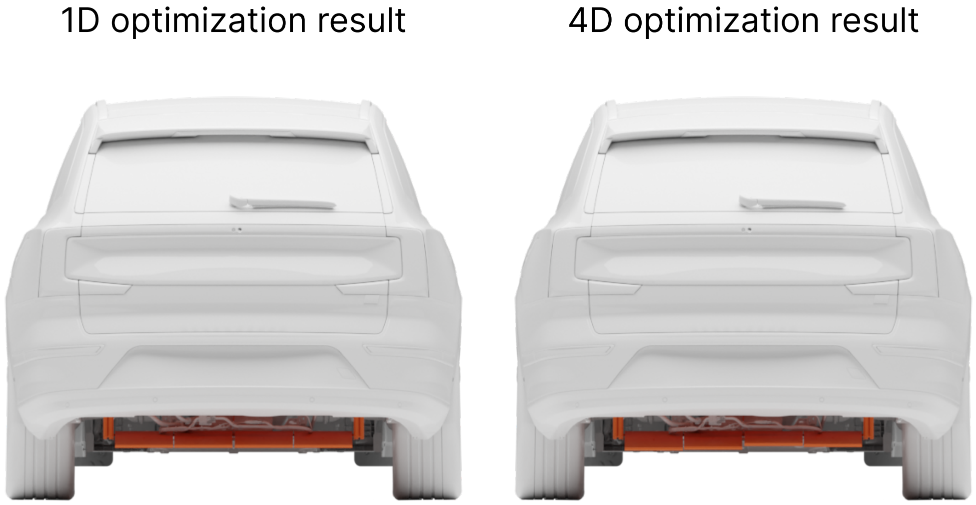

**Figure 3.21:** Visualization of the optimized diffuser shape obtained at 0° yaw. On the left side, the outcome from 1-dimensional optimization is illustrated. On the right side, instead, the 4-dimensional optimization one.

Additionally, a CFD analysis was conducted on the digital twin of the clay car model. The considered vehicle shape was the one obtained from both the 1-dimensional and 4-dimensional optimization runs. The numerical analysis was undertaken to verify the result consistency as well as to obtain a visual representation of the difference in the vehicle wake before and after the advanced optimization.
From the CFD, a $\Delta C_{D,CFD} = -0.0007$ was observed while, as mentioned before, a $\Delta C_D = -0.0004$ was obtained with the wind tunnel test. Since the absolute difference between the two

$$\Delta_{\Delta C_D} = |\Delta C_{D,CFD} - \Delta C_D| = 0.0003$$

is smaller than the wind tunnel sensitivity, reported in Section 2.4, the mechatronics optimization has to be considered consistent.

Figure 3.22 shows a visualization of the vehicle rear wake. Particularly, Figure 3.22a illustrates the one obtained from the 1-dimensional diffuser optimization whilst Figure 3.22b the one coming from the 4-dimensional process. As it is possible to see, the velocity vectors in the 4-dimensional optimized wake are more orthogonal to the rear surface of the vehicle, and their magnitude is higher than the monodimensional case. This validates what discovered via wind tunnel tests, as the more orthogonal velocity vectors, the more aerodynamically efficient.

Additionally, an asymmetry in the wake can be easily observed. This is due the small averaging window used in the numerical analysis, set to 1 second and not due to the vehicle dynamic.

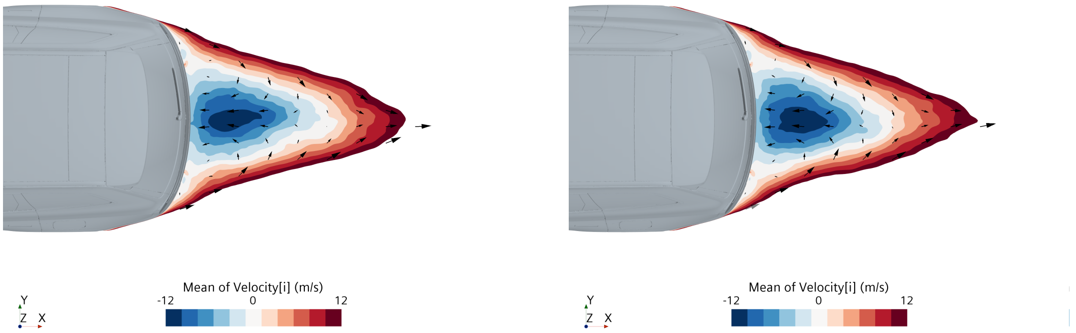

**(a)** 1-dimensional optimized diffuser case

**(b)** 4-dimensional optimized diffuser case

**Figure 3.22:** Velocity visualization obtained via CFD analyses for the optimized diffusers at 0° yaw.

Moreover, Figure 3.23 shows the normalized pressure distribution in the rear part of the vehicle, for both the 1-dimensional and 4-dimensional optimized case. Typically, low-drag optimized vehicles present high pressure in the rear to have more thrust and better overcome the drag effect. As it possible to see, Figure 3.23b shows higher and more symmetrically-distributed pressure, leading to better performance and confirming the optimality of the result.

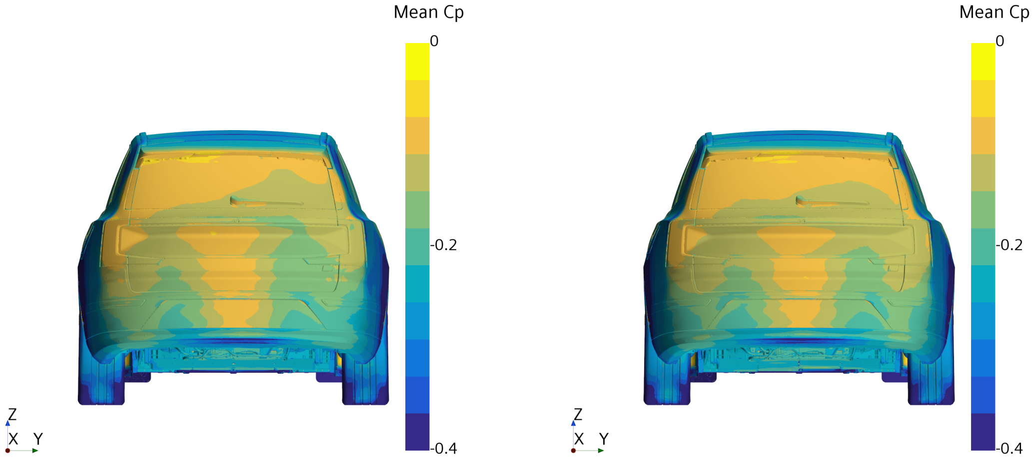

**(a)** 1-dimensional optimized diffuser case

**(b)** 4-dimensional optimized diffuser case

**Figure 3.23:** Normalized pressure (adimensional pressure coefficient) contour plot obtained from the diffuser optimization at 0° yaw.

### 3.2.3 Optimization at -5° yaw

The same analysis has been conducted at $-5°$ yaw, with a wind speed of 140 $km/h$, blowing from the right side of the car. Data was collected in the same way as the test conducted at 0° yaw, initially by performing a monodimensional sweep of the diffuser, then by running a 4-dimensional optimization via the Urquhart surrogate model.

In Figure 3.24 and Figure 3.25 the results from the tests are reported. As in the previous section, a transformation of the search space into a smaller hyperspace was made, to ease the visual representation of the investigated points.

Specifically, a $C_{D_{min}} = 0.3413$ was scored for the 1-dimensional test while a $C_{D_{min}} = 0.3375$ was obtained during the 4-dimensional optimization.

Figure 3.24 shows the same behaviour as the equivalent test executed at 0° yaw, with the presence of a unique minimum. As expected, the diffuser configuration that provides the drag coefficient minimization, $\theta = 6°$, is slightly different that the one obtained at 0°. This is naturally due to the changed wind direction. Even though the obtained solution is different, it is still quite consistent with the previous result. This is a good indicator of data reliability, as a $-5°$ yaw position does not drastically change the dynamics of the vehicle.

A more insightful aspect is the samples distribution occurred from the multidimensional optimization. As it is possible to see from Figure 3.25, the algorithm focused the sampling only in half of the search space, with a clustered batch in the neighbourhood of the minimum. This satisfies the prior assumption that a set of configurations, i.e. the ones that enhance high performances with the wind blowing from the left side, are discarded in the investigation.

The full comparison between the mono and multidimensional analyses is reported in Figure 3.26. As the analogous 0° yaw case, the most valuable information is the difference in magnitude between the best $C_D$ found and not the evolution over time.

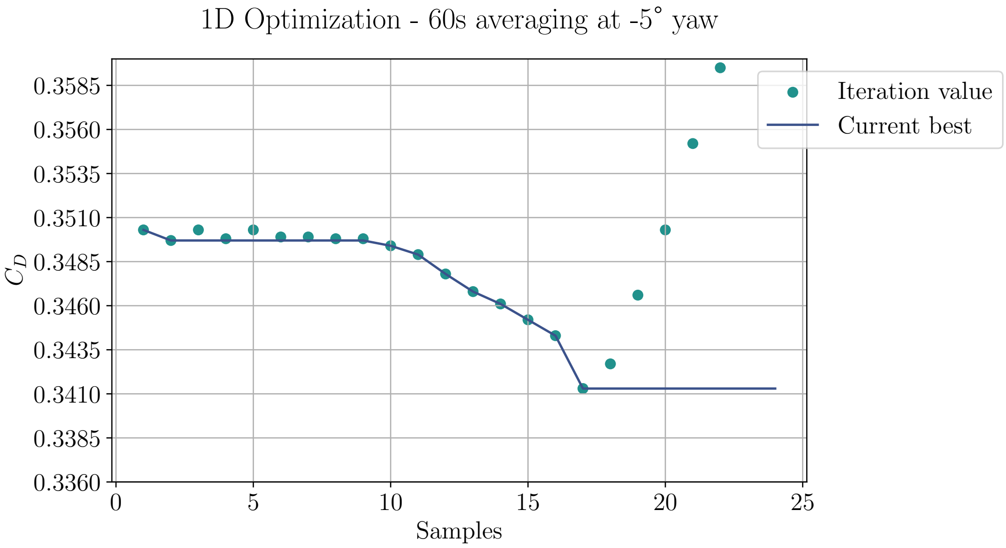

**Figure 3.24:** 1-dimensional mechatronics test to optimize the clay car drag coefficient $C_D$ at $-5°$ yaw and wind speed of $140\,km/h$.

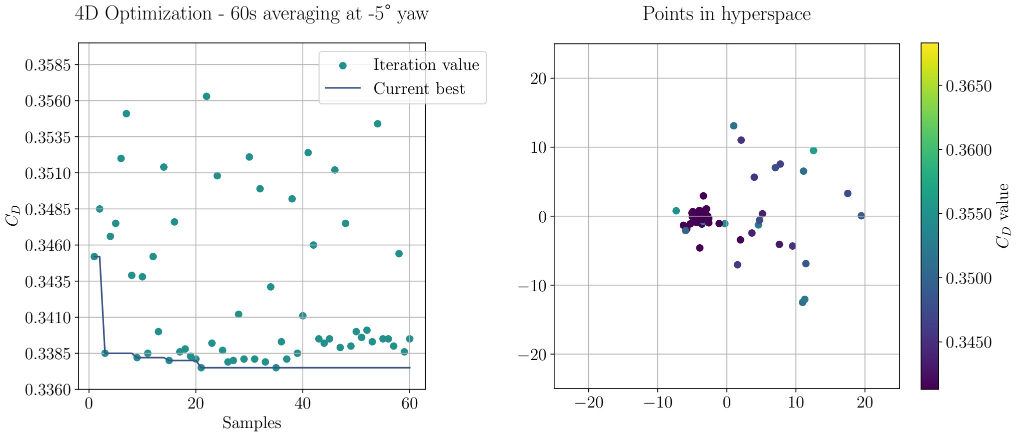

**Figure 3.25:** 4-dimensional mechatronics test to optimize the clay car drag coefficient $C_D$ at $-5°$ yaw and wind speed of $140\,km/h$. On the left side, $C_D$ values obtained from the sampling process are shown along with the evolution of the best value found over time. On the right side, a 2-dimensional hyperspace is shown, to better represent the disposition of the points and their relative distance.

With the 4-dimensional optimization, a significant reduction of $\Delta C_D = -0.0038$ was achieved.

The best configuration can be observed in Figure 3.27. As shown, the flaps disposition is asymmetric, with the flap on the right side completely up, while the middle one, as well as the one on the left, takes an uncommon configuration.

As reported in Section 3.2.2, an estimation of the reduction in energy consumption as well as vehicle range extension can be made. By recalling the calculations done for the 0° yaw case,

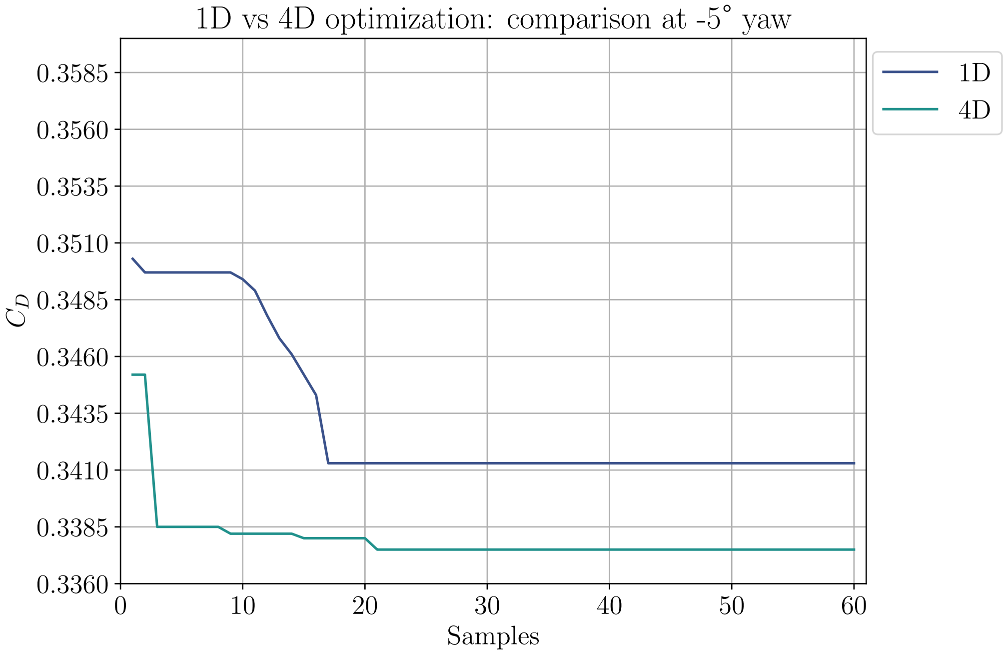

**Figure 3.26:** Performance comparison between the 1-dimensional and the 4-dimensional optimization conducted at $-5°$ yaw. Achieved $C_D$ values are compared.

$$\Delta e_{loss} = 86\,\Delta C_D\,A = 0.94\,\frac{Wh}{km}$$

Even in this case, by assuming that the vehicle consumption reported in Table 2.5 corresponds to the 1-dimensional optimized diffuser, the energy improvement is

$$\Delta e_{\%} = 1 - \frac{e_{loss,\,tot} - \Delta e_{loss}}{e_{loss,\,tot}} = 0.51\%$$

Considering the already introduced battery capacity from [6]

$$\Delta s = 585 \cdot \frac{0.5}{100} = 3\,km$$

This time the possible range extension has a significant impact as, for example, 3 $km$ might do the difference for a driver for reaching a charging station.

Even for the $-5°$ yaw case, the CFD analysis was conducted to verify the consistency of the results, as well as to see the changes in the vehicle wake. From that, a $\Delta C_{D,CFD} = 0.0061$ was found, leading to $\Delta_{\Delta C_D} = 0.0023$. This time the delta in the $C_D$ value is higher than the wind tunnel sensitivity, suggesting that even more improvements could be found. Since the optimization was already validated in Section 3.2.2, this does not represent any concern for the results, thus the optimized value can be considered validated as well.

Figure 3.28 shows the visualization of the vehicle wake for both the 1D and 4D case. As it is possible to observe, a stronger asymmetry characterizes the graph. In this case, not only the small averaging time influences the final shape, but also the direction of the wind, which blows on the right side of the car. Consequently,

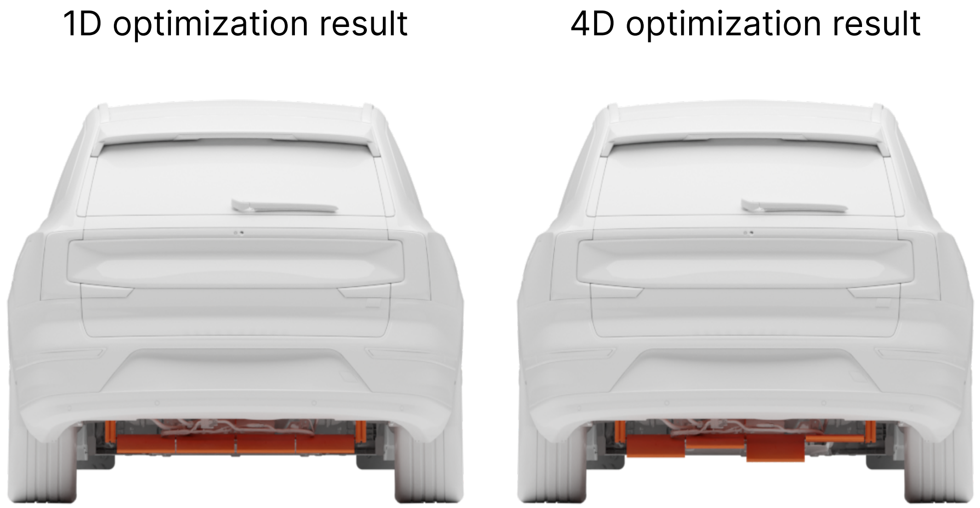

**Figure 3.27:** Visualization of the optimized diffuser shape obtained at $-5°$ yaw. On the left side, the outcome from 1-dimensional optimization is illustrated. On the right side, instead, the 4-dimensional optimization one.

a non-symmetric characterization of the velocity vectors can be observed, more remarkably in the 1-dimensional scenario. In the 4D, instead, the diffuser is able to counterbalance the side-wind effect, leading to a more symmetrical wake. Moreover, higher velocity regions can be observed, achieving $-12\,m/s$ in the central part. This causes higher pressures in the rear part of the vehicle, as it can be observed in Figure 3.29.

As introduced before, higher rear pressure guarantees more thrust to overcome the drag backwash, leading to a smaller $C_D$ value.

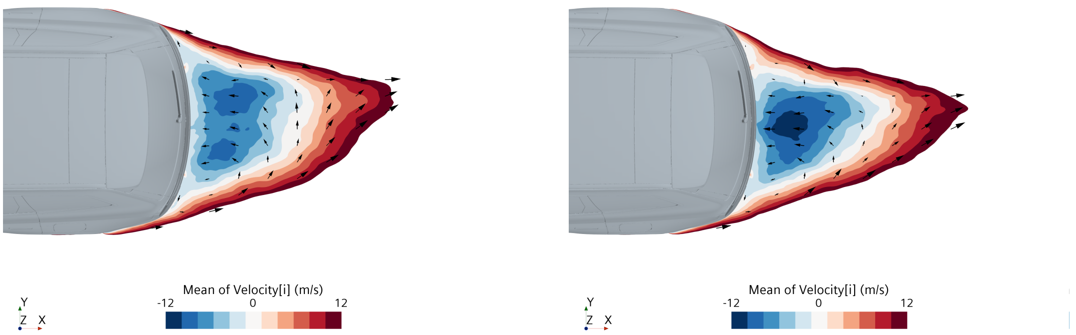

**(a)** 1-dimensional optimized diffuser case

**(b)** 4-dimensional optimized diffuser case

**Figure 3.28:** Velocity visualization obtained via CFD analyses for the optimized diffusers at $-5°$ yaw.

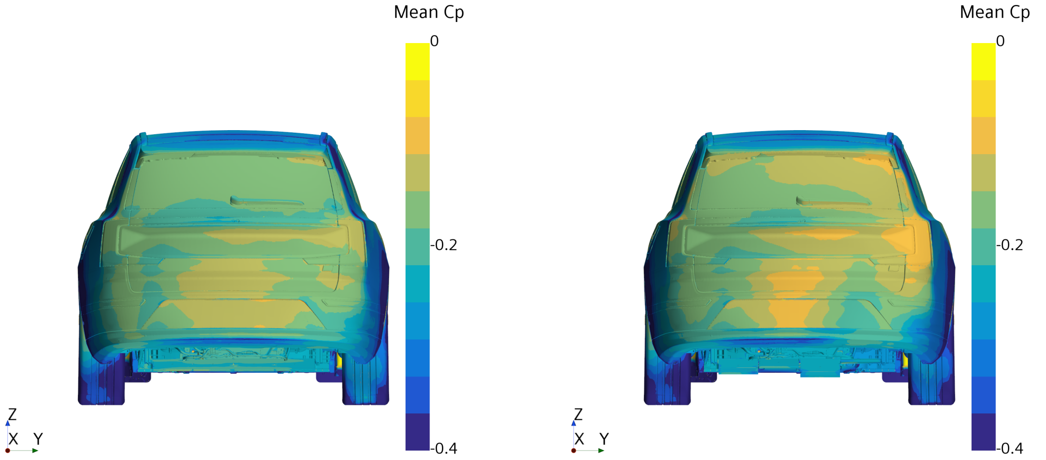

**(a)** 1-dimensional optimized diffuser case

**(b)** 4-dimensional optimized diffuser case

**Figure 3.29:** Normalized pressure (adimensional pressure coefficient) contour plot obtained from the diffuser optimization at $-5°$ yaw.

### 3.2.4 Optimization at -10° yaw

A further investigation at $-10°$ yaw has been conducted, by keeping the same nominal speed for the wind, averaging time and car configuration.
From the monodimensional test, a unique configuration led to the drag coefficient minimization. As it is possible to observe from Figure 3.30, the $C_D$ behaviour caused by the sweep movement is the same as the $0°$ and $-5°$ yaw cases, only distinguished by the coefficient magnitudes.

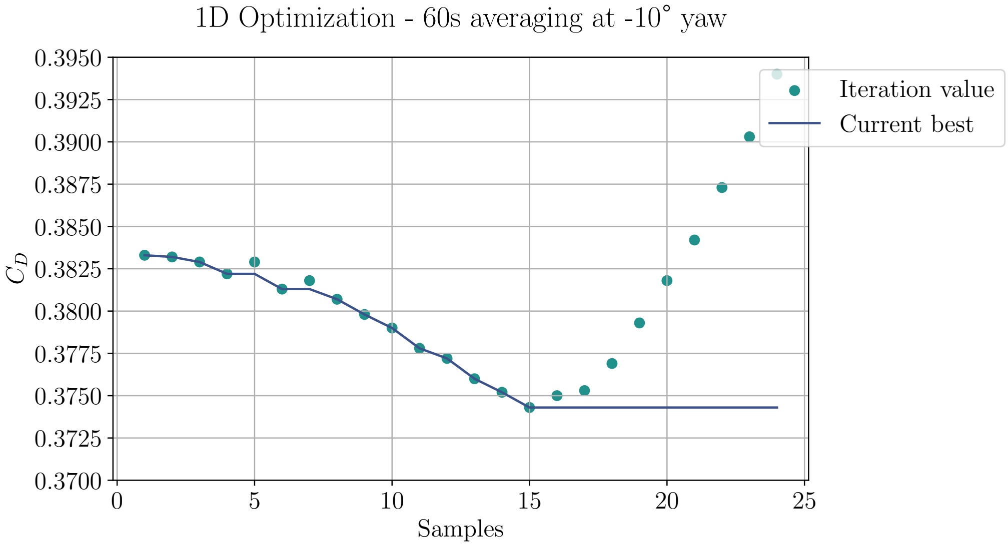

**Figure 3.30:** 1-dimensional mechatronics test to optimize the clay car drag coefficient $C_D$ at $-10°$ yaw and wind speed of $140\,km/h$.

The 1-dimensional optimization led to the drag coefficient minimization, reaching

$C_{D_{min}} = 0.3743$. Specifically, the best value was obtained with a flap configuration at $\theta = 4°$. Even in this case, the diffuser position that allows the drag force minimization is different from the previous ones, but still very similar. This is an additional indication of stability of the system, as the dynamic did not dramatically change even at $-10°$ yaw.

Speaking about the 4-dimensional optimization test, the Urquhart surrogate model was used to seek the optimal configuration. The result of the process can be observed in Figure 3.31. As the $-5°$ case, the surrogate model focuses only on half of the search space, creating a clustered set of points in the neighbourhood of the minimum. All the considerations made for the previous cases regarding the correct interpretation by the algorithm are still valid. Additionally, the best diffuser configuration led to $C_{D_{min}} = 0.3710$, namely $\Delta C_D = -0.0033$ of improvements compared to the 1-dimensional optimization result.

The evolution over time, as well as the comparison between the monodimensional and multi-dimensional optimizations, can be observed in Figure 3.32. Figure 3.33 shows instead the final diffuser configuration achieved after the 1-dimensional and 4-dimensional optimization processes. The flap dispositions are once again different from the 0°- and $-5°$-yaw test case.

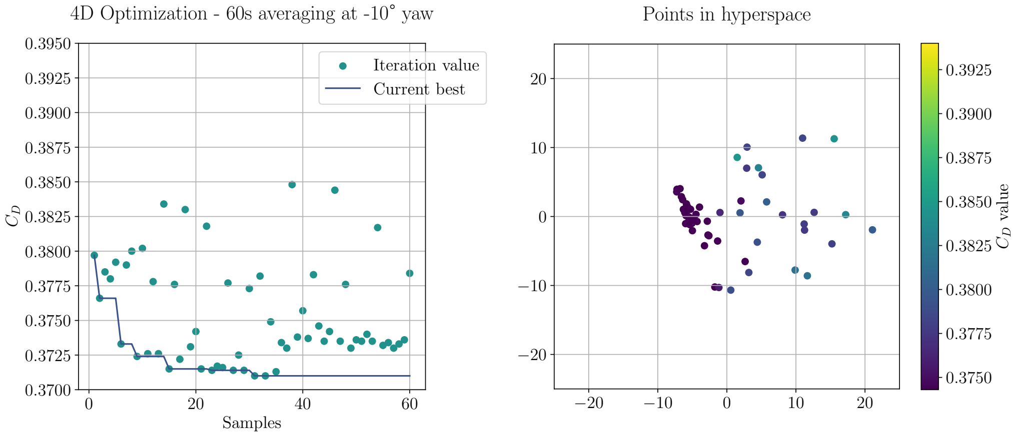

**Figure 3.31:** 4-dimensional mechatronics test to optimize the clay car drag coefficient $C_D$ at $-5°$ yaw and wind speed of 140 $km/h$. On the left side, $C_D$ values obtained from the sampling process are shown along with the evolution of the best value found over time. On the right side, a 2-dimensional hyperspace is shown, to better represent the disposition of the points and their relative distance.

As previously done for the 0° and $-5°$ case study, the estimated reduction in energy consumption and the range extension can be assessed, to better understand what might be the impact in performances if an optimized diffuser was used.

$$\Delta e_{loss} = 86\, \Delta C_D\, A = 0.81\, \frac{Wh}{km}$$

Assuming once again that the vehicle consumption reported in Table 2.5 is the one associated to the 1-dimensional optimized diffuser

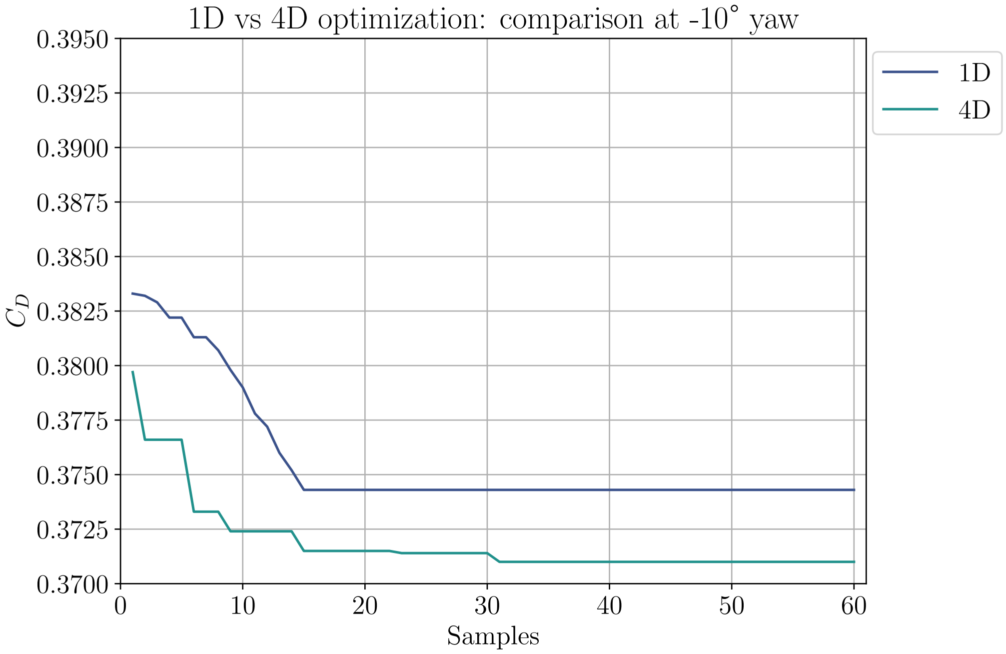

**Figure 3.32:** Performance comparison between the 1-dimensional and the 4-dimensional optimization. Achieved $C_D$ values are compared.

$$\Delta e_{\%} = 1 - \frac{e_{loss,\,tot} - \Delta e_{loss}}{e_{loss,\,tot}} = 0.44\%$$

Considering the already introduced battery capacity from [6],

$$\Delta s = 585 \cdot \frac{0.5}{100} = 2.58\,km$$

Even in this case, the introduction of 4-dimensional optimized diffuser for a $-10°$ yaw angle led to a significant improvement of $2.58\,km$.

Even in this case, a CFD analysis was conducted to verify the consistency of the result. From the numerical computation, a $\Delta C_{D,CFD} = 0.0024$ was achieved, leading to $\Delta_{\Delta C_D} = 0.0009$.

The difference in the $C_D$ improvements between the wind tunnel and CFD tests is higher than the wind tunnel sensitivity, but still small enough to validate the outcome.

The 4-dimensional optimization, as can be observed from Figure 3.34, allows to counterbalance the strong side-wind on the right side of the vehicle, leading to a more symmetrical wake shape. Additionally, in the 4D case the velocity vectors are more orthogonal to the rear surface, guaranteeing higher pressure to better overcome the drag effect. Nevertheless, smaller velocity were achieved.

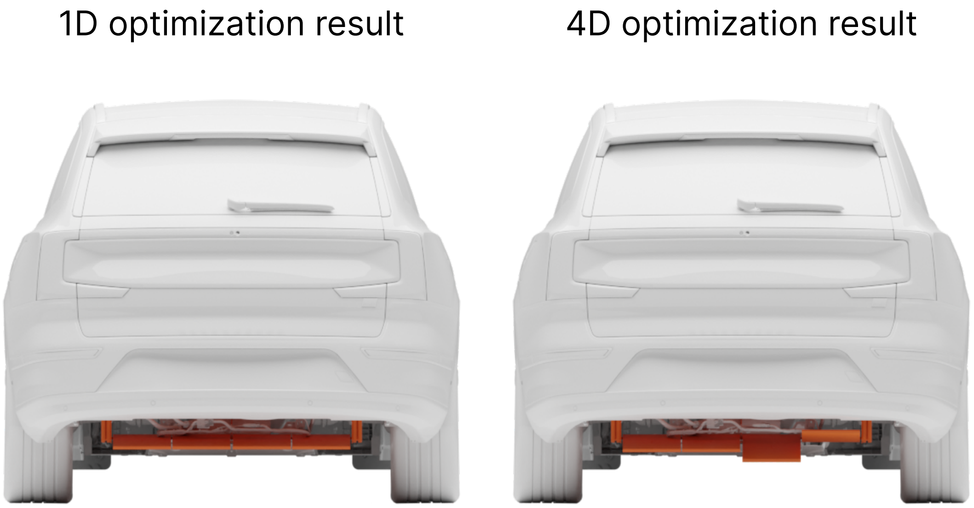

**Figure 3.33:** Visualization of the optimized diffuser shape obtained at $-10°$ yaw. On the left side, the outcome from 1-dimensional optimization is illustrated. On the the right side, instead, the 4-dimensional optimization one.

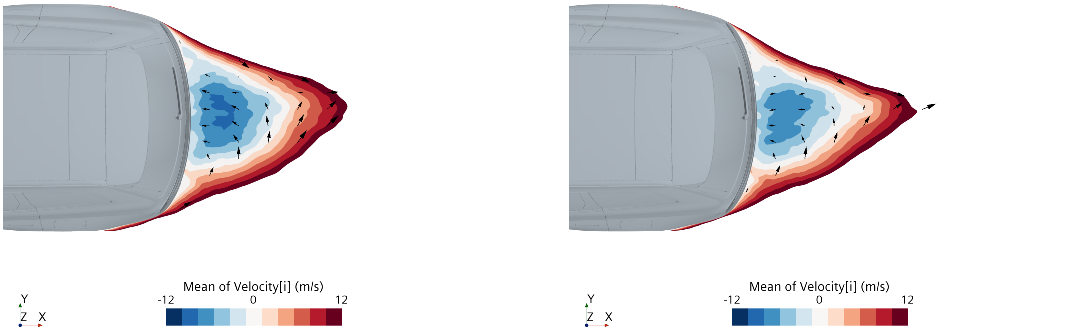

**(a)** 1-dimensional optimized diffuser case

**(b)** 4-dimensional optimized diffuser case

**Figure 3.34:** Velocity visualization obtained via CFD analyses for the optimized diffusers at $-10°$ yaw.

Figure 3.35 illustrated the normalized pressure distribution on the rear part of the vehicle. As it is possible to observe, the pressure is more evenly distributed, leading to better vehicle stability.

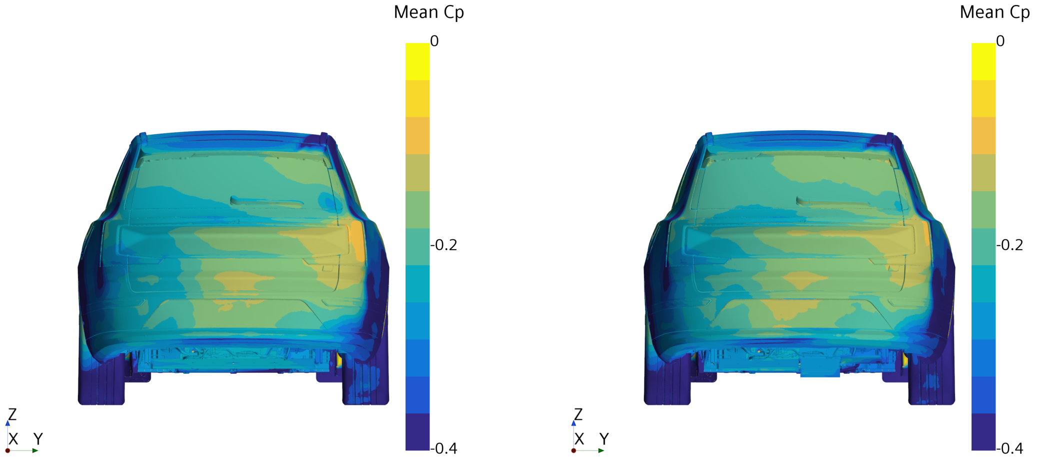

**(a)** 1-dimensional optimized diffuser case

**(b)** 4-dimensional optimized diffuser case

**Figure 3.35:** Normalized pressure (adimensional pressure coefficient) contour plot obtained from the diffuser optimization at $-10°$ yaw.

### 3.2.5 Wind-averaged-drag coefficient

In the previous sections, the improvements in the drag coefficient obtained via the mechatronic optimization approach have been illustrated, analyzing the impact on the vehicle consumption and car range.

The aerodynamic resistance component is identified by the drag coefficient at 0° yaw, which represents the drag in condition of no lateral wind [15]. As stated in [4] and observed in the experiment results, the drag coefficient almost always increases with the yaw values but will tend to underestimate the real vehicle drag in conditions where wind is present. Additionally, Figure 3.36 illustrates the velocity decomposition in a cross-wind scenario. This allows to better understand the relation between the vehicle's velocity and the wind's one. It is important to underline that in the case in which the vehicle is not moving, namely $U_V = 0$ as during a wind tunnel test, the wind angle $\varphi$ corresponds to the yaw angle $\psi$ and the wind speed magnitude becomes the resultant velocity, i.e. $U_W = U_R$.

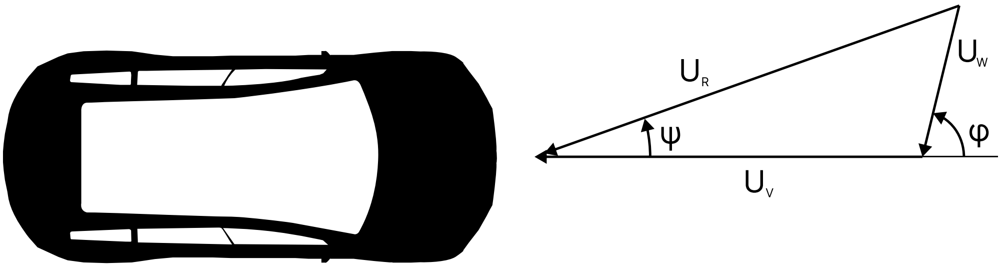

**Figure 3.36:** Velocity diagram for a car in a crosswind. $\varphi$ is the wind angle relative to the vehicle axis, $\psi$ yaw angle, $U_V$ car speed, $U_W$ wind speed and $U_R$ resultant velocity.

The need of creating a more comprehensive and accurate value that represents the

true drag coefficient of a car arises, to better estimate the real-world energy consumption of a vehicle.
In [16], Howell et al. introduced a drag coefficient specifically designed for a drive cycle, known as the cycle-averaged-drag coefficient. This coefficient was developed based on the concept of wind-averaged-drag and takes into account variations in vehicle speed and wind speed using meteorological data. The variability of the yaw angle was determined using the probabilities of wind speed direction obtained from the Weibull function, assuming equal probability for wind direction. The impact of wind shear was also considered, taking into consideration the terrain characteristics of different sections of the drive cycle. The findings revealed that assuming the aerodynamic resistance to be solely determined by the drag coefficient at 0° yaw, underestimated the realistic drag represented by the cycle-averaged-drag coefficient. The cycle-averaged-drag coefficient relies on the relationship between the drag increase and the yaw angle, as measured in the wind tunnel.
The definition of cycle-averaged-drag coefficient introduced by Howell et al. is reported in Equation 3.3

$$C_{DWC} = 0.48C_{D0} + 0.42C_{D5} + 0.10C_{D10} + 0.012C_{D15} \tag{3.3}$$

with $C_{D\psi}$ the drag coefficient obtained in the wind tunnel at a yaw angle $\psi$.
The $C_{DWC}$ definition was obtained in [16] via regression analysis of the data collected from the authors experiment. In the paper, it is also stated that $C_{DWC}$ is always higher than $C_{D0}$, with a variation between 1.5% and 11.6%.
It is interesting to note that in 1984 an early recognition of the need for a better representation of the true drag coefficient of a vehicle was introduced by Kramer in [17], in which he proposed a different but realistic drag coefficient $C_{DK}$

$$C_{DK} = \frac{1}{2}C_{D0} + \frac{1}{3}C_{D5} + \frac{1}{6}C_{D10} \tag{3.4}$$

It is interesting then to try to estimate the wind averaged drag even for this work, in order to better estimate a more comprehensive drag coefficient for the optimized clay car model. Since in this project tests at ±15° were not conducted, only the first 3 terms from Equation 3.3 will be considered, namely $C_{D0}$, $C_{D5}$ and $C_{D10}$, leading to Equation 3.5. Due to the symmetry of the wind tunnel, $C_D$ values obtained at $-5°$ and $-10°$ yaw are considered to be the same that would have been obtained at $+5°$ and $+10°$ yaw, with a symmetric disposition of the diffuser flaps.

$$C_{DWC} = 0.48C_{D0} + 0.42C_{D5} + 0.10C_{D10} \tag{3.5}$$

It is curious to observe that the considered coefficients in Equation 3.5 now sum to 1, as the ones in Equation 3.4. Substantially, the two equations slightly differ for the weight distributions, thus importance, that each $C_{D\psi}$ has.
During the optimization process, different configurations for the rear diffuser have been found. In particular, at each yaw angle $\psi$ a unique optimal position was discovered. In order to understand which is the best configuration that lead to higher performances at a cross-yaw level, the cycle-averaged-drag coefficient can be computed for each design, eventually choosing the one that leads to the minimum.

The $C_D$ values associated to the 1-dimensional optimized diffuser are reported in Table 3.7.

| | $\boldsymbol{\psi = 0°}$ | $\boldsymbol{\psi = -5°}$ | $\boldsymbol{\psi = -10°}$ |
|---|---|---|---|
| $\theta = 5°$ | 0.3210 | 0.3443 | 0.3750 |
| $\theta = 6°$ | 0.3220 | 0.3413 | 0.3753 |
| $\theta = 4°$ | 0.3222 | 0.3452 | 0.3743 |

**Table 3.7:** Summary of the $C_D$ values obtained during the 1-dimensional optimization at different yaw angles.

The diagonal of the table contains the best $C_D$ values obtained during the optimization run. Considering the different drag coefficients, the cycle averaged drag can be easily computed using both the definitions introduced by Howell and Kramer, Equations 3.5 and 3.4 respectively. The results are reported in Table 3.8.

| | $\boldsymbol{\theta = 5°}$ | $\boldsymbol{\theta = 6°}$ | $\boldsymbol{\theta = 4°}$ |
|---|---|---|---|
| $C_{DWC}$ | 0.3362 | 0.3354 | 0.3371 |
| $C_{DK}$ | 0.3378 | 0.3373 | 0.3386 |

**Table 3.8:** Cycle-averaged-drag coefficients obtained from 1D optimized diffuser solutions.

Surprisingly, even though $C_{D0}$ weights more in both Equations 3.4 and 3.5, the solution that leads to a minimum cycled average drag coefficient is the configuration found during the $C_D$ minimization at $\psi = -5°$. This directly leads to a new remarkable consideration: to create more efficient vehicles, subjected to cross-wind as real open-road scenarios, automotive industries should study and optimize a vehicle at $-5°$ rather than $0°$ yaw.

The same procedure could be done also for the 4-dimensional optimized diffuser, but the result would not be insightful, as the configurations are too asymmetric to provide low drag coefficients on a cross-yaw level.

Nevertheless, in a scenario in which the rear diffuser can actively change during the vehicle motion, the best solutions found for the diffuser at different yaw values could be applied and a new level of efficiency could be obtained. Specifically, Table 3.9 illustrates this.

| $\boldsymbol{\psi = 0°}$ | $\boldsymbol{\psi = -5°}$ | $\boldsymbol{\psi = -10°}$ | $\boldsymbol{C_{DWC}}$ | $\boldsymbol{C_{DK}}$ |
|---|---|---|---|---|
| 0.3206 | 0.3375 | 0.3710 | 0.3327 | 0.3346 |

**Table 3.9:** Cycle-averaged-drag coefficients obtained from 4D optimized diffuser solutions, assuming variable shape during the motion of the vehicle.

It is remarkable to see that, if a variable diffuser was implemented in a vehicle, the cycle-averaged-drag coefficient could be reduced by $\Delta C_D = 0.0027$ for both Howell's and Kramer's definition.

**Figure 3.37:** Visualization of the 4-dimensional optimized diffuser shape at different yaw values. In the scenario in which an active diffuser is implemented in a vehicle, its shape would change accordingly to best face side-wind conditions.

Figure 3.37 shows what the implementation of active aerodynamic components could look like in the future. During the vehicle motion, the rear diffuser can take different configuration to better adapt and counterbalance the side-wind effect, to always reach the most efficient configuration and maximize the car autonomy.

### 3.2.6 Pareto front and multi-objective optimization

In the previous sections, mono-objective optimization has been introduced and data coming from the respective tests has been illustrated. In particular, the analysis focused on the minimization of the drag coefficient values, to improve aerodynamics and thus reducing energy consumption.

Nevertheless, as mentioned in Chapter 1, several aspects must be taken into account while developing a vehicle. In the end, the final result should correspond to the best trade-off among all the several system parameters. By looking at the values reported in Sections 3.2.2, 3.2.3 and 3.2.4, good results from $C_D$ minimization have been obtained and a noticeable impact on the vehicle range was observed. However, no information about other parameter values and their evolution were provided.

Recalling the best configurations found during the optimization tests, the $C_{LR}$ and $C_{LF}$ values associated to the optimized flap disposition are reported in Table 3.10.

| **Angle** | $\boldsymbol{C_D}$ | $\boldsymbol{C_{LR}}$ | $\boldsymbol{C_{LF}}$ |
|---|---|---|---|
| 0° yaw | 0.3206 | 0.0526 | 0.1018 |
| −5° yaw | 0.3375 | 0.0761 | 0.1039 |
| −10° yaw | 0.3710 | 0.1013 | 0.1354 |

**Table 3.10:** $C_D$, $C_{LR}$ and $C_{LF}$ corresponding to the optimized diffuser configurations, obtained from the 4-dimensional mono-objective minimization.

The values reported in the table might not communicate much if considered alone. Since the following discussion and considerations regarding $C_{LR}$ and $C_{LF}$ would be the same, only the former is covered in this work.

By looking at Figure 3.38, it is possible to understand the true value of these results.

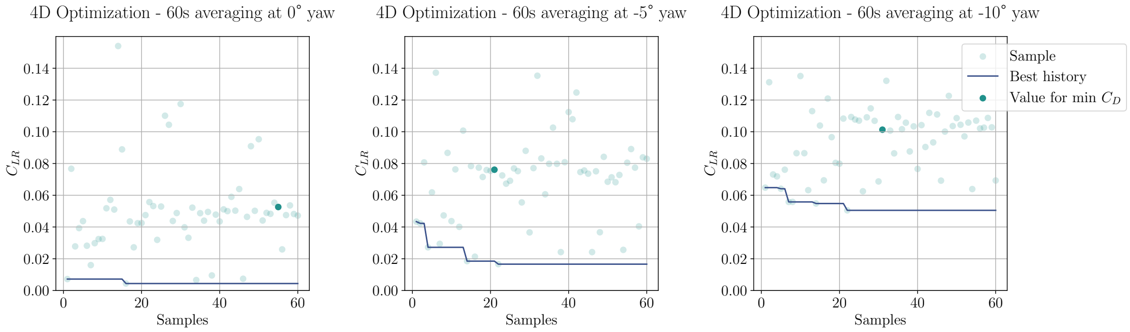

**Figure 3.38:** $C_{LR}$ values obtained during the $C_D$ mono-objective optimization. Samples and evolution over time of the best value found are displayed. The $C_{LR}$ value corresponding to configuration that minimized $C_D$ is highlighted as well. The clay car was tested at different yaw values (0°, $-5°$ and $-10°$ from left to right) and with a wind speed of 140 $km/h$.

It is immediate to observe that the $C_{LR}$ value, obtained from the configuration that minimizes the drag coefficient, is not the best result in terms of $C_{LR}$. This, as shown in the graph, occurred for all the tests conducted at different yaw value.
Moreover, the just introduced values cannot be considered a priori good solutions as their magnitude is quite different from the minimum that could have been obtained. Volvo EX90 is the biggest passenger car that the company nowadays produces. Since it belongs to the SUV-class, its weight is higher than conventional vehicles, leading to stiff stability even at high speeds. Nevertheless, since the mechatronic project aims to open the doors for advanced optimization procedures for all future clay car models, smaller and more sensitive to aerodynamics categories (such as sedan or coupe) might be affected by strong instabilities due to the non-optimized aerodynamics parameters.
Hence, it becomes necessary to start optimizing a vehicle with a more global approach, introducing multiple targets for the optimization process.
This directly leads to the so called multi-objective optimization, in which the target cost functions to be minimized include multiple variable parameters, weighted by different coefficients according to the importance or priority that data analysts want to provide.
The public version of the Urquhart surrogate model already includes the possibility to perform multi-objective optimization, by building a surrogate model for each target variable. For this case, as a proof of concept, the model has been exploited to try to minimize both $C_D$ and $C_{LR}$ coefficients in order to provide a better balanced solution.
The cost function was designed with the same weights for both the parameters, avoiding to favor one variable instead of the other.
From an engineering perspective, the best way to visualize and understand the results of the analysis is to employ the Pareto Front. Pareto Front is a mathematical tool to represent the set of all efficient solutions coming from a test, called Pareto efficient solutions. Specifically, these solutions are characterized by the impossibility of improving one parameter without worsening the other. They have therefore to be considered optimal, and equivalent to similar results. There is no way to understand

which is the absolute best, it will depend on the system designer and from case to case whether to choose one solution rather than another one. In the specific case, an optimal solution with low $C_D$ and high $C_{LR}$ cannot be better than a one characterized by high $C_D$ and low $C_{LR}$. It will depend on which performances the engineering teams want to provide to the vehicle under development.

To better understand the benefits of this approach, and how the sampling behavior changes from mono-objective to multi-objective investigation, the Pareto Front has been built also for the test case covered in Section 3.2.2 and can be observed in Figure 3.39. Figure 3.40 shows instead the Pareto front built from the multi-objective optimization.

On the x-axis, $C_{LR}$ values are displayed while the drag coefficient is represented by the y-axis. This kind of representation clearly illustrates how the sampling changed over time, as well as the explored points and the respective obtained results. Another way to see the different data distribution can be observed in the central and right pictures reported in both Figure 3.39 and 3.40. In these graphs the hyperplane, built according to Section 3.2.2, is represented. In the central figure, $C_D$ magnitudes are highlighted while $C_{LR}$ values can be observed in the right picture.

A more insightful information is contained in the Pareto Front. Typically, multi-objective optimization processes produce hockey-stick-shaped fronts and Figure 3.40 shows the same behavior. Nevertheless, the gathered data was not enough to produce an extended wall and only a portion of it has been obtained. As previously mentioned, the front is a set of all the Pareto efficient solutions, meaning that one point in the set is completely equivalent to another. Only system design and requirements can point out which solution might suit the problem the best.

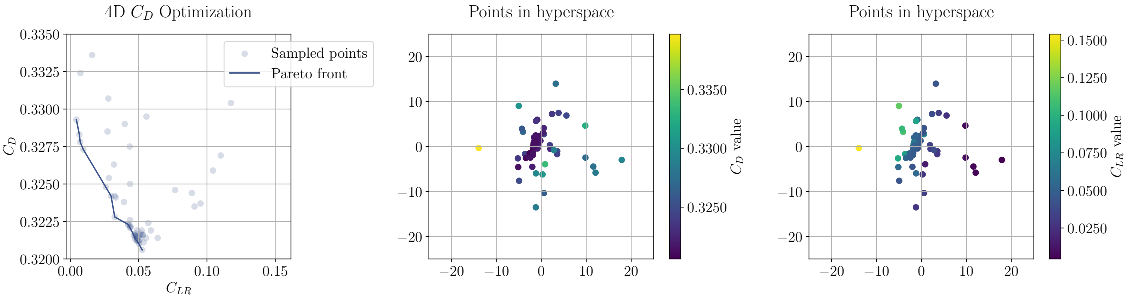

**Figure 3.39:** Pareto front built from mono-objective optimization. The test aimed to minimize $C_D$ values. The clay car was tested at 0° yaw and with wind speed of $140\,km/h$.

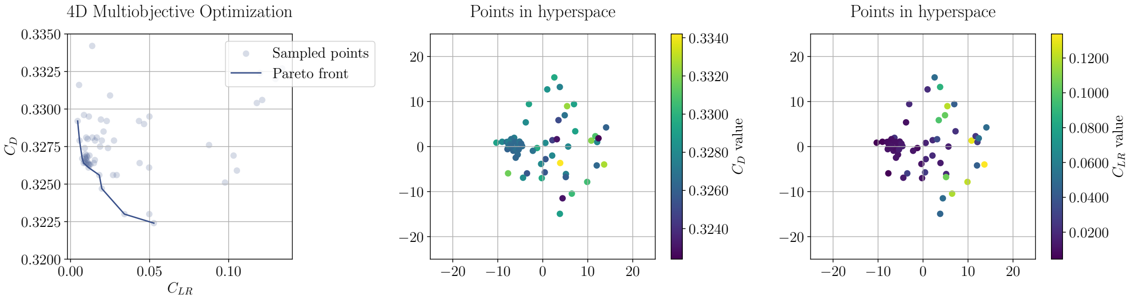

**Figure 3.40:** Pareto front built from multi-objective optimization. The test aimed to minimize both $C_D$ and $C_{LR}$ values. The clay car was tested at 0° yaw and with wind speed of 140 $km/h$.

## 3.3 Economic impact

As already introduced in Chapter 1, the goal of the mechatronic project is to bring a new and more efficient solution while designing a vehicle shape, in order to provide better performances via the optimization algorithms.

The main benefit from this investigation is the introduction of new, not obvious flap configurations that allow to minimize the aerodynamic drag, e.g. Section 3.2.2, 3.2.3 and 3.2.4, as well as find the optimal trade-off among parameters such as $C_D$ and $C_{LR}$ discussed in Section 3.2.6.

Nevertheless, another crucial benefit coming from the automation of this process is the economic advantages and savings that could be introduced if the mechatronic test rigs were exploited on a daily basis. In particular, in the following sections estimations about cost savings will be done for both current workflow and advanced optimization.

### 3.3.1 Potential savings on the current workflow

Already introduced in Chapter 1 and illustrated in Figure 1.5, the Aerodynamics team at Volvo Cars nowadays studies the vehicle characteristics mainly via an experience-based approach. Particularly, aerodynamics engineers start from an initial good configuration of the spoilers, such as diffusers, thanks to a previous CFD simulation and analysis. The simulation can last between 10 and 30 hours and allows to test the vehicle in a particular scenario, with a specific wind speed and yaw value. Even though several simulations can be run in parallel, such as 0°, −5° and −10° studies, plenty of hours are needed before looking at the vehicle behaviour.

After few iterations, once understood which might be the best car configuration, the team focuses on the wind tunnel tests. The clay car model is brought in the test room and the configuration that minimizes the drag coefficient is tested, by performing a sweep of at least 3 different diffuser angles.

The exploited method is a pure trial and error approach, meaning that no guarantees that a new better minimum will be found. Moreover, as Figure 1.5 shows, the procedure takes time and a repeated start and stop of the wind tunnel.

Specifically, to test out one diffuser configuration, the procedure is estimated to take $5\,min$, divided as following

1. Start the wind tunnel, wait for the balance signal and to reach nominal speed: about $3\,min$
2. Run the test: $1\,min$
3. Bring the wind speed to $0\,km/h$: about $1\,min$
4. Get in the wind tunnel, apply the new configuration and go out: about $4\,min$

Additionally, the diffuser tests are repeated for each car configuration, namely the clay car with additional changes, such as covered wheels or inlets, addition of roof flaps or deflectors. To change the car configuration, $10\,min$ are estimated to be needed by the aerodynamics team.

Summarizing, a total of $37\,min$ is necessary to completely study a new car configuration, but $34\,min$, or the 91.9%, are downtime.

By exploiting the mechatronics solution, the current workflow can be dramatically accelerated. Assuming to have all the car parameters of interest controlled via mechatronics, such as wheel deflectors, flaps and diffuser, the new estimated times, verified through this work, are

1. Start the wind tunnel, wait for the balance signal and to reach nominal speed: about $3\,min$
2. Change car configuration via mechatronics: about $20\,s$
3. Move the diffuser to a new position: max $20\,s$
4. Run the test: about $90\,s$
5. Repeat step 3) and 4) other two more times
6. Take the wind down: about $1\,min$

By considering the same car configuration and 3 diffuser sweep tests, less than $10\,min$ are needed to assess the study, leading to a 73.4% time reduction and a new downtime rate of 54.2%. The achieved time reduction naturally translates into economic savings. Indeed, by outlining the costs per hour associated to the wind tunnel usage, roughly the same percentage could be saved in terms of money.

### 3.3.2 Potential savings on advanced optimization

Briefly mentioned in Section 2.5.2, if no optimization algorithms were applied, a total of 15.5 years would be needed to completely investigate the 4-dimensional search space and find the best car configuration that minimized the desired variable.

The obtained results were quite impressive, leading to a remarkable reduction in energy consumption and extension of the vehicle range.

If such results were obtained using only a 4-parameter, by introducing more system parameters, such as wheel deflectors, rear spoilers and front diffusers might lead to even higher and remarkable improvements in a vehicle, reaching a new design level via morphing surfaces.

By adding new variables to the system, a rapidly growing complexity is achieved, described by Equation 3.6

$$C = \prod_{i=1}^{N} \delta_i \tag{3.6}$$

where $C$ represents the complexity, i.e. the number of combinations that could be investigated in the system, $N$ the total number of parameters and $\delta$ the dimension of the search space in a specific direction.
For this project, Equation 3.6 takes the following shape

$$C = \prod_{i=1}^{4} 46 = 4477456$$

By considering then the total amount of time needed for testing a specific configuration, it is easy to estimate the overall time that would be needed to seek the search space.

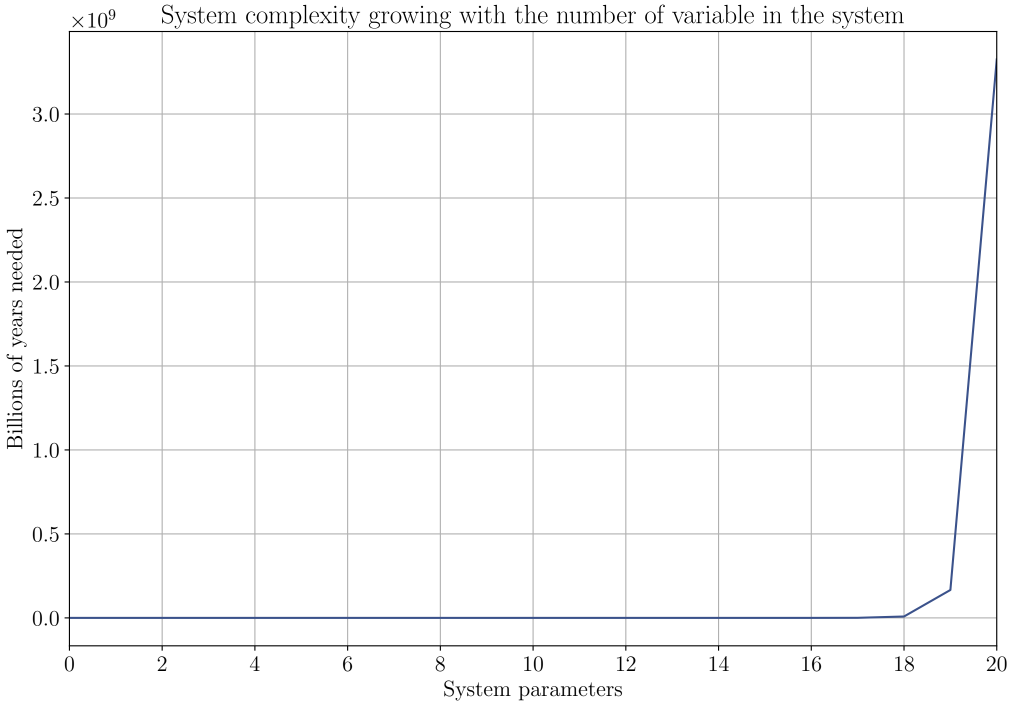

**Figure 3.41:** System complexity growing exponentially with the number of variables present in the system. In the graph, each variable range was considered the same and equal to 46, as the one for this project. On the y-axis, the number or years required to solve the system are pointed.

Once again, the need of exploiting ad-hoc optimization algorithms is fundamental to solve the system in a finite time, as highlighted by Figure 3.41. However, once introduced them, the benefit for the company is countless, as the wind tunnel time saved for investigating optimal designs is drastically reduced, thus its cost.
Finally, as briefly mentioned in 3.2.5, the future for making vehicles reach higher levels of efficiency lies in the introduction of active aerodynamics components. Elements such as rear spoilers, diffuser, wheel deflectors and more could be made change in shape during a vehicle motion to always guarantee the most efficiento.
Sport car manufacturer companies, such as Lamborghini and Porsche, already introduced in the past active aerodynamic components to increment the downforce and

reduce instability at high speeds. This, however, does not aim to make the vehicle energy efficient as the technology does not take into account cross-wind scenarios. A good approach, then, might be the introduction of morphing surfaces that change design according to pressure values, to provide the best performance and lower down the drag force as much as possible. Example of this technology are already known in the aircraft literature [18] [19] [20], but research and implementations still lack in the automotive field.

# 4

# Conclusion

This thesis aimed at investigating a new advanced automated workflow for studying the aerodynamics of a vehicle during its development stage. Specifically, a smoother and faster system was proposed, by relying less on computational fluid dynamics analyses and focusing more on wind tunnel clay car testing. In such manner, more frequent and effective iterations between the design and the aerodynamics department in a car manufacturer company can occur, bringing new and better vehicle models on the market at higher pace.

The project focused on the innovation of current wind tunnel tests, improving both the interaction with the test facility and the test object. Particularly, a seamless and scalable system was developed for actively controlling and reading data from the wind tunnel, realizing a plug-and-play workflow in which the test object takes the core role.

In details, an advanced clay car model that includes moving components actuated by mechatronics has been proposed. As a proof of concept, a 4-dimensional rear diffuser has been implemented.

The work was divided in two parts: an automated 1-dimensional optimization of the rear diffuser to mimic the investigation that aerodynamics engineers manually do, and a 4-dimensional optimization to demonstrate the potential of advanced and efficient new designs.

The 1-dimensional analysis brought to a 73.4% of time reduction for assessing the manual tests, leading to significant cost reduction of the research and development phase. Tests at different yaw values were conducted for consistency.

The 4-dimensional analysis was instead carried on by optimization algorithms, to efficiently investigate the search space and find the vehicle configuration that minimizes aerodynamic parameters. Particularly, a series of optimization tests at different yaw values were run, leading to optimized diffuser configurations with unexpected design. The impact on efficiency and range extension was estimated via a rule of thumb, resulting from 0.3 to $3\,km$ extension according to the considered wind direction.

Wind-averaged-drag coefficient was also discussed and computed, to better estimate the actual aerodynamic drag acting on a vehicle. Surprisingly, the minimization of such coefficient was achieved by implementing a 5° yaw side wind.

Moreover, mono-objective and multi-objective optimization investigations were conducted, to demonstrate the difference between very efficient and more balanced solutions and provide drag and lift trade-off configurations.

An estimation of the economic impact was also conducted, covering the reduced downtime by exploiting the new workflow as well as the the efficiency brought by the optimization algorithms in terms of computational times when an increasing number of moving components is introduced.

# Bibliography

[1] J. Wong, *Theory of Ground Vehicles.* 2022.

[2] M. Urquhart, *Vehicles wakes in side wind.* 2021.

[3] S. Windsor, "Real world drag coefficient – is it wind averaged drag?," in *The International Vehicle Aerodynamics Conference*, pp. 3–17, Elsevier, 2014.

[4] J. Howell, "Aerodynamic Drag of Passenger Cars at Yaw," *SAE International Journal of Passenger Cars - Mechanical Systems*, vol. 8, pp. 306–316, 4 2015.

[5] M. L. Whiteman, B. M. Phillips, P. L. Fernández-Cabán, F. J. Masters, J. A. Bridge, and J. R. Davis, "Optimal design of structures using cyber-physical wind tunnel experiments with mechatronic models," *Journal of Wind Engineering and Industrial Aerodynamics*, vol. 172, pp. 441–452, 1 2018.

[6] ev-database, "Volvo EX90 Twin Motor Performance," 12 2022.

[7] J. Pavlovic, A. Marotta, and B. Ciuffo, "CO2 emissions and energy demands of vehicles tested under the NEDC and the new WLTP type approval test procedures," *Applied Energy*, vol. 177, pp. 661–670, 2016.

[8] M. L. Whiteman, P. L. Fernández-Cabán, B. M. Phillips, F. J. Masters, J. R. Davis, and J. A. Bridge, "Cyber-physical aerodynamic shape optimization of a tall building in a wind tunnel using an active fin system," *Journal of Wind Engineering and Industrial Aerodynamics*, vol. 220, p. 104835, 2022.

[9] M. Urquhart and S. Sebben, "Optimisation of Trailing Edge Flaps on the Base Cavity of a Vehicle for Improved Performance at Yaw," *Flow, Turbulence and Combustion*, vol. 109, pp. 309–326, 8 2022.

[10] Schneider Electric, "Modbus Master-Slave Principle," 2020.

[11] SAE International, "J1594. Vehicle Aerodynamics Terminology (J1594 Ground Vehicle Standard)," tech. rep., 1987.

[12] M. Urquhart, E. Ljungskog, and S. Sebben, "Surrogate-based optimisation using adaptively scaled radial basis functions," *Applied Soft Computing Journal*, vol. 88, 3 2020.

[13] United Nations - Inland Transport Committee, "Proposal for Amendment 4 to UN GTR No. 15 (Worldwide harmonized Light vehicles Test Procedures (WLTP))," tech. rep., 2018.

[14] European Commission, "COMMISSION REGULATION (EU) 2017/1151," *Official Journal of the European Union*, 2017.

[15] J. Howell, M. Passmore, and D. Butcher, "An Estimation of the Effect of Turbulence from the Natural Wind and Traffic on the Cycle-Averaged-Drag Coefficient," in *SAE Technical Papers*, no. 2022, SAE International, 3 2022.

[16] J. Howell, M. Passmore, and S. Windsor, “A Drag Coefficient for Test Cycle Application,” *SAE International Journal of Passenger Cars - Mechanical Systems*, vol. 11, pp. 447–461, 4 2018.

[17] C. Kramer, “Introduction into vehicle aerodynamics.,” no. (Short Course 1984-01), 1984.

[18] M. Mamou, Y. Mebarki, M. Khalid, and M. Genest, “Aerodynamic Performance Optimization of a Wind Tunnel Morphing Wing Model subject to various Cruise Flow Conditions,” tech. rep., 2010.

[19] M. Butera, A. Butler, A. Hayes, E. Schaffer, N. Sinha, J. Kapasiawala, and P. Bagchi, “Mechanical-Based Design for Airfoil Structural Morphing,” in *2022 IEEE MIT Undergraduate Research Technology Conference, URTC 2022*, Institute of Electrical and Electronics Engineers Inc., 2022.

[20] Q. IEEE Industrial Electronics Society. Conference (38th : 2012 : Montreal, Institute of Electrical and Electronics Engineers, and IEEE Industrial Electronics Society, *Proceedings, IECON 2012 : 38th Annual Conference of the IEEE Industrial Electronics Society : Ecole de Technologie Superieure de Montreal, Universite du Quebec, Montreal, Canada, 25-28 October, 2012*. IEEE, 2012.

# A

# Appendix 1

| Algorithm | Averaging time | Wind speed | Yaw | Dimension | Sampling budget | Car configuration |
|---|---|---|---|---|---|---|
| Sweep | 20 | 140 | 0 | 1 | 23 | Standard |
| Sweep | 20 | 140 | -5 | 1 | 23 | Standard |
| Sweep | 20 | 140 | -10 | 1 | 23 | Standard |
| Sweep | 20 | 140 | 0 | 1 | 23 | Wheel covers + roof kick |
| Sweep | 20 | 140 | -5 | 1 | 23 | Wheel covers + roof kick |
| Sweep | 20 | 140 | -10 | 1 | 23 | Wheel covers + roof kick |
| Sweep | 60 | 140 | 0 | 1 | 23 | Wheel covers + roof kick |
| Sweep | 60 | 140 | -5 | 1 | 23 | Wheel covers + roof kick |
| Sweep | 60 | 140 | -10 | 1 | 23 | Wheel covers + roof kick |
| Urquhart Surrogate Model | 20 | 140 | 0 | 4 | 60 | Standard |
| Urquhart Surrogate Model | 20 | 140 | -5 | 4 | 60 | Standard |
| Urquhart Surrogate Model | 20 | 140 | -10 | 4 | 60 | Standard |
| Urquhart Surrogate Model | 20 | 140 | 0 | 4 | 100 | Wheel covers + roof kick |
| Urquhart Surrogate Model | 20 | 140 | -5 | 4 | 60 | Wheel covers + roof kick |
| Urquhart Surrogate Model | 20 | 140 | -10 | 4 | 60 | Wheel covers + roof kick |
| Urquhart Surrogate Model | 60 | 140 | 0 | 4 | 60 | Wheel covers + roof kick |
| Urquhart Surrogate Model | 60 | 140 | -5 | 4 | 72 | Wheel covers + roof kick |
| Urquhart Surrogate Model | 60 | 140 | -10 | 4 | 60 | Wheel covers + roof kick |
| Urquhart Surrogate Model | 20 | 140 | 0 | 2 | 60 | Wheel covers + roof kick |
| Urquhart Surrogate Model | 20 | 140 | 0 | 2 | 60 | Standard |

**Table A.1:** List of tests run in the wind tunnel, part 1

| Algorithm | Averaging time | Wind speed | Yaw | Dimension | Sampling budget | Car configuration |
|---|---|---|---|---|---|---|
| Multi-Objective | 60 | 140 | 0 | 4 | 60 | Wheel covers + roof kick |
| Multi-Objective | 60 | 140 | -5 | 4 | 60 | Wheel covers + roof kick |
| Multi-Objective | 60 | 140 | -10 | 4 | 60 | Wheel covers + roof kick |
| Repeatability test | 60 | 140 | 0 | 4 | 4 | Wheel covers + roof kick |
| Repeatability test | 60 | 140 | 0 | 4 | 4 | Wheel covers + roof kick |
| Repeatability test | 60 | 140 | 0 | 4 | 4 | Wheel covers + roof kick |
| Repeatability test | 60 | 140 | 0 | 4 | 4 | Wheel covers + roof kick |
| Repeatability test | 60 | 140 | 0 | 4 | 4 | Wheel covers + roof kick |
| Repeatability test | 60 | 140 | 0 | 4 | 4 | Wheel covers + roof kick |
| Repeatability test | 60 | 140 | 0 | 4 | 4 | Wheel covers + roof kick |
| Repeatability test | 60 | 140 | 0 | 4 | 4 | Wheel covers + roof kick |
| Repeatability test | 60 | 140 | 0 | 4 | 4 | Wheel covers + roof kick |
| Repeatability test | 60 | 140 | 0 | 4 | 4 | Wheel covers + roof kick |
| Bayesian | 20 | 140 | 0 | 4 |  | Standard |
| Nelder Mead | 20 | 140 | 0 | 4 |  | Standard |
| Nelder Mead | 60 | 140 | 0 | 4 | 60 | Wheel covers + roof kick |
| Particle Swarm | 20 | 140 | 0 | 4 |  | Standard |

**Table A.2:** List of tests run in the wind tunnel, part 2

# B

# Appendix 2

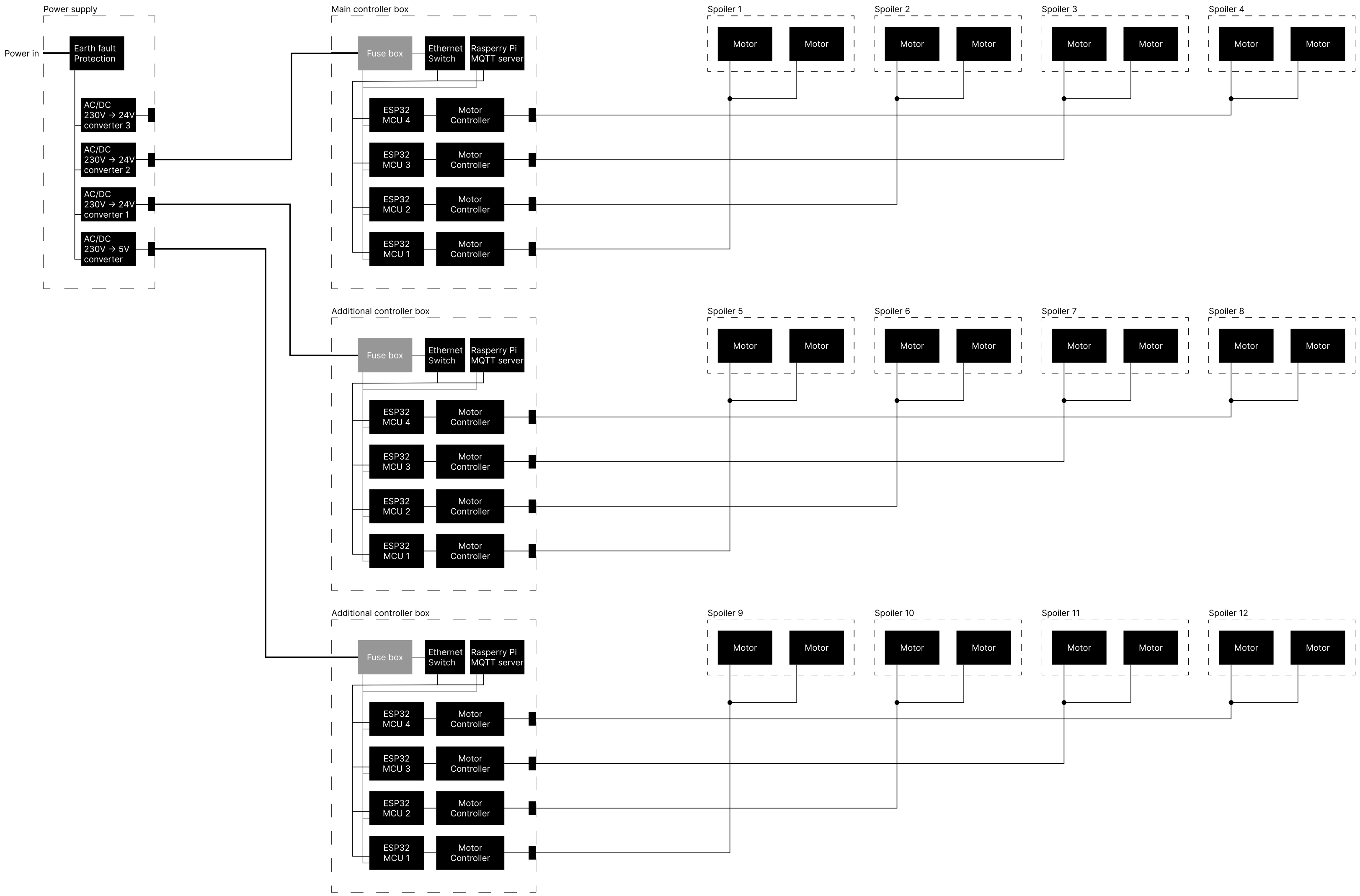

**Figure B.1:** Complete schematic of the test rig.

**DEPARTMENT OF SOME SUBJECT OR TECHNOLOGY**
**CHALMERS UNIVERSITY OF TECHNOLOGY**
Gothenburg, Sweden
www.chalmers.se

CHALMERS
UNIVERSITY OF TECHNOLOGY